UC Merced

UC Merced Electronic Theses and Dissertations

Title

Porous Materials for Two-Phase Heat Transfer

Permalink

https://escholarship.org/uc/item/8591f5v3

Author

Shattique, Md Rubaiet

Publication Date

2023

Copyright Information

This work is made available under the terms of a Creative Commons Attribution License, available at https://creativecommons.org/licenses/by/4.0/

Peer reviewed|Thesis/dissertation

eScholarship.org Powered by the California Digital Library
University of California

UNIVERSITY OF CALIFORNIA, MERCED

Porous Materials for Two-Phase Heat Transfer

by

Muhammad Rubaiet Shattique

A dissertation submitted in partial satisfaction of the
requirements for the degree of
Doctor of Philosophy

in

Materials and Biomaterials Science and Engineering

Committee in charge:

Professor James W. Palko
Professor Min Hwan Lee
Professor Valerie Leppert

2023

Chapter 2 ©2023 Advanced Materials Interfaces, Wiley-VCH.

All other chapters ©2023 Muhammad Rubaiet Shattique

All rights are reserved

The dissertation of Muhammad Rubaiet Shattique is approved, and it is acceptable in quality and form for publication on microfilm and electronically:

Professor James W. Palko, Advisor	Date
Professor Min Hwan Lee, Chair	Date
Professor Valerie Leppert	Date

University of California, Merced

2023

Dedications

To all my teachers for crafting me who I am today,

to the memories of my grandparents, who survived famine and wars,

so that one day I can continue their service,

to my beloved wife, Mou,

to my family and friends who have impacted my life in a thousand ways.

Acknowledgments

I am forever grateful to Professor James W. Palko for his guidance and supervision. Over the course of numerous interactions with him as my research supervisor and my teacher, I have grown as an individual and as a researcher beyond my imagination. I thank him for allowing me to learn and conduct research in his laboratory, for his invaluable instructions, for being patient with my imperfections, for allowing me to nurture my curiosity, and for providing me with the training and support to learn and succeed. His input as a committee member of this dissertation is gratefully acknowledged as well.

Furthermore, and importantly, I am deeply grateful to my other committee members, Professors Min Hwan Lee and Valerie Leppert for their exceptional contributions to my research journey. Their expert knowledge, unwavering guidance, and steadfast support have significantly enriched my investigations and expanded the horizons of my understanding. Their pivotal role on my committee has been instrumental in shaping the trajectory of my work, and I cannot thank them enough for their invaluable mentorship.

I express my gratitude to my fellow group members, Souvik, Neda, Jose, Sebastian, Selina, Roman, Gokce, Maged, and all the undergraduate lab members. The camaraderie, shared laughter, and engaging intellectual discussions with this incredible team have not only fostered my personal growth but also provided vital support for navigating this challenging journey. I am also grateful to my research collaborators Professor Mehdi Asheghi, Professor Kenneth Goodson at Stanford, Dr. Ercan Dede at the Toyota Research Institute of North America, Dr. Sreekant Narumanchi at the National Renewable Energy Laboratory, Dr. Peter de Bock at ARPAe for their guidance and support during this research.

I wish to convey my heartfelt appreciation to Professor Sarah Kurtz for her exceptional support and guidance, which has been instrumental in helping me navigate the challenges of the Materials and Biomaterials Science (MBSE) PhD program at UC Merced. I am also deeply grateful for the close-knit relationship fostered within the MBSE cohort, which I highly value and appreciate. A very special thanks to Dr. Tania Gonzalez.

Growing up along the banks of the Karnaphuli River, where it met the Bay of Bengal just a stone's throw from my home, I would often watch seafaring ships depart from the ports, vanishing into the distant horizons. In my childhood, I sensed that we were all interwoven, sharing this small planet with its myriad joys and challenges. It was during my journey in science and engineering that I uncovered the universal language of the natural world. In this realm, elegant equations and laws transcended borders, enabling me to communicate my thoughts with the world. My heartfelt gratitude extends to my dedicated teachers at Bangladesh Navy School and College, Chittagong, and the Department of MME, BUET for their guidance and love that shaped me. I wish to convey my profound gratitude to the memory of Professor ASW Kurny, my undergraduate supervisor at BUET. He took a lost and curious soul like me under his guidance and skillfully reshaped my path, leaving an indelible mark on my journey. I am indebted to Dr. Maria Stepanova, who introduced me to graduate-level education in the USA and gave me a chance to educate myself in this society, which is deeply invested in the research and development of technologies that impact everyone around the globe. The individuals I encountered on my path in Springfield, MO, Fayetteville, AR, and Merced, CA, have made a profound impact on my personal and intellectual growth. I wish to acknowledge Professor David Cornelison, Professor Saibal Mitra, Professor Nan Zheng, Dr. Ashfaqul Anwar Siraji, and Nancy Parrish for their enduring support. I want to particularly express my sincere gratitude to Dr. Md Delower Hossain and Matthew Robinson for their outstanding guidance in securing research positions during the early stages of graduate school. And, to Shayan C. Arnob for his songs, my companion of countless hours in the lab.

This endeavor would not have been achievable without the unwavering support of my family. I am deeply thankful to my wife, Mahbuba Tabassum Mou for standing by my side and offering her continuous support, and love. I am profoundly grateful to my parents, Nasima and Mahbub, my brother Rhittique, my sister-in-law Rimsha, and my in-laws Tahmina and Mazhar, for their unconditional love. I am grateful to Julfikar Ali Manik for his continuous inspiration. Internally, I feel confident to embark on newer journeys of intellectual endeavors. This to me is not an end, but a new beginning.

I would like to conclude by sharing a few verses that have accompanied and inspired me through the highs and lows of this remarkable journey:

'If you can fill the unforgiving minute
With sixty seconds' worth of distance run,
Yours is the Earth and everything that's in it'
'

- *Rudyard Kipling*

'Our answer is to rely on youth - not a time of life but a state of mind, a temper of the will, a quality of imagination, a predominance of courage over timidity, of the appetite for adventure over the love of ease.'

- *Robert F. Kennedy*

Abstract

Porous materials are ubiquitous in nature as well as in engineering applications. The pores provide exceptional properties of large surface area, efficient transport of mass and energy between the solid matrix, and fluid flowing through the pores and capillarity which facilitates liquid transport without external pumping. Designing and processing porous materials to meet engineering challenges are important for the advancement of society. Currently, porous materials are frequently used as electrode materials for energy storage, construction materials, and importantly, in the thermal management of electronic devices.

Thermal management of electronic materials plays a crucial role in the effective implementation of highly efficient devices. Recent advancements in efficient materials and device designs have paved the way for exceptional computing and electrical power transfer performances. A key bottleneck for the ubiquitous deployment of these devices are large heat fluxes generated by the devices. The inability to dissipate these fluxes limits device performance and often leads to device failure. Novel materials synthesis and engineering of materials for thermal management are key to scientific advancement and society at large.

Among the various techniques available, capillary-driven liquid-vapor phase change, facilitated by porous materials, has exhibited exceptional capabilities in efficiently dissipating large heat fluxes exceeding 1 kW/cm^2. This supersedes the cooling performances of single-phase liquid or air-cooling strategies. To illustrate the challenge at hand for two-phase cooling, modern electronic devices can exceed junction heat fluxes of 5 kW/cm^2. This is anticipated to increase as more sophisticated devices are developed to serve the needs of society, for example, large data centers, high-power lasers, nuclear fusion and fission reactors, electric vehicles, electric vertical takeoff and landing vehicles, and integrated three-dimensional chips, to name a few. There is a pressing demand for breakthrough research and development aimed at achieving highly efficient thermal management via two-phase heat transfer.

In this dissertation, we delve into approaches to leverage thin, free-standing porous materials to achieve liquid delivery through capillary action. We

developed methods to characterize fluid flow properties in the free-standing meshes for two-phase flow conditions. We developed methods to enhance the wettability of mesh structures growing microstructures on the surfaces. The capillary-driven flow in these porous structures is enhanced by careful design of their surfaces to increase their wettability, with the aim of maintaining a thin, evaporating liquid film while retaining high fluid permeability. Our investigation extends to strategies for elevating the system's efficiency by controlling the distribution of liquid and vapor phases. We design and process a three-dimensional manifold that increases the efficiency of uniform fluid delivery and vapor escape during the two-phase heat transfer process. This delivery is targeted at laser-processed porous heat spreaders crafted from Aluminum Nitride (AlN). We identified AlN as an effective substrate material that can be used for liquid-vapor phase change cooling applications directly.

We assess the long-term reliability of AlN under the rigors of prolonged operational conditions for liquid-vapor phase change electronics cooling. We investigate the corrosion of AlN in contact with boiling water. We measure the corrosion rate and its dependency on different heat fluxes during boiling. Furthermore, we delve into corrosion mitigation strategies of AlN in pool boiling conditions. Particularly, we develop surface protections of AlN that effectively mitigate the corrosion behavior of AlN in pool boiling conditions. We find that a thin layer of alumina grown thermally by a one-step process of oxidation of AlN at elevated temperatures is effective in the corrosion protection of AlN.

The findings from this research including the experimental methods and mathematical models developed are expected to propel further research on materials engineering for two-phase electronics cooling of high heat flux dissipating devices and realizations of working commercial devices.

‘*That the powerful play goes on, and you may contribute a verse.’*

-Walt Whitman.

Table of Contents

List of Figures

List of Tables

Chapter 1

Introduction

1.1 Materials challenges in two-phase heat transfer

Materials engineering for efficient thermal management is vital for power electronics, which are expected to handle nearly 100% of all electricity in the next decade, potentially saving a significant amount of energy and reducing global energy consumption by over 25%.[1] Improved power electronics efficiency is crucial for applications like photovoltaic systems, fast-charging batteries, and 3D integrated circuits, where near junction cooling has shown substantial energy efficiency and performance gains. Effective thermal management is also critical for microprocessors, data centers, and supercomputers, as reducing junction temperatures can significantly reduce power consumption and enhance reliability. [2]Commercial power devices typically maintain junction temperatures below 125°C to 175°C for efficiency and long-term reliability. Factors like ON-resistance and charge extraction during switching contribute to conduction and switching losses on power devices. These losses result in heat generation, affecting device temperature, performance, and reliability.[3]

Use of flat heat pipes and vapor chambers, which offer passive heat spreading from a localized heat input area (the evaporator) to a larger heat-rejection area (the condenser). These passive cooling devices working in the evaporation regime can handle heat flux on the range of 100 W/cm^2. From the 1980s, the heat dissipation in electrical and power equipment exceeded the limit of 100 W/cm^2, surpassing most single-phase liquid cooling strategies. To address this issue, designers turned to two-phase cooling systems, which can dissipate more heat while maintaining low device temperatures by utilizing the sensible and latent heat of the liquid. Capillary driven two-phase heat transfer by boiling ensures effective heat spreading for considerably large heat-fluxes than heat-pipes, particularly when sustained boiling takes place in the evaporator, provided the wick structure facilitates adequate liquid resupply through porous pathways.

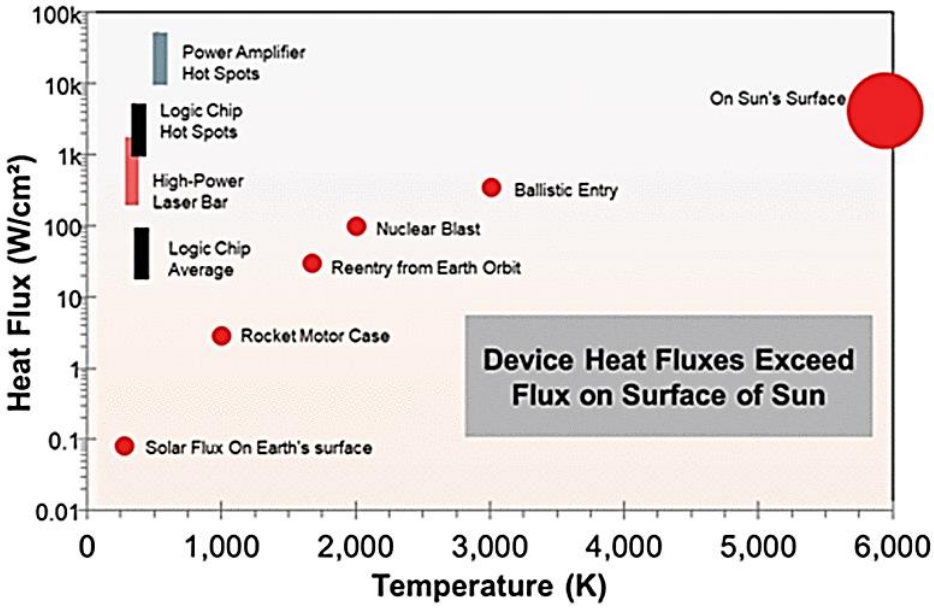

Figure 1.1 Heat fluxes at different temperatures for devices. © [2021] IEEE Reprinted, with permission, from [Avram Bar-Cohen, The ICECool Fundamentals Effort on Evaporative Cooling of Microelectronics, IEEE Transactions on Components, Packaging and Manufacturing.]

Various fluids and cooling techniques were compared regarding heat transfer coefficients, with water achieving values up to a thousand times greater than those of natural convection. Although limited to the Critical Heat Flux (CHF), this improvement has sparked research on nucleate boiling and heat transmission mechanics, particularly for cooling high heat flux dissipating devices. Boiling heat transfer, for example, offers high heat transfer coefficients for this purpose. [5]**Figure 1.2.**

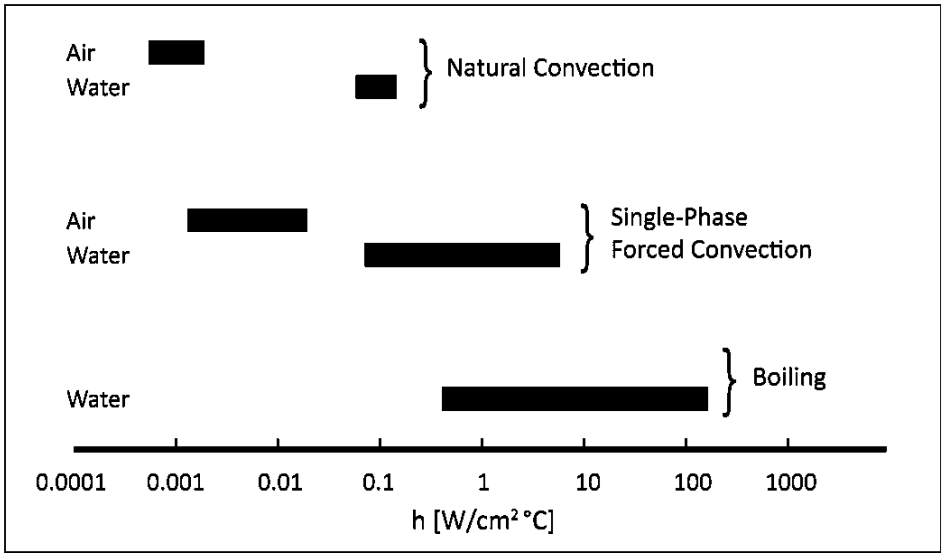

Figure 1.2 Heat transfer coefficient (HTC) of different fluids. Boiling heat transfer provides an exceptionally high heat transfer coefficient.

The process of a substance changing from a liquid to a gas when it comes into contact with a heated surface is a form of boiling. When the surface temperature T_w rises above the liquid's saturation temperature (T_{sat}), vapor production occurs at the solid-liquid interface. The fluid is set into motion by convective waves and bubbling together. From Newton's law of cooling $q'' = Q / A_s = h_b (T_w - T_{sat})$, where, Q is the heat rate, As is the surface area and h_b is the heat transfer coefficient of boiling**. Figure 1. 3.** Provides a typical boiling curve which plots heat flux, q'' on the y-axis and superheat ($T_w - T_{sat,}$) on the x-axis. As heat is applied to the liquid, its temperature gradually increases. When the liquid reaches a certain temperature known as the boiling point at the given pressure, bubbles of vapor start forming at nucleation sites on the container's bottom or other surfaces (A_s). The heat flux rises as the wall superheat increases. When the heat flux reaches a sufficiently high level, an excess of vapor bubbles forms on the boiling surface. These bubbles prevent the liquid from re-establishing contact with the surface, resulting in the formation of an insulating vapor film. This vapor film acts as a thermal barrier, causing a significant increase in wall superheating and ultimately leading to the burnout of the boiling system (B). This transition from nucleate boiling to film boiling is referred to as the boiling crisis, with the maximum heat flux denoted as CHF. Improving CHF can either provide greater safety margins or expand the operational range of heat flux for

boiling systems. (C) and (D) points in the boiling curve represent the Leidenfrost point and film boiling region respectively. For electronics at CHF the device temperature often exceeds the melting point of the material, and material 'burnout' occurs. Operation beyond point (B) is not viable. **Figure 1.3**

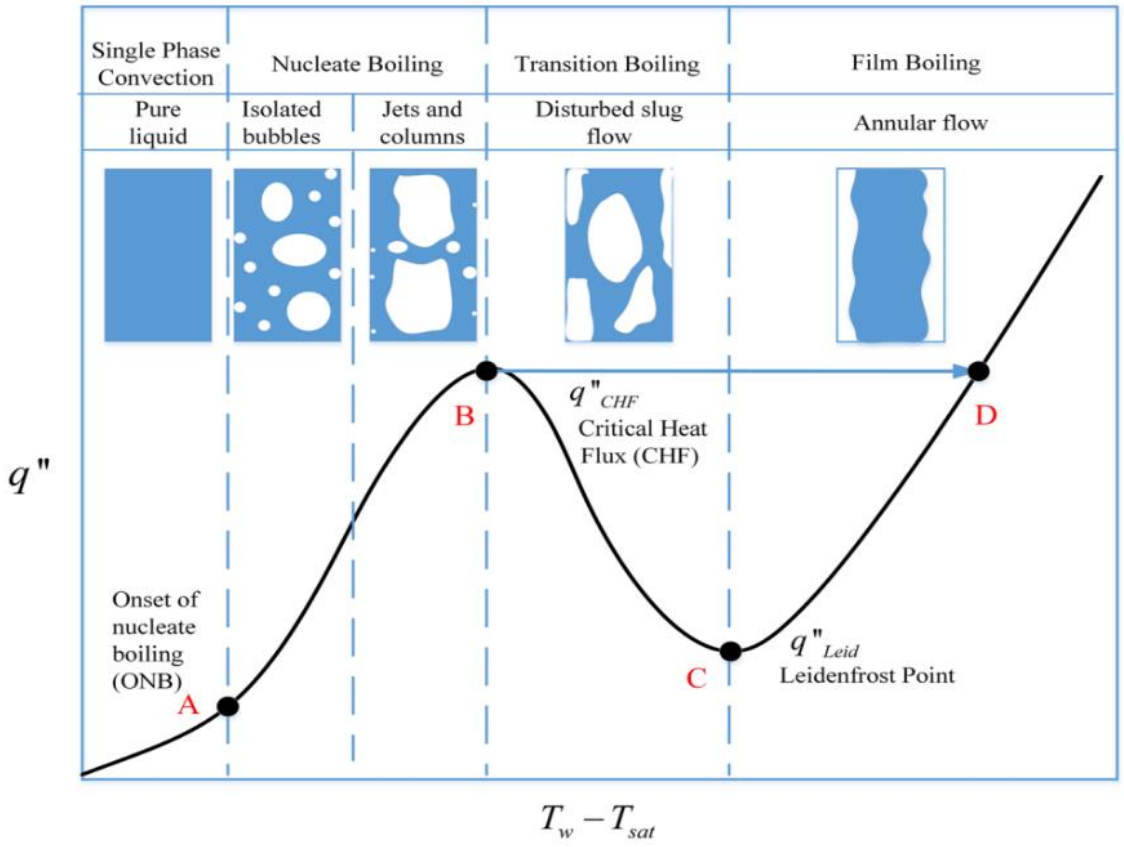

Figure 1.3 A pool boiling curve. Reprinted with permission from [Hu, H *et al*. Boiling and quenching heat transfer advancement by nanoscale surface modification. Sci Rep 7, 6117 (2017)] licensed under CC BY 4.0.

Porous materials are highly effective in conducting heat and facilitating boiling heat transfer due to their high surface area and vapor nucleation sites. Additionally, these materials enable capillary wicking of the heat transfer liquid towards the heated surface, maintaining a thin evaporating liquid film.[6] The Young–Laplace equation, defines the capillary pressure difference at the

interface of two static fluids, like water and air, owing to surface tension connecting this pressure difference with the surface shape.

The capillary pressure, $P_{cap} = \sigma\left(\frac{1}{R_1} + \frac{1}{R_2}\right)$ where R_1 and R_2 are the principal radii of curvature and σ is the surface tension. For spherical shapes such as bubbles or droplets, $R_1 = R_2 = R$ and

$P_{cap} = \frac{2\sigma}{R}$. The radius of curvature R of a sphere can be related to the radius of pore size, r, **Figure 1.4(a),** and the contact angle, θ as $R = \frac{r}{\cos\theta}$.

$$P_{cap} = \frac{2\sigma\cos\theta}{r} \tag{1.1}$$

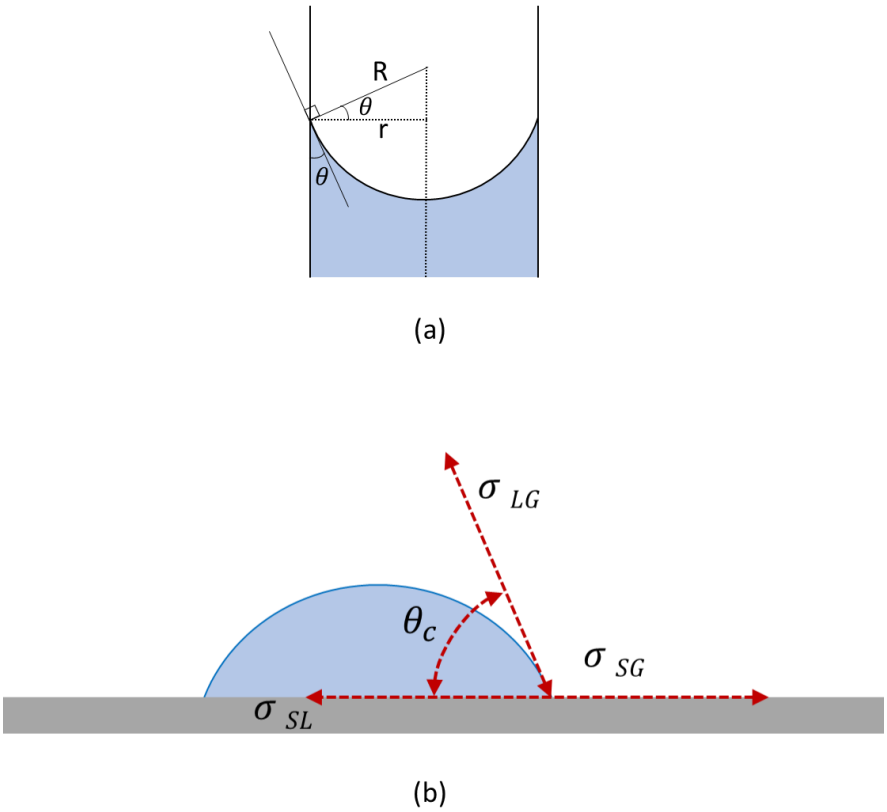

Figure 1.4 (a) Spherical meniscus with a radius of curvature R, inside a pore of radius r. (b) The equilibrium contact angle θ_C is related to the σ_{SG} is the solid vapor interfacial energy, σ_{SL} is the solid-liquid interfacial energy, and σ_{LG} is the liquid-vapor interfacial energy, surface tension of the fluid.

The contact angle (θ_C) is a measure of the wettability of a solid surface by a liquid, represented as the angle between the tangents of the liquid-vapor and solid-liquid interfaces at their point of contact, as described by Young's equation; describing the thermodynamic equilibrium between three phases: the liquid phase (L), the solid phase (S), and the gas or vapor phase (G). Another immiscible liquid phase can be present in lieu of the gas phase. To discuss we illustrate in **Figure 1.4(b)** a sessile drop of liquid is sitting on a solid surface. Surface tension arises from the cohesive forces between molecules, with molecules in the bulk of the fluid experiencing attractive forces from all directions, causing the fluid's surface to curve due to reduced neighboring interactions among exposed surface molecules, leading to a net contracting force on the surface. If σ_{SG} is the solid vapor interfacial energy, σ_{SL} is the solid-liquid interfacial energy, and σ_{LG} is the liquid-vapor interfacial energy (surface tension of the liquid) then the equilibrium contact angle is found from Young's equation:

$$\sigma_{SG} - \sigma_{SL} - \sigma_{LG} \cos\theta_c = 0 \tag{1.2}$$

The Young–Dupré equation relates the contact angle to the work of adhesion, ΔW_{slg} (solid-liquid adhesion energy in a medium G):

$$\sigma_{LG} (1+\cos\theta_c) = \Delta W_{slg} \tag{1.3}$$

When gravity and surface forces are in balance, the capillary length (l_c) acts as a length scaling factor between them, influencing menisci behavior. This equilibrium involves the balance of the fluid pressure related to specific weight and the Young-Laplace pressure that originates from surface tension because there are fewer neighboring interactions at the fluid's surface. In the case of an interface between two immiscible fluids,

$$\textit{Capillary length, } l_c = \sqrt{\frac{\sigma_{lg}}{\Delta\rho g}} \tag{1.4}$$

$\Delta\rho$ is the density difference of the fluids, g is the gravitational acceleration. On Earth, the capillary length for air and water at ambient temperature is about 2.5 mm. The Eötvös number or Bond number (Bo) is a dimensionless number that signifies the relationship between the buoyancy forces and surface tension within a liquid. The Bond number can be expressed by incorporating a characteristic length, typically the liquid's radius of curvature, along with the capillary length.

$$\textit{Bond number, } Bo = \frac{\Delta \rho g L^2}{\sigma} \tag{1.5}$$

Where, L is the characteristic length (e.g., radius of curvature of the meniscus or pore size). In terms of capillary length, $\textit{Bond number, } Bo = \left(\frac{L}{l_c}\right)^2$

A dimensionless metric known as the capillary number (*Ca*) is used to measure the relative importance of surface tension and viscous drag forces at the interface between two immiscible liquids or between a liquid and a gas. It is often mentioned in conjunction with the Bond number.

$$\textit{Capillary number, } Ca = \left(\frac{\mu u}{\sigma}\right) \tag{1.6}$$

Where, μ is dynamic viscosity and u is the characteristic velocity of the fluid. For, fluid flowing through a porous media, u is the superficial velocity of the fluid. Darcy's law describes the superficial velocity u of fluid flowing through a porous media; it is a flux equation where the velocity u (liquid volume flux) is proportional to the pressure gradient (∇p), $u \propto -\nabla p$. The minus sign signifies the fluid flows in the opposite direction of the pressure gradient, i.e., from the high-pressure region to the low-pressure region. The proportionality constant depends on the geometry of the porous media and the viscosity of the fluid. Permeability (k) of the porous media (similar to conductivity for electrical conductors when electrical current flows due to voltage gradient, Ohm's law) captures the geometric contribution to the proportionality constant. When two phases are present in porous material, for example liquid and vapor, the Permeability (κ) is a product of the intrinsic permeability (κ) and the relative permeability (κ_{rl}). The intrinsic permeability is related to the geometry of the porous structure, porosity, ϕ

($\phi = \frac{pore\ volume}{solid\ volume}$) and pore sizes ($r$), generally we can write $\kappa \propto \phi\, r^n$. The relative permeability (κ_{rl}) is related to the saturation of the liquid phase within the porous material and varies from 1 (completely saturated) to zero (completely dried). On the other hand, higher viscosity results to slower fluid velocity. The Darcy's law can be written as,

$$u = -\frac{\kappa \kappa_{rl}}{\mu} \nabla p \tag{1.7}$$

In porous medium, the capillary pressure is often the driving force for fluid flow $\nabla p = P_{cap}$,the fluid flows through a laminar regime (whether the fluid flows in a Laminar or turbulent regime can be calculated from Reynold's number (R_e) which is an dimensionless number, the ratio of inertial forces to viscous forces, $R_e = \frac{\rho u L}{\mu}$ where, L is the characteristic length, e.g., the pore radius.) For a fluid flowing through a porous medium through capillary suction, Reynold's number is low, less than 1, meaning the viscous forces of the fluid dominate the inertial forces. It is worth noting that although permeability increases with pore sizes, the driving force- capillary pressure has an inverse relation with the pore size e.g., (Equation 1.1).

The *Lucas-Washburn* equation relates the distance, *x* travelled by a meniscus in a porous media in time, *t*,

$$L = \left(\frac{\sigma \cos\theta r_e}{2\mu}\right)^{1/2} \sqrt{t} \tag{1.8}$$

Where, r_e is the effective pore radius. r_e can be determined from the Jurin's law which essentially states that the maximum equilibrium height, h_{max} of a meniscus in a capillary tube is inversely proportional to the effective pore radius,

$$h_{max} = \frac{2\sigma \cos\theta}{\rho g r_e} \tag{1.9}$$

Boiling in porous media can be significantly increased by designing porous structures, while the small scales have high capillary pressure, the viscous drag for fluid flow is also higher. On the other hand, large pores have higher permeability and lower capillary pressure. The hierarchical design of porous material with a combination of small and large pores provides separate pathways for liquid delivery to the heated surface, and vapor escape from the heated surface. Moreover, the heterogeneity of the porous surface provides a large surface area for bubble nucleation sites. This can be explained from the classical nucleation theory, according to which a nucleus of a more stable phase can grow from within a stable phase. The rate of nucleation

$$N' \propto \dot{e}^{-\frac{E_{act}}{kT}} \tag{1.10}$$

where, $E_{act}$is the activation energy, the work required to create a stable spherical nucleus.

In the case of homogenous nucleation, the nucleus forms within the bulk of the of the metastable phase. For a nucleus of radius r of phase 1 to form inside phase 2 the energy of the homogenous nucleating phase

$$E_{nuc}^{hom} = {}^{4}/_{3}\,\pi r^{3}\rho_{1}(G_{1}-G_{2}) + 4\,\pi r^{2}\,\sigma_{1,2} \qquad (1.11)$$

ρ_1 is the density of the nucleating phase, G_1, G_2 are Gibbs free energy per unit volume of phase 1 nucleating in phase 2, respectively, $\sigma_{1,2}$ is the interfacial energy between phase 1 and 2. When phase 2 is metastable, the nucleating phase has lower Gibbs free energy, $G_1 < G_2$ the bulk change in Gibbs free energy $\Delta G = G_1 - G_2 < 0$. At maximum of E_{nuc}^{hom} the derivative of equation (1.5) is equal to zero. We can determine the critical radius of the nucleating phase.

$$r_c = \frac{-2\sigma_{1,2}}{\rho_1 \Delta G} \qquad (1.12)$$

the activation energy $E_{act} = E_{nuc}^{hom}$ at $r = r_c$.

However, the requirement to construct an interface and the corresponding surface energy result in an energy cost, it scales with the surface area of the nucleating phase. For heterogenous nucleation, phase1 at the interface of phase 2 and a solid surface. Equation (1.11) can be written as

$$E_{nuc}^{hom} = {}^{4}/_{3}\,\pi r^{3}\rho_{1}(G_{1}-G_{2})f(\theta) + 4\,\pi r^{2}\,\sigma_{1,2}f(\theta) \qquad (1.13)$$

Where, $f(\theta)$ is volume of the spherical cap compared to that of full sphere of the same radius:

$$f(\theta) = \frac{1}{4}(2 - 3cos\theta + \cos^{3}\theta) \qquad (1.14)$$

The critical radius for heterogeneous nucleation, while similar to homogeneous nucleation (Equation 1.12), incorporates changes based on contact angle and solid interfacial energy. This modification results in a substantially lower activation energy for heterogeneous nucleation compared to homogeneous nucleation. This is why nucleation is more often observed at interfaces (such as boiling and condensation surfaces) rather than within bulk fluid. In boiling liquids, bubbles form at much lower superheat temperatures than classical nucleation theories would predict. These bubbles originate from specific nucleating centers on the heated surface. Pits or scratches that contain gas or vapor can serve as potential sites for nucleation. The onset of nucleate boiling,

characterized by the superheat temperature difference (T_w - T_s), depends on surface characteristics and the presence of entrapped gas or vapor in cavities. Initial nucleating centers are randomly distributed. At low heat transfer rates, boiling occurs in patches around these centers, leading to spatial and temporal variations in surface temperature. These boiling patches, where bubbles form and depart, enhance heat transfer by agitating the superheated film and introducing colder fluid to the surface. As heat flux density increases, the superheat temperature also rises, affecting the number of nucleating sites. A comprehensive review of materials nanoengineering for liquid-vapor phase change heat transfer is compiled by (Cho et al., 2016).

Nucleate boiling is a function of temperature as well as surface characteristics. At higher heat fluxes, the influence of surface roughness on the heat transfer rate may diminish, resulting in more uniform boiling without distinct patches. This might involve changes in bubble types and the bubble generation process. As was previously indicated, viscosity causes the liquid to lose pressure over a considerable wicking distance on the porous surface. Additionally, the vapor blanketing stops the liquid from reaching the heated surface at high heat fluxes. The porous heat spreader needs a sufficient and consistent liquid supply in order to overcome restrictions at high heat fluxes. **Figure 1.5.**

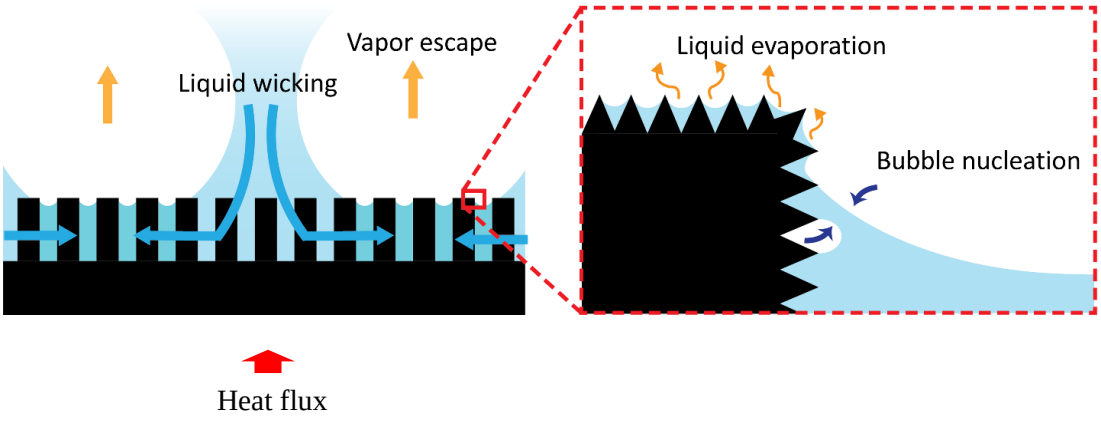

Figure 1.5 Porous surfaces enhance two-phase heat transfer via thin film evaporation and nucleation and growth of bubbles. The figure is inspired by the works from [7].

Various porous materials, including copper inverse opals (CIOs)[8], copper screen meshes [9], [10], copper foam [11]and sintered copper particles [12], have been studied for their effectiveness in capillary-fed two-phase heat transfer. Recent research has focused on two-layer sintered copper particles [13], bi-porous sintered CIO [14], and hybrid copper mesh, demonstrating improved heat dissipation capabilities compared to their monoporous counterparts. The findings reveal that the single-layer wick experiences partial *dry out* with increasing heat flux, ultimately leading to complete dry out, while the two-layer wicks delay partial dry out due to distributed flow. Dry out is a phenomenon when there is insufficient liquid on the heated surface for heat exchange due to evaporation and boiling and insufficient replenishment of liquid due to nonuniform liquid distribution and viscous pressure drop.

One strategy for enhancing the performance of traditional heat pipe wick materials, as previously discussed, involves the implementation of patterned or multi-scale wicks. These wicks exhibit a [15]wide range of pore sizes within the same evaporator. The underlying principle behind this wick structure is twofold: smaller-scale pores extend the capillary limit by generating significant capillary pressure to facilitate liquid flow, while larger-scale pores serve as low-resistance conduits for efficient fluid transport. Moreover, within the evaporator, larger pores contribute to improved boiling performance by creating high-permeability pathways for vapor, while smaller pores continue to supply liquid and act as sites for film evaporation or bubble nucleation. Palko *et al*. demonstrated a laser processed diamond heat spreader conformally coated with electrodeposited CIO with a manifold made of polyimide for fluid management could dissipate a staggering heat flux of ~1300 W/cm^2.[16]

The additional layer at the top of porous evaporator essentially acts as a fluid management device as a manifold. When manifolds are made of microchannels, liquid can be delivered to a heated surface by pumping mechanism. The microchannels ensure uniform fluid distribution on the heated surface, lowering the fluid delivery footprint and ensuring large passages for vapor escape. If porous materials are being used instead of microchannels for the construction, it essentially acts as a '*sponge*' to hold and deliver liquid to the bottom layer evaporator via capillarity. This layer requires sufficient permeability and capillary pressure to deliver liquid required by the porous heat spreader.

For example, we can determine the volumetric flowrate from the porous liquid delivery, $\dot{V}$ required to for heat rate, $\dot{q}$. During liquid-vapor phase change we can equate $\dot{q}=\dot{m}h_{fg,}\dot{m}$ is the mass flow rate of the liquid. Or,

$$\dot{q}= \dot{V}\rho h_{fg} \tag{1.15}$$

ρ is the density of the working fluid. The volume flow rate in a porous media is determined by the superficial velocity of the fluid (u) and the cross-sectional area of flow(A):

$$\dot{V} = uA \tag{1.16}$$

The superficial velocity of liquid in the sponge-like liquid delivery structure can be determined using Darcy's law (Equation 1.4). Rearranging Equation 1.4 we can determine the required permeability of the porous sponge for a maximum heat rate $\dot{q}$.

$$\kappa = -\frac{u\,\mu}{\nabla p} \tag{1.17}$$

Combining the Equations (1.15-1.17) we find that required permeability of capillary fluid delivery of the porous heat spreader has meet the requirement:

$$\kappa = -\frac{\dot{q}\,\mu}{\nabla p \rho h_{fg}} \tag{1.18}$$

The maximum pressure drop due to flow through the porous bulk from the edge to centerline of the active region can be estimated as

$$\Delta p_{liq(\text{maximum})} = -\frac{q''\,\mu}{2\kappa\kappa_{rl}\rho h_{fg}}\,L^2 \tag{1.19}$$

where h_{fg} is the heat of vaporization, ρ is liquid density, L is the effective wicking length, μ is the liquid dynamic viscosity, κ is the intrinsic permeability of the porous copper, and κ_{rl} is the relative permeability for the liquid phase due to partial vapor saturation of the structure. q'' is the heat-flux.

Within these '*hybrid*' micro coolers featuring a secondary capillary driven fluid management device using capillarity in conjunction with the porous heat spreader the saturation of liquid in the sponge like fluid delivery structure varies with the heat rate $\dot{q}$. Therefor permeability of these structures needs to account for the effect of saturation as well. In *Chapter 2* we will discuss this issue in

more detail. We will focus on the characterization of the permeability of a specific free-standing, thin, and porous mesh structure. The objective is to gain a comprehensive understanding of how this mesh structure allows fluids to flow through it under varying capillary pressure conditions. Furthermore, modification of the surface properties of the porous sponge like structures enhance their wettability to improve the fluid transport characteristics. In *Chapter 3*, we delve into an electrochemical method designed to modify the surface properties of the previously characterized mesh. We investigate how altering the surface of the mesh-like structures affects its permeability under different capillary pressure conditions.

During boiling at high heat flux conditions, a major problem occurs when vapor creates a barrier that keeps the liquid from getting to the porous evaporator. The upper sponge layer which distributes liquid, is rendered ineffective by this vapor barrier and CHF occurs. This problem could be resolved if capillary routes for liquid delivery from the upper sponge layer were still available, and the vapor escape path could be improved and controlled. In *Chapter 4*, we assess this issue in detail and design a system containing a three-dimensional (3D) manifold structure for controlling fluids in and out of a porous heat spreader. Along with the design of the manifold we explore novel processing methods containing mesh-like wicks for liquid transport.

The process of thermal management with boiling heat transfer includes the development of bubbles, exposure to high pressures during bubble burst, and an aggressive environment of high temperature liquid. Materials selection plays a key role in designing a cooling device. A schematic illustration of the various materials selection criteria and how they relate to each other for an efficient two-phase cooling system is shown in **Figure 1.6**. The substrate of the device houses electronic circuitry and carries heat away from the device to the ambient for heat exchange (for example via boiling heat transfer). The high surface area (SA), and thermal conductivity (K) of the porous evaporator enhance heat management through conduction, it is also important that they are electrically resistive prevent *shorting* with the electrical circuits laid on the substrate material. For near junction cooling, for example where electrical circuitry is laid on side of the substrate and boiling heat transfer is implemented on the opposite side [17] the porous head spreader facilitates vapor formation and escape, and capillary replenishment of the heat transfer liquid. The effective thermal conductivity of a

homogenous porous material (K_{eff}) is modeled through several methods, notably the Maxwell-Eucken 1 (ME1), Maxwell-Eucken 2 (ME2), the effective medium theory and co-continuous phase (CC) model. [12], [18]K_{eff} from these models and the wick thickness, *d*, can be used to forecast the evaporation-regime surface superheat, as per

$$\Delta T_{sl} = -\frac{q" d}{K_{eff}} \tag{1.20}$$

After the boiling process begins, the system exhibits minimal differential thermal resistance. This low differential thermal resistance can be attributed to three key factors closely linked to the size of the structure: the confinement of vapor bubbles, capillary suction within the liquid phase, and heat conduction through thin liquid films. One factor that is expected to have a significant impact on superheat is the capillary pressure caused by the containment of nucleating vapor bubbles within the porous structure. To illustrate this, consider the spherical pores in the copper layer with a characteristic diameter of 5 μm. These pores can generate a capillary pressure in a vapor bubble of similar size in water at 110 °C, which is approximately 45.4 kPa. This can be described by the *Kelvin* equation relates the increase in vapor pressure to the inverse of the radius of curvature of the meniscus. From *Clausius-Clapeyron* equation this increased vapor pressure leads to an effective superheat, resulting in a temperature elevation of 11 K if the pressure in the surrounding liquid remains at the ambient level of 101 kPa. [16] The liquid pressure within the structure should ideally remain at or below ambient levels. This is primarily because of the viscous losses that occur during the flow through the wick. These losses lead to a reduction in the liquid pressure, which, in turn, should result in a decrease in the absolute pressure within vapor bubbles. Therefore, this reduction in pressure should lead to a decrease in saturation temperature. In other words, the viscous losses partially offset the confinement effect of the porous structure, ultimately reducing the superheat associated with it. Palko et al. estimated a mean vapor pressure inside bubbles[16]:

$$p_{vap(\text{mean})} = p_{amb} - \frac{2}{3}\frac{\sigma}{r_{pore}}\,(3 - 2cos\theta) \tag{1.21}$$

The mechanisms discussed earlier have an impact on vapor pressure at evaporating surfaces and the corresponding saturation temperature. An additional mechanism is thermal resistance caused by heat conduction from the self-heated copper structure to the evaporating surface. This temperature difference due to

conduction also contributes to the overall superheat observed. The resistance to conduction in thin evaporating liquid films is known to be a significant factor in superheating, as seen in studies on heated surfaces and boiling in porous layers. In this context, [8], [16]provided a rough estimate of this effect by considering an effective liquid film thickness that takes into account all transient and spatial variations in the liquid/vapor distribution across the internal surface. This estimated thermal resistance, relative to the active region base area, results from heat conduction through this idealized film with an effective thickness denoted as d_{film}.

$$\Delta T/\Delta q'' = (d_{film}/K_{liq})\,(A_{base}/A_{real}) \tag{1.22}$$

The water's thermal conductivity, K_{liq}, is 0.68 W/m^{-1} K^{-1} at 110 °C. The projected base area and active interior surface area of the structure are denoted by A_{base} and A_{real}, respectively.

Another key component is the liquid for exchanging heat. Enabling liquid transport through capillarity requires a high surface tension. Furthermore, a less viscous fluid can be used to counteract the viscous pressure drop that occurs during capillary transfer. In addition, the high latent heat of vaporization of the liquid guarantees that a substantial quantity of heat can be recovered during the liquid-vapor phase transition. One potential issue with exposing the liquid to high temperatures is that it may catch fire. Materials selection would include a non-toxic, non-flammable liquid. Furthermore, higher thermal conductivity of the fluid reduces the conduction resistance in the thin film region as per equation (1.22). For detailed discourse of the physics the readers are pointed towards '*Liquid-Vapor Phase-Change Phenomena, An Introduction to the Thermophysics of Vaporization and Condensation Processes in Heat Transfer Equipment*', Third Edition by Van P. Carey. [20]

The heat extraction process is improved by effective fluid management, which includes liquid delivery and vapor escape, as was previously mentioned. Furthermore, for a micro-cooler to be implemented successfully, it must have a simple processing mechanism and long-term dependability under boiling conditions. For a prolonged period, the device needs to withstand the harsh boiling environment while preserving the appropriate capillary pressure and permeability that characterize the capillary-driven boiling heat transfer. In *Chapter 5*, we assess the long-term reliability of aluminum nitride (AlN) as a substrate material in the context of two-phase heat transfer systems. AlN is

known for its excellent thermal properties and is often used in electronic cooling applications as a substrate material.[19] This chapter involves experiments and analysis to determine how AlN behaves over an extended period when subjected to the rigors of two-phase heat transfer processes.

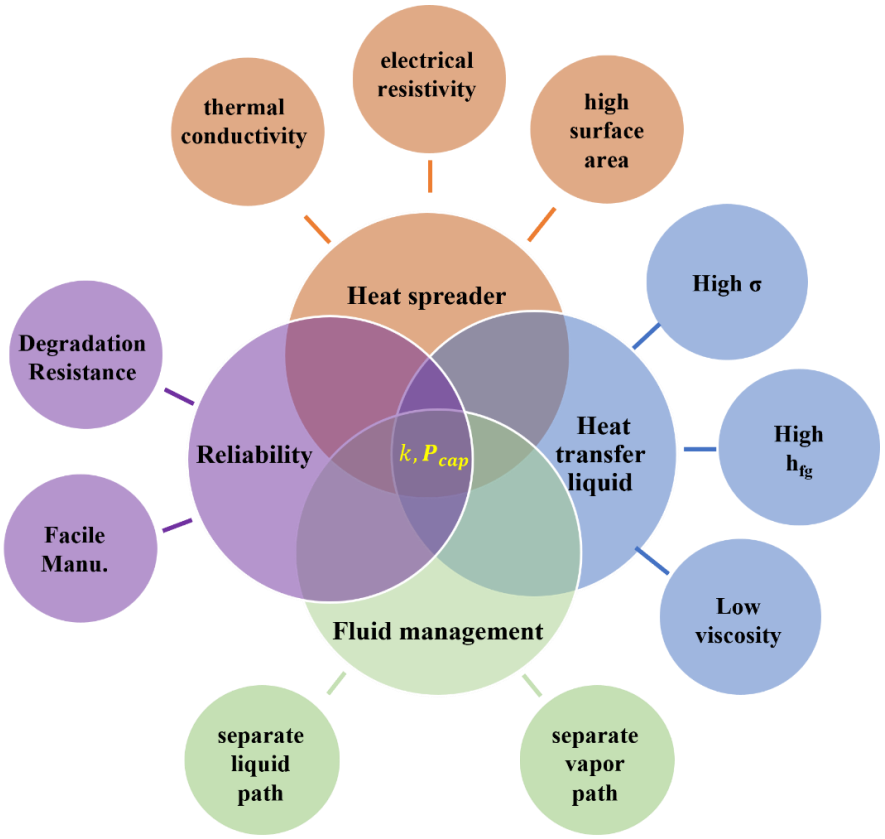

Figure 1.6 Material properties and selection criteria for designing an effective two-phase heat transfer device.

1.2 References

[1] E. M. Dede *et al.*, “Techno-economic feasibility analysis of an extreme heat flux micro-cooler,” *iScience*, vol. 26, no. 1, p. 105812, Jan. 2023, doi: 10.1016/j.isci.2022.105812.

[2] M. H. Mousa, C.-M. Yang, K. Nawaz, and N. Miljkovic, “Review of Heat Transfer Enhancement Techniques in Two-Phase Flows for Highly Efficient and Sustainable Cooling,” *Renewable and Sustainable Energy Reviews*, vol. 155 2022, https://doi.org/10.1016/j.rser.2021.111896.

[3] Y. Qin *et al.*, “Thermal management and packaging of wide and ultra-wide bandgap power devices: a review and perspective,” *Journal of Physics D: Applied Physics*, vol. 56, no. 9. Institute of Physics, Mar. 02, 2023. doi: 10.1088/1361-6463/acb4ff.

[4] A. Bar-Cohen *et al.*, “The ICECool Fundamentals Effort on Evaporative Cooling of Microelectronics,” *IEEE Trans Compon Packaging Manuf Technol*, 2021, doi: 10.1109/TCPMT.2021.3111114.

[5] A. De La Mora, “Modeling boiling physics characterization of the boiling heat transfer coefficient under transient and unsaturated conditions.”

[6] H. Hu, C. Xu, Y. Zhao, K. J. Ziegler, and J. N. Chung, “Boiling and quenching heat transfer advancement by nanoscale surface modification,” *Sci Rep*, vol. 7, no. 1, Dec. 2017, doi: 10.1038/s41598-017-06050-0.

[7] H. J. Cho, D. J. Preston, Y. Zhu, and E. N. Wang, “Nanoengineered materials for liquid-vapour phase-change heat transfer,” *Nature Reviews Materials*, vol. 2, no. 2. Nature Publishing Group, Dec. 06, 2016. doi: 10.1038/natrevmats.2016.92.

[8] C. Zhang, J. W. Palko, M. T. Barako, M. Asheghi, J. G. Santiago, and K. E. Goodson, “Enhanced Capillary-Fed Boiling in Copper Inverse Opals via Template Sintering,” *Adv Funct Mater*, vol. 28, no. 41, pp. 1–8, 2018, doi: 10.1002/adfm.201803689.

[9] B. Subedi, S. H. Kim, S. P. Jang, and M. A. Kedzierski, “Effect of mesh wick geometry on the maximum heat transfer rate of flat-micro heat pipes with multi-heat sources and sinks,” *Int J Heat Mass Transf*, vol. 131, pp. 537–545, Mar. 2019, doi: 10.1016/j.ijheatmasstransfer.2018.11.086.

[10] R. Pastuszko, “Pool boiling on micro-fin array with wire mesh structures,” *International Journal of Thermal Sciences*, vol. 49, no. 12, pp. 2289–2298, Dec. 2010, doi: 10.1016/j.ijthermalsci.2010.07.016.

[11] L. L. Manetti, A. S. O. H. Moita, R. R. de Souza, and E. M. Cardoso, “Effect of copper foam thickness on pool boiling heat transfer of HFE-7100,” *Int J Heat Mass Transf*, vol. 152, May 2020, doi: 10.1016/j.ijheatmasstransfer.2020.119547.

[12] J. A. Weibel, S. V. Garimella, and M. T. North, “Characterization of evaporation and boiling from sintered powder wicks fed by capillary action,” *Int J Heat Mass Transf*, vol. 53, no. 19–20, pp. 4204–4215, Sep. 2010, doi: 10.1016/j.ijheatmasstransfer.2010.05.043.

[13] S. Sudhakar, J. A. Weibel, and S. V. Garimella, “Experimental investigation of boiling regimes in a capillary-fed two-layer evaporator wick,” *Int J Heat Mass Transf*, vol. 135, pp. 1335–1345, Jun. 2019, doi: 10.1016/j.ijheatmasstransfer.2019.03.008.

[14] Q. Wu, C. Zhang, M. Asheghi, and K. Goodson, “Design and fabrication of graded copper inverse opals (g-cios) for capillary-fed boiling in high heat flux cooling applications,” *ASME 2020 International Technical Conference and Exhibition on Packaging and Integration of Electronic and Photonic Microsystems, InterPACK 2020*, no. February, 2020, doi: 10.1115/IPACK2020-2603.

[15] R. Wen, S. Xu, Y. C. Lee, and R. Yang, “Capillary-driven liquid film boiling heat transfer on hybrid mesh wicking structures,” *Nano Energy*, vol. 51, pp. 373–382, Sep. 2018, doi: 10.1016/j.nanoen.2018.06.063.

[16] J. W. Palko *et al.*, “Approaching the limits of two-phase boiling heat transfer: High heat flux and low superheat,” *Appl Phys Lett*, vol. 107, no. 25, Dec. 2015, doi: 10.1063/1.4938202.

[17] Zhang, Chi; Wu, Qianying; Seyedhassantehrani, Neda; Shattique, Muhammad; Roy, Souvik; Palko, James W.; Narumanchi, Sreekant; Kekelia, Bidzina; Sougata, Hazra; E. Goodson, Kenneth; Giglio, Roman; Asheghi, Mehdi; Dede, Ercan M.;, “Heat Flux Micro Coolers Having Multi-Stepped Features And Fluid Wicking,” United States Patent 11729951B2, Aug. 15, 2023

[18] S. Sudhakar, J. A. Weibel, and S. V. Garimella, “Experimental investigation of boiling regimes in a capillary-fed two-layer evaporator wick,” *Int J Heat Mass Transf*, vol. 135, pp. 1335–1345, Jun. 2019, doi: 10.1016/j.ijheatmasstransfer.2019.03.008.

[19] “A HYBRID MICROPOROUS COPPER STRUCTURE FOR HIGH PEROFMRANCE CAPILLARY-DRIVEN LIQUID FILM” 2021.[Online].Available: http://asmedigitalcollection.asme.org/InterPACK/proceedings-pdf/InterPACK2021/85505/V001T05A001/6802665/v001t05a001-ipack2021-73309.pdf

[20] Carey, V.P. (2020). Liquid-Vapor Phase-Change Phenomena: An Introduction to the Thermophysics of Vaporization and Condensation Processes in Heat Transfer Equipment, Third Edition (3rd ed.). CRC Press. https://doi.org/10.1201/9780429082221

Chapter 2

Permeability of Single-Layer-Free-Standing Meshes at Varying Capillary Pressure via a Novel Method

2.1 Introduction

Porous materials, such as mesh wicks, can transport mass, charge, and energy through their pores and matrix and enhance interaction between these two spaces due to their high surface area. Mesh wicks are commonly used in various applications for transferring fluids by capillary action. Their low flow resistance allows transfer of fluids over long distances with minimal pressure drop, making them useful in systems that require a low-pressure gradient, such as heat pipes and fuel cells. [1] In addition, mesh wicks can also be found in oil-water separation systems, desalination systems and gas separation systems.[2–5] As an important example application, in two-phase heat transfer systems, it is often necessary to maintain a thin film of evaporating liquid on the surface of a porous matrix in order to enhance heat transfer.[6,7], [8,9] This enhancement can be achieved using a mesh wick, transporting the liquid through capillary action without needing external pumping. The capillary action of the wick can increase the heat transfer coefficient and the critical heat flux in evaporation and boiling heat transfer processes through optimal delivery of coolant fluid to the heated area.[10–13]

The permeability of a mesh wick refers to its ability to allow fluids to pass through it. It is influenced by the size and shape of the pores in the wick, and when multiple, immiscible phases are present, the surface tension of the liquids and surface energy of the matrix and the relative pressure within each phase.[14–17][18] The permeability of a mesh can be an important factor in many applications, as it can affect the rate at which fluids are transferred through the wick. Darcy's law is used to describe the flow of a fluid through a porous medium based on pressure gradient, ∇p, and dynamic viscosity of the fluid, μ.[19]

$$u = -\frac{k_i k_r}{\mu} \nabla p \tag{2.1}$$

The superficial velocity, u, is equal to the volumetric flow rate (Q) divided by the cross-sectional area (A) of the face of the media normal to the flow. A = width (w) · thickness (δ). In a free-standing mesh, the cross-sectional area for flow is ambiguous, but the superficial velocity can be normalized by the thickness of the single layer of mesh matrix to give $u\delta = Q/w$.

In Equation (2.1), k_i and k_r are intrinsic and relative permeabilities, respectively. Intrinsic permeability is a fundamental parameter related to the geometry of the porous medium and it scales with the square of the characteristic feature size. It has dimensions of area and is often expressed in units of m^2, or non-SI units, such as Darcy (Da). Relative permeability is dimensionless and defined as the ratio of superficial velocity of a given fluid when another immiscible fluid is also present to the value when only the original given fluid is present. The relative permeability depends on the porous structure as well as on the participating fluids and the present and past conditions of the system. The relative permeability of a fluid in a porous medium exhibits a saturation dependency, with a decrease in relative permeability as saturation decreases. In turn, saturation (and therefore permeability) exhibits a dependency on capillary pressure, which may show considerable hysteresis. The Gardner, van Genuchten-Mualem model, Brooks-Corey-Burdine model and theory proposed by Papatzacos-Skjæveland, are commonly employed in analytical and numerical modeling of these properties. [20][21][22] For thin, porous structures without well-defined internal pores, such as free standing meshes, the meaning of relative permeability is less clearly defined and the dependence on flow resistance with capillary pressure less well known.

To measure in-plane intrinsic permeability of meshes, researchers have developed methods considering stacks of meshes submerged in a liquid to understand how different characteristics of the mesh, such as the number of layers, wire diameter and spacing, crimping factor, mesh thickness, and stacking density, can influence single-phase flow through the mesh. [23–26] [27–29][30] The results of these studies have contributed to the development of models, such as the modified Blake-Kozeny equation, which can predict the intrinsic permeability of metal meshes for certain configurations. However, both the measurement methods and mathematical models may not be accurate for very thin stacks of mesh and do not address meshes with free surfaces. The mesh

structure and the surrounding environment also affect how liquid flow resistance varies as capillary pressure changes. Some studies have considered flow in meshes with free surfaces, such as the configuration used in the study by Si-Cong Tan et al. [31] In this study, the permeability of an ultra-thin screen wick with a free surface on one side of the mesh was investigated using a gravity flow method. The copper meshes were welded to a copper plate, leaving a vapor-liquid interface on one side, and the liquid was pumped into the wick using a microflow pump. However, the method is not suitable to measure the permeability of free-standing meshes with liquid-vapor interface on both sides. Additional studies have measured in-plane relative permeability of thin, porous films.[13,32] The environment can play a role in the fluid flow properties of woven meshes, particularly through its effect on evaporation from the wick. [33] Changes in temperature and relative humidity can alter the radius of curvature of the liquid-vapor interface as described by the Kelvin equation. [34] Models have also been developed for through-plane single-phase permeability of meshes accounting for the full three-dimensional structure.[35]

Above a certain capillary pressure in a given porous structure, a percolating liquid phase no longer exists and the relative permeability drops to zero. [36] Smaller pores and higher surface tension result in higher values of this maximum allowable capillary pressure. Optimizing the tradeoff between resistance to capillary pressure and high intrinsic permeability allows enhanced performance in liquid wicking applications.[37] Maximum capillary rise, capillary rate of rise, and bubble point measurements may be used to approximate this maximum allowable capillary pressure. [36,38],[39],[40]

In this study, we demonstrate a new, simple method to measure the permeability of free-standing mesh structures that have liquid-vapor interfaces on both sides. The method involves liquid capillary suction through the mesh by fixing a driving force of gravitational potential using water pools at different heights. It allows measurement of permeability at different capillary pressures. We measure the relationship between permeability-thickness-product ($k\delta$) and capillary pressure in free-standing #100 copper mesh wicks. We provide dimensional analysis to extend the results to other mesh sizes and materials with similar weaves and different working fluids. To our knowledge, the capillary pressure dependence on the liquid permeability of thin single layer porous

structures, such as mesh wicks, that are exposed to vapor phases on both sides has not been previously determined. The relationship between $k\delta$ and capillary pressure of a single layer free-standing mesh can be used to calculate the overall flow performance in various situations by integrating Darcy's law and can be helpful in the design of mesh-based microfluidic devices for two-phase heat transfer applications.[41]

2.2 Materials and methods

2.2.1 Mesh

We analyze metal mesh formed from copper with 99.9% purity (McMaster-Carr). The mesh has a plain weave, **Figure 2.1(a)**, with 100 wires per linear inch, opening size of 0.152 mm, wire diameter, D, of 0.114 mm, and 30.3% open area. The thickness of the mesh, δ, is 0.280 mm. A scanning electron microscope (SEM) image of the mesh, **Figure 2.1(b)**, reveals that the weave creates square openings with all wires of generally uniform size. The mesh shows 4-fold symmetry with wires in both orientations being similarly deformed.

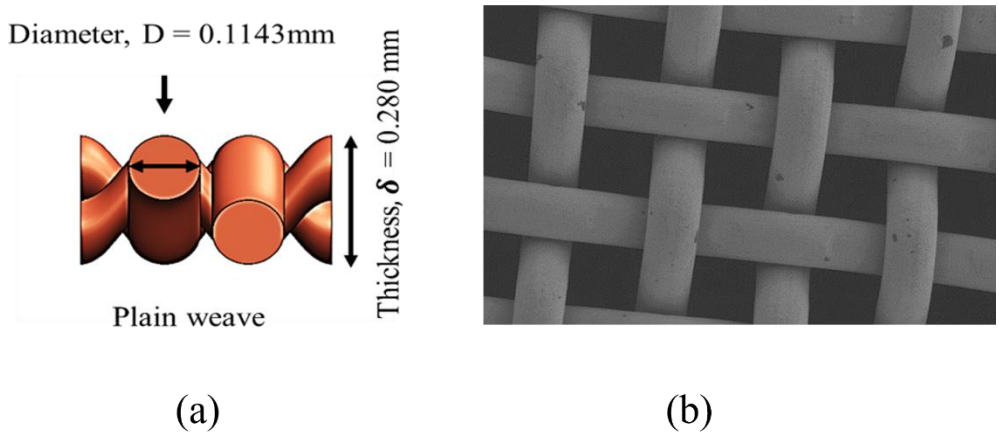

Figure 2.1 (a) Geometry and dimensions of copper wire mesh rendering of mesh with wire diameter, D = 0.114 mm, and thickness, δ= 0.280 mm. The mesh has a plain weave. **(b)** Geometry and dimensions of copper wire mesh, SEM image

2.2.2 Methods

2.2.2.1 Chemical surface preparation of copper mesh

As received, the copper mesh carries surface contamination. Prior to permeability characterization, the mesh is cleaned in caustic solution and then etched in acidic solution to insure reproducible surface properties. The steps for the surface preparation process are listed in **Table 2 -1**. We prepared 1M NaOH from NaOH pellets (MDL Number**:** MFCD00003548) having 97% purity. We prepared 1% H_2SO_4 from concentrated (95-98%) H_2SO_4 (MDL Number: MFCD00064589).

Table 2-1 Surface preparation steps for copper mesh samples

Step number	Process description
1	Cleaning with DI water for 15 min
2	Cleaning in 1M NaOH for 40 min at 80 ^oC
3, 4, 5	Cleaning with DI water for 5 min
6	Etching in 1% H_2SO_4 for 80 min at 80 ^oC
7, 8, 9	Cleaning with DI water for 5 min

This preparation protocol results in consistent data for permeability and capillary rise. We also explored cleaning with surfactants and solvents including hexane and acetone but found this approach to yield inconsistent results.

2.2.2.2 Imaging

We imaged the surface of the copper wire mesh using an SEM (Zeiss Gemini SEM 500), **Figure 2.1(b)**, with 3 kV accelerating voltage and Everhart Thornley secondary electron detector.

2.2.2.3 Permeability Experimental set-up

Figure 2.2 (a) shows a schematic of the permeability measurement set-up. In essence, the mesh forms a siphon between two pools. Two side by side mesh

siphons are considered in each setup (**Figure 2.2 (c)**). The samples have the same length in the vertical sections but different lengths in the horizontal sections. Comparison of the resistance between the two samples allows approximate isolation of resistance due to the excess horizontal section in the longer sample (L^* in **Figure 2.2 (d)**). We measure permeability of section L^* at varying capillary pressure.

The two water pools are maintained at heights h_1 and h_2, respectively, where $h_1 > h_2$. The pool height difference, $h = h_1 - h_2$ is kept constant throughout all experiments at 4.7 cm. We fold each copper mesh to create three sections. A vertical section rises from the top water pool (with length l_u), a horizontal section bridges the two pools (l_x), and a second vertical section drops to the lower pool (l_l). We ensure the mesh is fully saturated in deionized (DI) water prior to each experiment by submerging the mesh in a bath of DI water for 10 minutes. As the mesh is initially saturated, the experiment occurs in a drainage mode. We do not expect any significant difference in behavior if the mesh approaches steady state from an unsaturated condition, but we have not tested this condition, and imbibition into the mesh is very slow. During the experiment, DI water is siphoned from the upper pool through the horizontal section to the lower pool due to the difference in gravitational potential. We can control the capillary pressures in the horizontal sections of the mesh by changing their height with respect to the water pools. An environmental control chamber, with wicking humidifier, maintains an atmosphere that is nearly saturated with water vapor during experiments. We monitor humidity throughout the experiment using electronic humidity sensors (HTM2500LF, Humidity measuring range(*%RH*): 0 – 100, Humidity sensor assembly accuracy (*%RH*): ±3). A secondary cover over the experimental samples prevents the possibility of any condensation from the outer casing falling on the samples themselves.

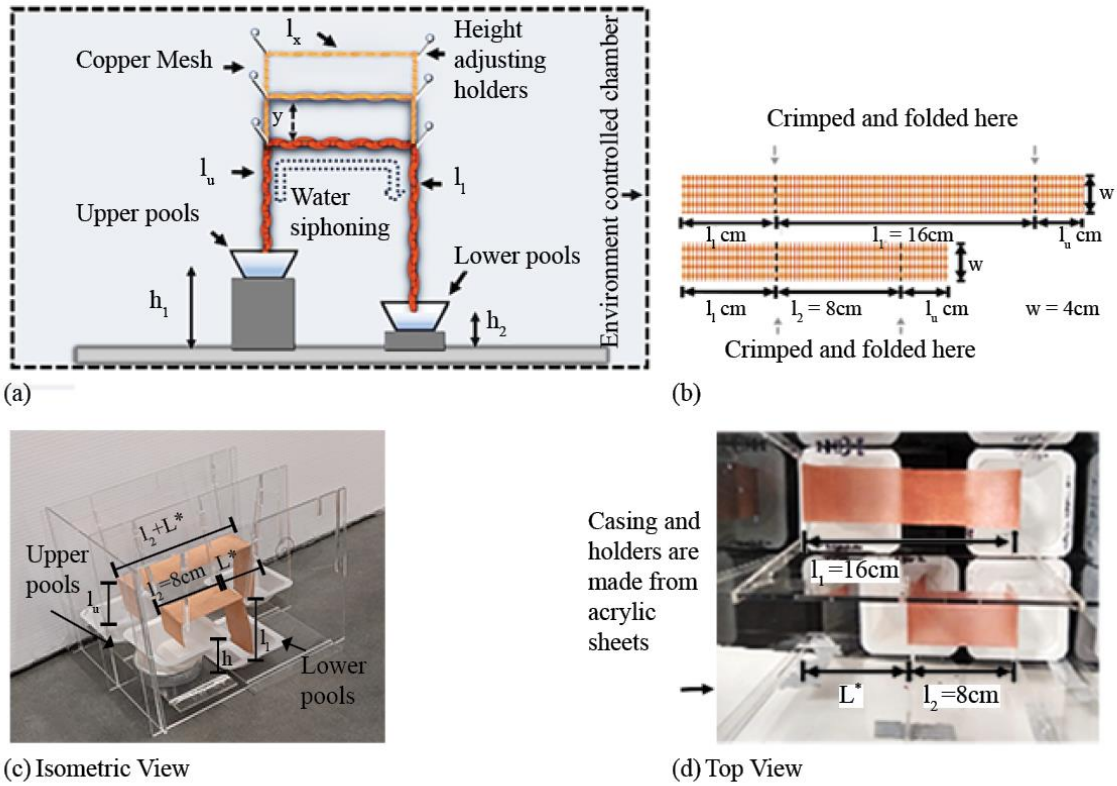

Figure 2.2 (a) Schematic of the experimental set-up for permeability measurements. Water is siphoned from the upper pool to the lower pool via capillary action of the mesh. (b) Schematic of mesh sections with their dimensions. Meshes are crimped and folded at the d dotted lines to create three sections, two vertical (l_u and l_l) and one horizontal ($l_x = l_1$ *or* l_2). (c) Isometric view of the setup: the vertical lengths (l_u *and* l_l) are equal for both the meshes. The pool height difference, h, between the upper and lower pool is constant**.** (d) top view of the setup: two copper meshes with different lengths of the horizontal sections (l_1 and l_2) are placed side by side. Two side by side mesh siphons are considered in each setup. The samples have the same length in the vertical sections but different lengths in the horizontal sections. Comparison of the resistance between the two samples allows approximate isolation of resistance due to the excess horizontal section in the longer sample *(L*).*

Detailed calculations allowing determination of permeability are discussed in the subsequent section. A key element allowing determination of permeability at a defined capillary pressure is the use of two samples in each experiment, as seen in **Figure 2.2 (b)**. The two samples have the same vertical wicking lengths from the upper pool (l_u) and lower pools (l_l), respectively, which can be adjusted, **Figure 2.2 (c)**. However, the length of their horizontal sections (l_x) is different, as pointed out in **Figure 2.2 (d).** l_1 = 8 cm and l_2 = 16 cm. l_1 and l_2 are kept constant throughout all experiments. The width of the copper mesh strips is 4 cm. This width minimizes edge effects and has been used in recent studies of permeability of mesh with a single free surface.[31]

2.2.3 Experimental procedure

2.2.3.1 Permeability of copper mesh

After cutting the meshes, they are cleaned following the protocol described above**.** The meshes are then dipped into a DI water pool to saturate them entirely. At the beginning of each experiment, 20 mL and 10 mL of water is dispensed into each top and bottom polypropylene reservoir, respectively. The saturated meshes are then placed on the holders, as seen in **Figure 2.2 (a)**.

Each experiment is run for 24.0±0.1 hours, after which each pool's mass is measured using an analytical balance. Before starting an experiment, we weighed the mass of the copper mesh dry and saturated the mesh with water. The difference between these masses yields the mass of the water the mesh can hold in a saturated condition ($m_{saturated}$). Water is transferred from the upper pool to the lower pool by siphoning via capillarity of the mesh. The difference in mass at the lower pools from start to finish of an experiment is the mass transferred through wicking ($m_{capillary}$). $m_{saturated}$ is on average ~7% of $m_{capillary}$, which ensures that the primary transport of mass from the upper pool to the lower pool is by capillary wicking, and not draining of the mesh. The mass flow rate is calculated by the mass transferred divided by the time of the experiment and is converted to the volume flow rate by dividing by the density of water. We characterize the water evaporation from the upper and lower water pools by keeping them in the environment control chamber without the mesh installed between the pools for 24 hours (hrs). The evaporation mass loss is < 5% from all

pools. We do a similar tracking of evaporation from saturated copper meshes by placing the meshes on a Teflon sheet inside the environment control chamber at 100% humidity for 24 hrs. The calculated mass loss due to evaporation from the saturated copper mesh is <4%.

2.2.3.2 Maximum capillary pressure measurement

For capillary rise measurements, we cut a 4 cm x 30 cm section from the stock copper mesh described in Section 2.1. The section was cleaned following the procedure described in **Table 2-1**.

The experiment was conducted in an environmental control chamber to ensure that temperature and humidity remained constant during the duration of the experiment**. Figure 2.3(a)** gives a schematic of the set-up. An initially fully saturated mesh sits vertically in a pool of DI water**.** Water drains from the mesh and reaches an equilibrium height. After 24 hours, we record the height of the capillary rise, h_{max}. The maximum capillary pressure $P_{c(max)}$ is given by $\rho\, g\, h_{max}$ where, ρ = density of water at 25 ^{0}C, and g = gravitational acceleration.

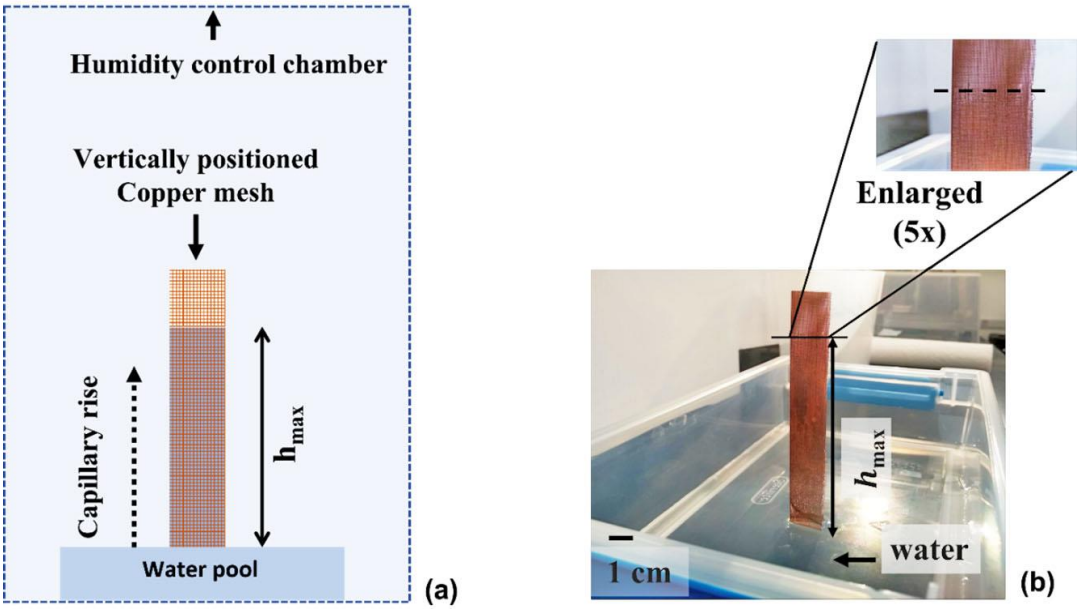

Figure 2.3 (a) Schematic of capillary rise test experimental set-up. Saturated copper mesh stands vertically with one end dipped in a water pool and the other open to ambient. Set-up is enclosed in the chamber maintaining a fixed temperature and ~100% humidity during the experiment. **(b)** Water drains from the saturated mesh and reaches an equilibrium at maximum capillary height, h_{max}

2.2.3.3 Calculation of permeability thickness product

To obtain a correlation between capillary pressure and permeability, we isolate the horizontal region of the sample where capillary pressure is not affected by gravity (though it is still influenced by viscous loss as discussed below). Resistance to flow can be expressed as the driving force for flow divided by the flowrate. Thus, we can write the volumetric flow rate as,

$$Q = \frac{\text{driving force i.e. pressure differences}}{\text{resistance to flow}} \tag{2.2}$$

We keep the pool height difference (driving force) constant during all measurements. By changing the length of the horizontal section of the mesh, l_x, we change the resistance to flow. For example, increasing l_2 to l_2+L^* (**Figure 2.2**) increases the resistance to flow of water through the mesh. This increase in

resistance to flow results in a decreased volumetric flow rate to the lower pool. Thus, we can quantify the resistance to flow by measuring the volumetric flow rate at l_2+L*. We can then use this resistance and Darcy's law to determine the permeability thickness product ($k\delta$). The liquid pressure drops along the length of the wick due to viscous loss. Capillary pressure, P_c, is defined as the difference between the gas pressure in the environment, P_g, and the local liquid pressure in the wick, P_l ($P_c = P_g - P_l$). Capillary pressure varies throughout the wick due to elevation change and viscous pressure loss. We use two meshes side by side, having equal vertical wicking lengths but different horizontal flow lengths, to correct for the variable capillary pressure and permeability found in the vertical sections. We can change the vertical sections of the mesh (e.g., $l_u + y$, from upper pool; $l_l + y$, from lower pool) to drive flow at varying capillary pressure. We define resistance to flow for three mesh sections, (l_u, l_x, l_l) to develop our calculation for determining permeability thickness product ($k\delta$) with different capillary pressure.

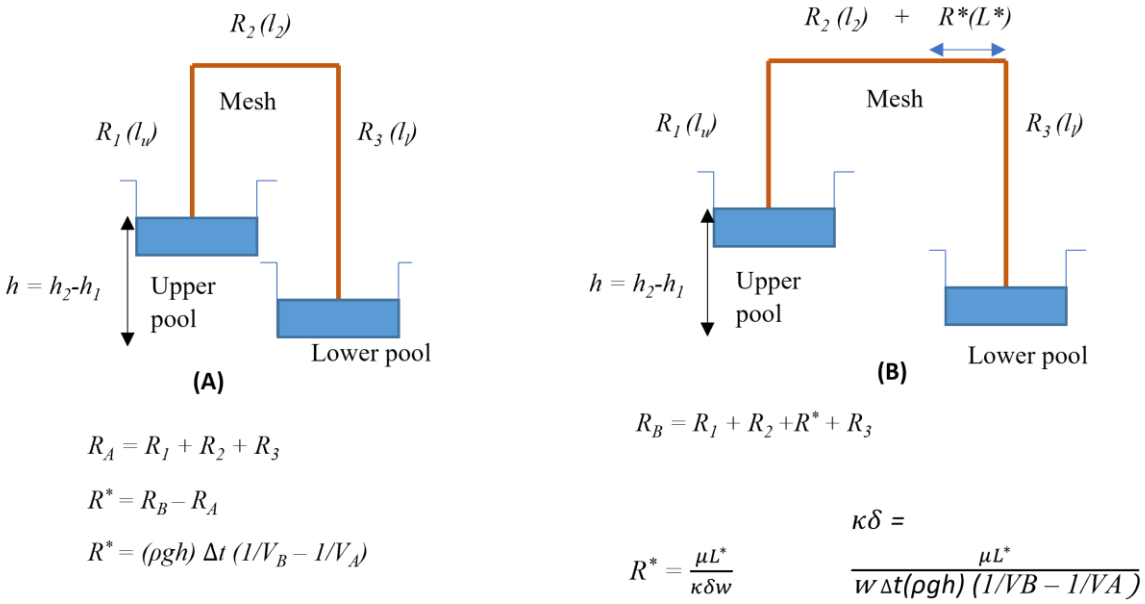

Figure 2.4 . Calculation details to determine permeability thickness product ($k\delta$) at varying capillary pressures (P_c). δ is thickness, and w is width of the copper mesh. In **Figure 2.4 (a)**, R_1 is resistance to flow of water in the part of length of l_u, R_2 is resistance to flow of water in the part of length of l_2 ,and R_3 is resistance to flow of water in the part of length of l_l . In **Figure 2.4 (b)**, R* is resistance to the flow of water in the length of L*. h is the pool height difference between the upper and lower water pools. R_A is the total resistance to flow in setup (A) and R_B is the total resistance to flow in setup (B), $R^* = R_B - R_A$.

In **Figure 2.4** above we schematically show our experimental set-up with corresponding resistances defined. Flow resistance for the shorter sample (A) is divided into: R_1, related to the length of l_u; R_2, related to the length of l_2, and R_3, related to the length of l_l. Since all these resistances to flow are in series, we can write the total resistance to flow of (A) as $R_A = R_1 + R_2 + R_3$. Resistances for the longer sample (B) are similar to (A), except for the horizontal resistance which is $R_2 + R^*$, related to the length of $l_2 + L^*$. Thus, the total resistance to flow of (B) is $R_B = R_1 + R_2 + R^* + R_3$.

If we subtract R_A from R_B, we find the resistance R^* related to the length L^* i.e., $R^* = R_B - R_A$. Now, resistance to flow in B, $R_B = \frac{\text{driving force i.e.capillary pressure}}{Q}$. If V_B is the volume of water transferred in time Δt then, $Q = (V_B/\Delta t)$, and the driving pressure is ρgh, where ρ is the density of water at 25 °C, g is gravitational acceleration, and h is pool height difference. Thus, $R_B = (\rho gh\Delta t/V_B)$. Similarly, $R_A = (\rho gh\Delta t/V_A)$. Therefore,

$$R^* = (\rho gh\Delta t/V_B) - (\rho gh\Delta t/V_A) \tag{2.3}$$

Again, if we consider the flow of water in the horizontal section of the mesh, it follows Darcy's law. For a mesh cross-sectional area of A, where A = width(w) · thickness (δ), the volume flow rate, $Q = u\,A$. The resistance to flow R^* of the length L^*

= pressure drop along the length L^*/ volume flow rate .

Or, $R^* = \Delta p/Q = \Delta p/uA = u\ \mu\ L^*/u\ k\delta w$. Where, μ is the dynamic viscosity of the fluid.

Therefore, resistance to flow in the horizontal section with length L^* is,

$$R^* = \mu\ L^* / k\delta w \tag{2.4}$$

From (3) and (4), the thickness permeability is product given by:

$$\kappa\delta = \frac{\mu L^*}{w\Delta t(\rho gh)\ (1/V_B - 1/V_A)} \tag{2.5}$$

As the mesh is free standing, we consider this product to be the most appropriate measure of fluid conductivity for the structure.

Capillary pressure corresponding to the flow resistance measured (i.e. in the excess horizontal length, L^*) is not uniform due to the viscous pressure loss in this section. This increment in viscous loss and corresponding capillary pressure also makes the equivalence in resistance of the two samples' common sections (**Figure 2.4**) only approximate. The additional resistance induces some change in the capillary pressure and corresponding resistance of the remainder of the sample, but as shown in supporting materials section SM.(I), this contribution is relatively small. Viscous loss in the vertical and common horizontal sections also contributes uncertainty in the capillary pressure experienced by the section of interest (L^*). Here we approximate the capillary pressure at the region of interest as the average of the gravitational head above the upper and lower pools, i.e. $P_c = \rho g \left(\frac{l_u + l_l}{2}\right)$. Approaches to eliminating this uncertainty in capillary pressure are discussed in the following section.

2.2.3.4 Scope and limitations of method

The method described here can be extended to measure permeability-capillary pressure relationships for a wide range of thin, porous structures. Forming the material of interest into the three sections of the measurement apparatus, as shown above, is convenient but not necessary and may not be possible for brittle materials. A separate standardized wicking material can be used for all but the unique section (L^* in **Figure 2.2**). The wicking material must support a maximum capillary pressure higher than that of the material under test and preferably have low net flow resistance (which can be reduced by increasing thickness). A schematic of this modified approach is given in the supporting information section SM.(IV).

The primary limitation in the method presented is the determination of capillary pressure at the section of interest. As discussed above, viscous pressure drop introduces uncertainty in the capillary pressure. Capillary pressure uncertainty is bounded by the driving force applied for flow. A small height difference between upper and lower pools yields well defined capillary pressure but also incurs low flow rates and attendant issues including increased importance of evaporation, liquid volume held in the mesh, and mass measurement uncertainty. Alternatively, the capillary pressure at the region of interest can be refined by an iterative approach applying the permeability-

capillary pressure relation determined using the nominal capillary pressure to correct for viscous pressure drop, then rescaling the relation by the corrected capillary pressure and iterating until a self-consistent solution is obtained. Viscous pressure loss across the region of interest (L^*) also reduces the accuracy of equating the resistances of the remaining sections of both samples. This inaccuracy can be reduced by minimizing the length of the region of interest at the expense of reducing the difference in response between the samples and increasing error associated with the subtraction of the accumulated flows.

2.3 Statistical analyses

We measured permeability of three independent samples at each capillary pressure. Data for all samples is presented. There is negligible uncertainty in the measured mass of liquid transferred and time for flow, which contribute to each permeability measurement. Maximum capillary pressure is determined from measurements of three independent samples. The average maximum capillary pressure and uncertainty, equal to the maximum difference between measured values and the average, are reported. There is negligible uncertainty in the height of the horizontal sections with respect to both pools from which the nominal capillary pressure is calculated. Ambiguities in capillary pressure associated with viscous pressure drop are discussed in the previous section.

2.4 Results and discussion

2.4.1 Surface cleaning of copper wire mesh

Based on SEM analysis, prior to surface cleaning, the mesh shows non-metallic debris on the wire surfaces, **Figure 2.5 (a)**. This debris, which likely originates from the lubricant used during the drawing process of the copper wire as well as handling and storage of the mesh, agglomerates as islands on the surface of the mesh. It is detectable by electron beam charging. Following cleaning process steps 1-5 described above, the islands of debris are removed from the surface, **Figure 2.5 (b)**. The surface of the copper mesh is again imaged after cleaning steps 6-9 (including etching in sulfuric acid). The etching results in roughening of the copper wire surface.

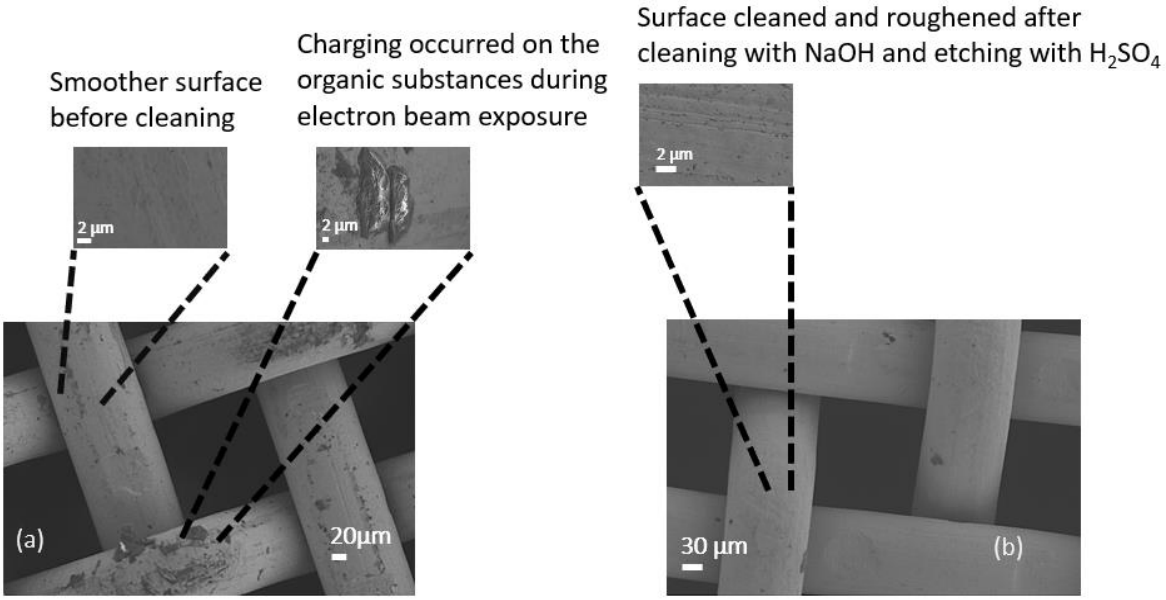

Figure 2.5 SEM of copper wire mesh surface: (a) as received copper mesh contains organic compounds. Charging occurred on the organic substance on copper mesh during electron beam exposure. (b) After cleaning with 1M NaOH, the organic debris were removed from the surface and followed by etching with 1% H_2SO_4 further cleaned and roughened the copper mesh surface.

2.4.2 Maximum capillary pressure P_c *(max)*

Based on the method described above, the maximum capillary rise is measured as h_{max} = 10.5±0.2 cm. The maximum capillary pressure supported by the mesh is determined as $P_c(max) = h_{max}\ \rho\ g$ = 1027±19.5 Pa, where ρ is the density of water at 23 °C, and g is the gravitational acceleration.

2.4.3 Change of permeability thickness product of wire mesh (#100) with capillary pressure

Using the procedure described above (2.3.1 and 2.3.3), we measure the permeability thickness product ($k\delta$) for the mesh over a range of capillary pressures from ~600 Pa to ~1000 Pa.

Figure 2.6 shows the permeability thickness product data for cleaned copper #100 mesh at different capillary pressures. We performed three independent $k\delta$ measurements for each capillary pressure with separate mesh samples for each measurement. The permeability thickness product is relatively insensitive to pressure at low capillary pressure. As we increase the capillary pressure, the $k\delta$ product value starts to decrease gradually at capillary pressures around 750 Pa. With an increase in capillary pressure the radius of curvature of the meniscus between the liquid and vapor phases decreases. For a free-standing mesh with two liquid-vapor interfaces at the top and bottom of the mesh, this results in a decreased cross section of liquid volume available for flow. $k\delta$ then decreases more rapidly with increasing capillary pressure, before the decrease moderated around 950 Pa. At even higher capillary pressures, beyond 1000 Pa, the $k\delta$ value is very low and again shows relative insensitivity to capillary pressure. We fit (orange curve of **Figure 2.6**) the permeability thickness product versus capillary pressure data with a sigmoidal curve as chosen below, where P_c is capillary pressure.

$$\kappa\delta = \frac{a}{1+\exp\left(b(P_c-c)\right)} + d \qquad (2.6)$$

A least squares regression yields the following parameters: a = 7.07x10^{-15} m^3, b = 0.0208 Pa^{-1}, c = 700 Pa, d = 1.11x10^{-15} m^3. We note that this fit does not have a physical basis, and other functions could be applied. The experimental uncertainty of the experimental data may originate from different surface conditions of the copper mesh originating from the mesh processing step, different rates of evaporation of water during experiments, and deviation from linearity in the vertical and horizontal sections of the mesh originating from the mesh folding step. The masses of the water pools were measured using an

analytical balance and likely do not contribute appreciably to experimental uncertainty.

We have considered simple porous flow resistance models for comparison to the measured mesh behavior at low capillary pressure. The Carman-Kozeny relationship predicts a value of $k\delta = 45.3\text{x}\ 10^{-15}\ \text{m}^3$. ($k\delta = (D_p^2/180) \cdot (\Phi^3/(1-\Phi)^2) \cdot \delta$, where, D_P is the effective pore size of the nesh, and Φ is the porosity of the copper mesh [15]. For our copper mesh the calculated porosity Φ is 65% (see supplementary material SM.(III)). As expected, such a calculation which attributes the full thickness of the mesh as available to flow, overestimates the observed flow (e.g., by ~400%).

We note that the hydrodynamic pressure drops along the horizontal length of the wick for the flow rates measured through our experiment are small compared to the mean capillary pressure. The ratio of the pressure drops (ΔP) to the capillary pressure (P_c) ranged between 12.5% to 7.5% (supporting materials **Figure 2.10 SM1**).

2.4.4 Dimensional analysis

The results obtained for flow resistance versus capillary pressure for the free-standing mesh can be generalized beyond the specific size and material of mesh studied. Dimensional analysis allows us to consider the relationship between non-dimensionalized expressions of flow resistance and capillary pressure, which can be applied to similarly shaped meshes of different scales.

For small meshes of similar geometry but different scale (i.e., plain weave meshes with the same ratio of wire diameter to opening size), we can expect the value of $k\delta$ to depend only on a limited number of parameters. These are L_m, length scale of the mesh (e.g., diameter of the mesh wire or mesh spacing), σ, surface tension of the liquid, P_c, capillary pressure, and liquid contact angle for the surface, θ. Only these parameters are significant as long as surface tension dominates. For the mesh considered here, the Bond (or Eötvös) number ($\frac{\Delta\rho g L^2}{\sigma}$)

is very small. Using the wire diameter as the characteristic length, the calculated Bond number is 1.75 x 10^{-3}<< 1, indicating that the surface tension forces overwhelm gravitational ones. Furthermore, the fluid is in the Stokes flow regime (Reynold's number, $Re <$ 5 x 10^{-4} at room temperature for water) so that we can define a flow resistance that is independent of the effect of fluid velocity and driving pressure for flow. We further note that many liquid/solid combinations will have a contact angle near zero. For example, clean solid metal surfaces are hydrophilic and tend to have very low contact angle with water (close to 0-degree). Based on Hamaker coefficients for metal surfaces using Lifshitz theory, it is suggested that physical interactions at the metal-water interface are composed solely of dispersion forces. If the macroscopic Hamaker coefficients are calculated from the Lifshitz theory, dispersion forces alone are sufficient to predict metal surfaces as strongly hydrophilic [23,42–45]. Furthermore, low surface tension liquids such as hydrocarbons or halogenated hydrocarbons show essentially zero contact angle on many surfaces.

From dimensional analysis we find that,

$$k\delta/L_m^3 = f'(P_c L_m/\sigma, \theta) \quad (2.7)$$

Where, L_m, length scale of the mesh (e.g., diameter of the mesh wire or mesh spacing), σ, surface tension of the liquid, P_c, capillary pressure, and liquid contact angle for the surface, θ.

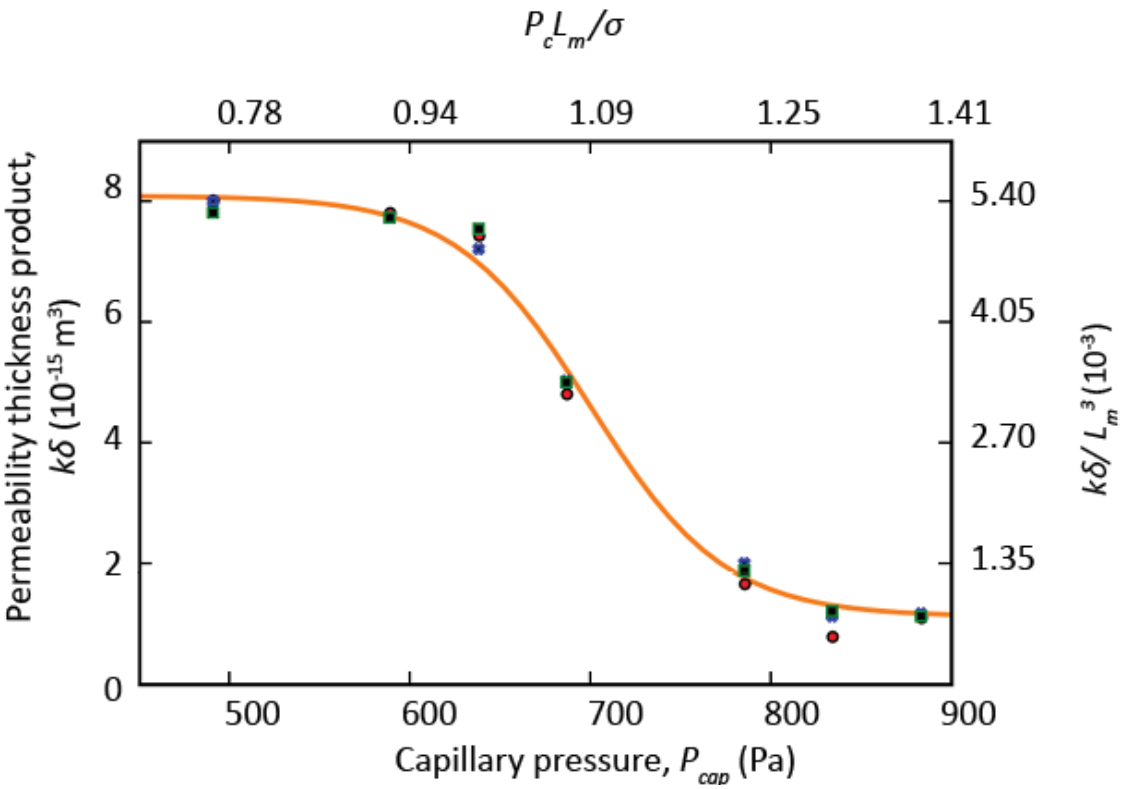

Figure 2.6 Permeability thickness product (kδ) of plain weaved copper wire mesh #100 at different capillary pressures for water at room temperature. Data points are measured experimentally. Line is fit using Equation (6). Axes are also given for dimensionless flow resistance $k\delta/L_m^3$ (right) and dimensionless capillary pressure, P_cL_m/σ (top). We used known surface tension of DI water at room temperature and wire diameter of the mesh to nondimensionalize the axes. Data for all (3) independent samples at each capillary pressure are shown.

Equation (2.7) is a generalized non dimensional one, that can be used along with the plot in **Figure 2.6** to describe flow resistance of meshes with any mesh number that have a similar weave (i.e., geometric similarity) as that described in section 2.1, and liquid/solid combination with similar contact angle. **Figure 2.6** also shows axes for nondimensionalized capillary pressure, P_cL_m/σ, (top) and flow resistance, $k\delta/L_m^3$, (right). Details of the dimensional analysis are given in the supplementary section SM.(II).

2.4.5 Effect of surface cleaning

We measured the permeability of as-received copper mesh containing surface debris, without surface cleaning. We find the permeability of the as received mesh is lower than the cleaned copper mesh at a similar capillary pressure (e.g., at ~490 Pa the permeability thickness product of as received mesh prior to cleaning is ~2.2 x 10^{-15} m^3 compared to ~ 8.1 x 10^{-15} m^3). We believe this effect results from poor wetting of the mesh by water due to non-polar nature of the potential contamination, such as oil. We also measured the wetting property of the as-received mesh prior to cleaning by a capillary rise test with DI water as our working fluid in a humid environment. After 24 hours we find that the maximum capillary height on the uncleaned mesh is, $h_{max}^{uncleaned}$ = 3.8 cm, on average, and the resulting maximum capillary pressure of the uncleaned mesh $P_c\,(max_{uncleaned}) = h_{max}^{uncleaned}\,\rho\, g$ = 371 Pa.

2.4.6 Flow performance of free-standing meshes

The permeability/capillary pressure relation given in **Figure 2.6** provides information necessary to predict flow through free standing meshes having various lengths and applied driving pressure. This can be expressed in general form as an integration of Darcy's law for pressure drop along one dimension (the flowline). The volumetric flow rate of a free-standing mesh, normalized by the viscosity of the liquid and the length of the mesh, can be described using a modified version of Darcy's law as follows:

$$u\delta\mu l = \int_o^P \kappa\delta\left(p_g - p\right)dp \tag{2.8}$$

Where, p_g is the vapor pressure and p is the liquid pressure. For a constant gas pressure surrounding the free-standing, horizontal mesh, the capillary pressure increases proportionally to the hydrodynamic pressure loss. We determine the $\kappa\delta(p)$ relationship from our experiments, as fit in Equation (2.6). Applying this relationship, assigning zero capillary pressure at zero position, and integrating with respect to pressure in the liquid gives us the superficial velocity of water in a 1D free-standing wick normalized with regards to viscosity and length of the wick.

The integration of Equation (2.8) yields,

$$u\delta\mu l = (a+d)\Delta P - \frac{a}{b} ln\left(e^{b(\Delta P - c)} + 1\right) + p_0 \qquad (2.9)$$

Where, $p_0 = 5.07$ x 10^{-12} Pa.m^3 (Values of other constants are given above with Equation (2.6).) Plotting Equation (2.9) for different pressure differences (ΔP), we find that the normalized superficial velocity ($u\delta\mu l$) increases with increasing pressure difference almost linearly at lower pressures. After a specific pressure drop, the rate of change of $u\delta\mu l$ decreases significantly, corresponding to the increase in flow resistance with increasing capillary pressure. Following the dimensional analysis approach above, we can likewise relate a dimensionless velocity length product and pressure. **Figure 2.7**

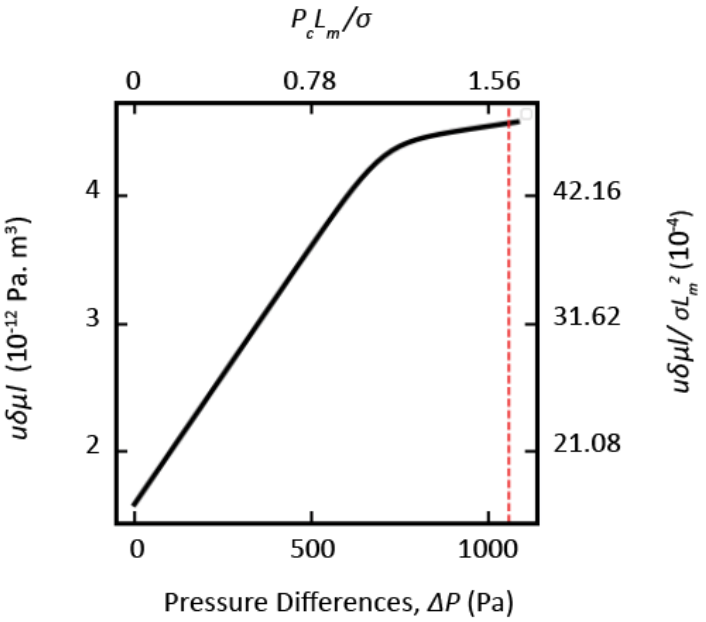

Figure 2.7 Normalized superficial velocity $u\delta\mu l$ (Pa.m^3) versus pressure differences ΔP (Pa). We used wire diameter and surface tension of DI water at room temperature to nondimensionalize the axes. The red-dotted straight line indicates the maximum capillary pressure, $P_c(max)$.

Equation (2.9) can be applied to understand the performance of mesh in specific cases. We can consider the maximum flowrate that can be achieved for DI water in copper #100 mesh with plain weave and wire diameter 0.114 mm assuming a driving pressure equal to the maximum capillary pressure. **Figure 2.8 (a)** shows the values of superficial velocity through a single layer free standing mesh wick, $u\delta$, at maximum driving pressure for different dynamic viscosities, 0.282 mPa s, 0.354 mPa s, 0.466 mPa s, 0.6527 mPa s, and 0.95 mPa s, respectively. For a fixed capillary pressure, $u\delta$ decreases with increasing wicking length asymptotically approaching zero at rates determined by the liquid viscosity. Likewise, **Figure 2.8 (b)** shows $u\delta$ in the mesh at wicking lengths of l = 0.25 cm, l = 0.50 cm, l = 0.75 cm, and l = 1 cm versus total pressure drop for DI water, (dynamic viscosity at boiling point of water, μ = 0.282 mPa s), demonstrating higher $u\delta$ through shorter wicking distance with increasing pressure differences.

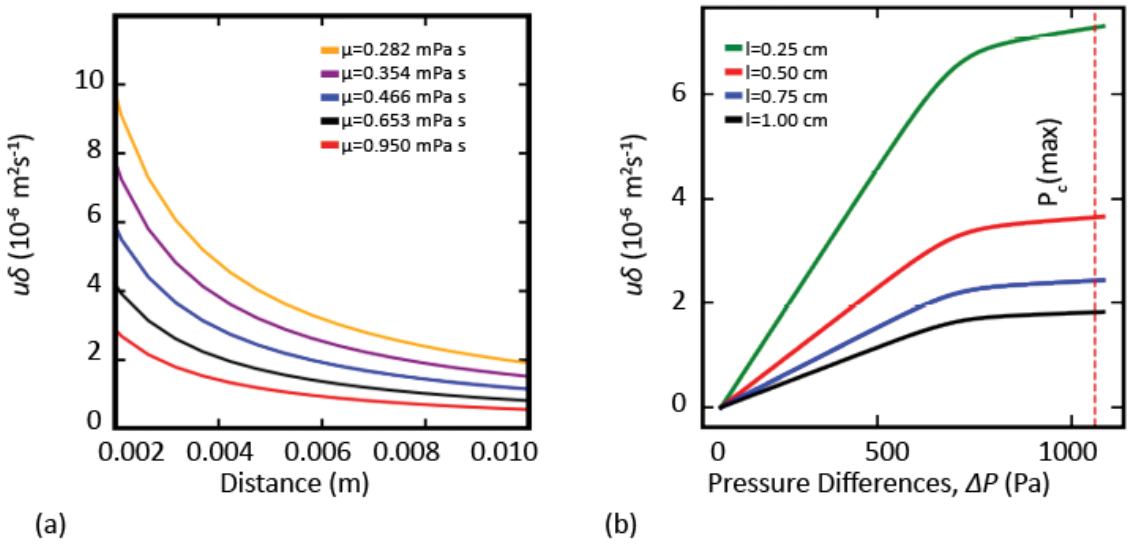

Figure 2.8 **(a)** Superficial velocity through a single layer free standing mesh wick, $u\delta$ (m^2s^{-1}), decreases with increasing wicking distance at maximum capillary pressure. Longer wicking lengths experience more considerable viscous drag compared to shorter wicking lengths. uδ of DI water is thus lower for longer wicking lengths than that of shorter wicking lengths. **(b)** $u\delta$ (m^2s^{-1}) vs. pressure difference, ΔP (Pa), at different wicking lengths. The red-dotted straight line indicates the maximum capillary pressure, $P_c(max)$.

Furthermore, we consider the nondimensionalized version of Equation (2.9) (see the supplementary section SM.(II)'s Equation (SM2)) to evaluate the performance of two common fluids used in electronics cooling applications HFO1233zd (at 25 ^{0}C surface tension, σ = 12.57 mN/m and dynamic viscosity, μ = 0.469 mPa.s, $\theta \sim 0^0$) and HFE7100 (at 25 ^{0}C surface tension, σ = 13.345 mN/m and dynamic viscosity, μ = 0.58 mPa.s, $\theta \sim 0^0$), in plain weaved single layer copper #100 mesh with 0.114 mm wire diameter. [46,47],[48] **Figure 2.9 (a)** shows the values of $u\delta$, at maximum driving pressure for dynamic viscosities of 0.469 mPa s **(**HFO1233zd) and 0.581 mPa s (HFE7100). Due to the lower surface tension of these fluids than DI water at similar temperature, the maximum driving force (pressure difference) we can apply is significantly lower than that of DI water. **Figure 2.9 (b)** shows the behavior of $u\delta$ for HFO1233zd and HFE7100 in #100 mesh at wicking lengths of l = 0.25 cm. $u\delta$ increases with driving pressure differences. (There is a marginally higher $P_c(max)$ for HFO1233zd than HFE7100).

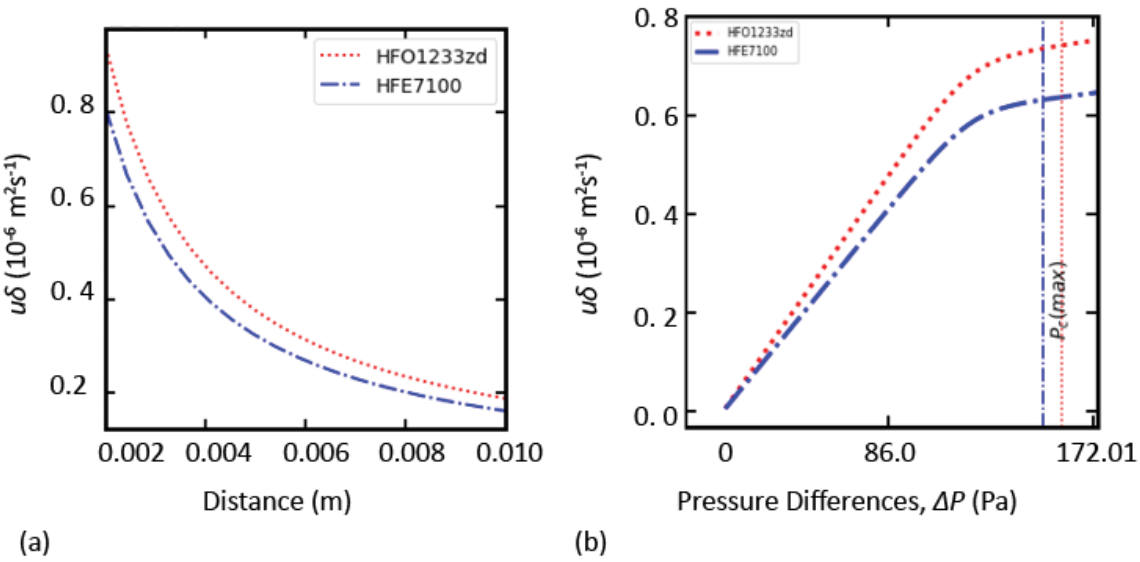

Figure 2.9 (a) $u\delta$ (m^2s^{-1}) with increasing wicking distance at maximum capillary pressure for common fluids used in electronics cooling application (HFO1233zd and HFE7100, respectively). **(b)** $u\delta$ (m^2s^{-1}) vs. pressure difference, ΔP (Pa), at wicking length of l = 0.25 cm for HFO1233zd and HFE7100, respectively. The red-dotted straight line indicates the maximum capillary pressure, $P_c(max)$ of HFO1233zd. The blue-dotted straight line indicates the maximum capillary pressure, $P_c(max)$ of HFE7100.

2.4.7 Comparison among methods to measure permeability of mesh geometries

Table 2-2 provides a comparison of permeability measurement methods and models applied to various mesh geometries. These include methods correlating flow and pressure drop [24][25][31] and rate of liquid imbibition into unsaturated samples.[49] We note that most methods are not suitable for measuring permeability-capillary pressure relationships. The method of Si Cong Tan et. al., used to measure the permeability-capillary pressure relationship of a thin mesh welded on a thin sheet, is an exception. However, this method cannot be easily modified to measure the permeability of a free-standing mesh where the mesh is exposed to liquid-vapor interface on both sides. The rate-of-rise method [1] is readily applied to free standing mesh structures. However, we note that there is ambiguity in comparing the rate-of-rise method, that determines the velocity of a saturation front, and the current method, that measures flow rate. A direct comparison requires a known cross-section for liquid flow, which is not precisely defined for free standing meshes, as discussed above. Additionally, the mesh considered here shows dramatic asymmetry in the rate of imbibition and drainage, as do various other porous materials, making the interpretation of rate of rise measurements ambiguous in these cases. The rate of rise method also does not provide direct information on capillary pressure dependence.

Table 2-2 Methods for measuring and calculating permeability for different mesh geometries

Method/ Geometry	**Mesh Number**	**Reported Permeability (m^2)**	**Applicable to free standing mesh**	**Capillary Pressure dependence**	**Ref.**
Flow with micropump/Single-layer Mesh Welded on plate[a]	150	2.2×10^{-11}	No	Yes	[31]
Gravity flow/Stacks of mesh[b]	150	5×10^{-11}	No	No	[24][25]
Capillary rate of rise/ Single-layer mesh welded on grooved plate	200	9.57×10^{-11}	Yes	No	[49]
Capillary rate of rise/ Two meshes stacked and sintered on plate	200	1.91×10^{-11}	Yes	No	[49]
Mathematical formula/N layers of mesh [c]	variable	variable	No	No	[50]
Rate of Rise/Single layer Dutch twill weave mesh	200/ 1400	Warp= 0.73×10^{-12} Weft = 0.36×10^{-12}	Yes	No	[51]
Siphon/Gravity flow/Single- layer free-standing mesh[d]	100	2.85×10^{-11}	Yes	Yes	This work

[a]Data for other mesh sizes #200, #250 with varying wire diameters 30,40,50 microns are also presented. Mesh material: Copper

[b]Data for other mesh sizes are also presented in [25][26]. Mesh materials: Stainless steel, phosphor bronze

[c]The formula for stacks of mesh

[d] Using mesh thickness of 0.280 mm for δ.

2.4.8 Validation of method

To validate the method described in this work, we compare the permeability of Whatman 1 filter paper at low capillary pressure obtained using a variety of approaches. We measure a permeability of 1.72 x 10^{-13} m^2 using the method presented here. Using the rate-of-rise method [1] on the Whatman 1 filter paper, we measure a permeability of 1.96 x 10^{-13} m^2. From the Herzberg number provided by the supplier [52] (100ml/150seconds) we calculate the permeability as 1.57 x 10^{-13} m^2. These permeability values are also consistent with the existing literature data on permeability of Whatman 1 filter paper: 1.41 x 10^{-13} m^2. in [33] and 2.01 x 10^{-13} m^2 in [53]. Details of the permeability measurements conducted on filter paper are discussed in supporting materials section SM.(V).

2.5 Conclusions

We proposed and demonstrated a novel and simple experimental technique that can be used to measure the permeability of free-standing mesh wicks with liquid-vapor interfaces on both sides of the wicks. Our experimental approach used water pools at different heights to create a driving force based on gravitational potential, allowing for liquid capillary suction through the mesh. To ensure accurate results, a surface cleaning protocol was established to clean the surfaces of the copper mesh from any organic debris. The meshes were thoroughly saturated with deionized (DI) water before the experiments and

operated in the drainage regime. To determine the maximum capillary pressure obtained from the metal meshes, a capillary rise test was conducted. Additionally, an environmental control chamber was used to conduct the experiments at 100% relative humidity to eliminate any effect of evaporation on the measurements. Importantly, this method does not require visual monitoring or a micropump for fluid flow, making it a cost-effective and efficient way to measure the permeability of mesh wicks.

Furthermore, this accessible set-up method couples the permeability with capillary pressure in mesh wicks. We report the change in permeability with capillary pressure in single layer free-standing mesh like structure by a correlation equation. The wicks show an essentially bistable response to capillary pressure. Flow resistance is essentially constant at low capillary pressures, then increases dramatically before stabilizing at high capillary pressure. We consider the generalization of these results to plain weave meshes of other scales and different fluids by dimensional analysis. We also calculate the flow behavior of meshes under specific conditions based on the observed flow resistance/capillary pressure relationship and the integration of Darcy’s law. By integrating Darcy's law, we calculated the flow velocity profile of DI water in metal mesh wicks using the correlation function we found through our experiment. The superficial velocity of water in copper mesh increases linearly until, at higher capillary pressures, the velocity increase goes down. At maximum capillary pressure, the superficial velocity of water decreases hyperbolically as the meniscus travels along the wicking length. The nondimensionalized permeability-capillary pressure relationship can be used to understand these materials' properties for any mesh sizes with similar weave and materials.

The methods and observations discussed are vital for designing and synthesizing devices that use single-layer, free-standing mesh structures for applications in which the permeability of the structures is affected by capillary

pressure. These applications include two-phase heat transfer for electronics cooling, electrochemical energy conversion devices, and deionization cells for water purification.

2.6 Acknowledgements

This research was supported by funding from the Advanced Research Projects Agency-Energy (ARPA-E), an agency of the United States Government, U.S. Department of Energy, under Award Number DE-AR0001055 in the OPEN program monitored by Dr. Peter de Bock. The authors acknowledge the Imaging and Microscopy Facility (IMF) at UC Merced (funded under NSF EAR Award number: 0420982) for use of the SEM instrument. MS would like to thank Kennedy Nguyen for helpful discussions on electron microscopy. Additionally, MS appreciates Brandon Yang, Carson Whitt, George Montross, Kamila Ramirez, Carlos Cruz, and Amani Byron for their help with sample preparation; and Qianying Wu for help with literature search. This paper's views, opinions, and findings are those of the authors. This work was co-authored by the National Renewable Energy Laboratory (NREL), operated by Alliance for Sustainable Energy, LLC, for the U.S. Department of Energy (DOE) under Contract No. DE-AC36-08GO28308. This work was supported by ARPA-E funding. The views expressed in the article do not necessarily represent the views of the DOE or the U.S. Government. The U.S. Government retains and the publisher, by accepting the article for publication, acknowledges that the U.S. Government retains a nonexclusive, paid-up, irrevocable, worldwide license to publish or reproduce the published form of this work, or allow others to do so, for U.S. Government purposes.

2.7 References

[1] B. Holley, A. Faghri, Permeability and effective pore radius measurements for heat pipe and fuel cell applications, Appl. Therm. Eng. 26 (2006) 448–462. https://doi.org/10.1016/j.applthermaleng.2005.05.023.

[2] C. Salameh, D. Voiry, Sieving in order, Nat. Mater. 21 (2022) 1106–1107. https://doi.org/10.1038/s41563-022-01351-w.

[3] J. Shen, Y. Cai, C. Zhang, W. Wei, C. Chen, L. Liu, K. Yang, Y. Ma, Y. Wang, C.C. Tseng, J.H. Fu, X. Dong, J. Li, X.X. Zhang, L.J. Li, J. Jiang, I. Pinnau, V. Tung, Y. Han, Fast water transport and molecular sieving through ultrathin ordered conjugated-polymer-framework membranes, Nat. Mater. 21 (2022) 1183–1190. https://doi.org/10.1038/s41563-022-01325-y.

[4] D. Salvatori, B. Caglar, H. Teixidó, V. Michaud, Permeability and capillary effects in a channel-wise non-crimp fabric, Compos. Part A Appl. Sci. Manuf. 108 (2018) 41–52. https://doi.org/10.1016/J.COMPOSITESA.2018.02.015.

[5] D. May, A. Aktas, S.G. Advani, D.C. Berg, A. Endruweit, E. Fauster, S. V. Lomov, A. Long, P. Mitschang, S. Abaimov, D. Abliz, I. Akhatov, M.A. Ali, T.D. Allen, S. Bickerton, M. Bodaghi, B. Caglar, H. Caglar, A. Chiminelli, N. Correia, B. Cosson, M. Danzi, J. Dittmann, P. Ermanni, G. Francucci, A. George, V. Grishaev, M. Hancioglu, M.A. Kabachi, K. Kind, M. Deléglise-Lagardère, M. Laspalas, O. V. Lebedev, M. Lizaranzu, P.J. Liotier, P. Middendorf, J. Morán, C.H. Park, R.B. Pipes, M.F. Pucci, J. Raynal, E.S. Rodriguez, R. Schledjewski, R. Schubnel, N. Sharp, G. Sims, E.M. Sozer, P. Sousa, J. Thomas, R. Umer, W. Wijaya, B. Willenbacher, A. Yong, S. Zaremba, G. Ziegmann, In-plane permeability characterization of engineering textiles based on radial flow experiments:

A benchmark exercise, Compos. Part A Appl. Sci. Manuf. 121 (2019) 100–114. https://doi.org/10.1016/J.COMPOSITESA.2019.03.006.

[6] J.W. Palko, C. Zhang, J.D. Wilbur, T.J. Dusseault, M. Asheghi, K.E. Goodson, J.G. Santiago, Approaching the limits of two-phase boiling heat transfer: High heat flux and low superheat, Appl. Phys. Lett. 107 (2015). https://doi.org/10.1063/1.4938202.

[7] C. Zhang, J.W. Palko, M.T. Barako, M. Asheghi, J.G. Santiago, K.E. Goodson, Enhanced Capillary-Fed Boiling in Copper Inverse Opals via Template Sintering, Adv. Funct. Mater. 28 (2018) 1–8. https://doi.org/10.1002/adfm.201803689.

[8] Y. Song, H. Cha, Z. Liu, J.H. Seong, L. Zhang, D.J. Preston, E.N. Wang, Alteration of pool boiling heat transfer on metallic surfaces by in situ oxidation, Int. J. Heat Mass Transf. 185 (2022). https://doi.org/10.1016/j.ijheatmasstransfer.2021.122320.

[9] M.M. Rahman, M. McCarthy, Effect of Length Scales on the Boiling Enhancement of Structured Copper Surfaces, J. Heat Transfer. 139 (2017) 1–9. https://doi.org/10.1115/1.4036693.

[10] M.M. Rahman, E. Ölçeroglu, M. McCarthy, Role of wickability on the critical heat flux of structured superhydrophilic surfaces, Langmuir. 30 (2014) 11225–11234. https://doi.org/10.1021/la5030923.

[11] C. Li, G.P. Peterson, Y. Wang, Evaporation/boiling in thin capillary wicks (I) - Wick thickness effects, J. Heat Transfer. 128 (2006) 1312–1319. https://doi.org/10.1115/1.2349507.

[12] C. Li, G.P. Peterson, Evaporation/boiling in thin capillary wicks (II) - Effects of volumetric porosity and mesh size, J. Heat Transfer. 128 (2006) 1320–1328. https://doi.org/10.1115/1.2349508.

[13] N. Lu, J. Li, Y. Sun, Research Progress and Prospect of Heat Pipe Capillary Wicks, Front. Heat Mass Transf. 18 (2022). https://doi.org/10.5098/hmt.18.24.

[14] C. Byon, S.J. Kim, The effect of meniscus on the permeability of micro-post arrays, J. Micromechanics Microengineering. 21 (2011). https://doi.org/10.1088/0960-1317/21/11/115011.

[15] R. Schulz, N. Ray, S. Zech, A. Rupp, P. Knabner, Beyond Kozeny–Carman: Predicting the Permeability in Porous Media, Transp. Porous Media. 130 (2019) 487–512. https://doi.org/10.1007/s11242-019-01321-y.

[16] Y. Nam, S. Sharratt, C. Byon, S.J. Kim, Y.S. Ju, Fabrication and characterization of the capillary performance of superhydrophilic Cu micropost arrays, J. Microelectromechanical Syst. 19 (2010) 581–588. https://doi.org/10.1109/JMEMS.2010.2043922.

[17] A. Wagner, E. Eggenweiler, F. Weinhardt, Z. Trivedi, D. Krach, C. Lohrmann, K. Jain, N. Karadimitriou, C. Bringedal, P. Voland, C. Holm, H. Class, H. Steeb, I. Rybak, Permeability Estimation of Regular Porous Structures: A Benchmark for Comparison of Methods, Transp. Porous Media. 138 (2021). https://doi.org/10.1007/s11242-021-01586-2.

[18] A. Faghri, Y. Zhang, SOLID-LIQUID-VAPOR PHENOMENA AND INTERFACIAL HEAT AND MASS TRANSFER, Transp. Phenom. Multiph. Syst. (2006) 331–420. https://doi.org/10.1016/B978-0-12-370610-2.50010-6.

[19] F.A.L. Dullien, Porous Media: Fluid Transport and Pore Structure, Academic Press, 1992.

[20] T.A. Ghezzehei, T.J. Kneafsey, G.W. Su, Correspondence of the Gardner and van Genuchten-Mualem relative permeability function parameters,

Water Resour. Res. 43 (2007) 1–7. https://doi.org/10.1029/2006WR005339.

[21] P. Papatzacos, S.M. Skjæveland, Relative Permeability from Capillary Pressure, Proc. - SPE Annu. Tech. Conf. Exhib. (2002) 1841–1851. https://doi.org/10.2118/77540-ms.

[22] J.D. Valiantzas, Combined Brooks-Corey/Burdine and van Genuchten/Mualem Closed-Form Model for Improving Prediction of Unsaturated Conductivity, J. Irrig. Drain. Eng. 137 (2011) 223–233. https://doi.org/10.1061/(asce)ir.1943-4774.0000284.

[23] L. Makkonen, A thermodynamic model of contact angle hysteresis, J. Chem. Phys. 147 (2017). https://doi.org/10.1063/1.4996912.

[24] Y. Ikeda, Permeability of a screen wick, in: Proc. Sumpos. Mech. Sp. Flight, Proceedings of the Sumposium on Mechanics for Space Flight, 1985: pp. 119–125.

[25] H. Kozai, I. Imura, Y. Ikeda, The Permeability of Screen Wicks, JSME Int. J. 34 (1991) 212–219. http://www.mendeley.com/research/geology-volcanic-history-eruptive-style-yakedake-volcano-group-central-japan/.

[26] H. Noda, K. Yoshioka, T. Hamatake, Experimental study on the permeability of screen wicks, JSME Int. Journal, Ser. B Fluids Therm. Eng. 36 (1993) 357–363. https://doi.org/10.1299/jsmeb.36.357.

[27] B. Subedi, S.H. Kim, S.P. Jang, M.A. Kedzierski, Effect of mesh wick geometry on the maximum heat transfer rate of flat-micro heat pipes with multi-heat sources and sinks, Int. J. Heat Mass Transf. 131 (2019) 537–545. https://doi.org/10.1016/j.ijheatmasstransfer.2018.11.086.

[28] D.R. Adkins, R.C. Dykhuizen, Procedures for measuring the properties of heat-pipe wick materials, Proc. Intersoc. Energy Convers. Eng. Conf. 2

(1993) 911–917.

[29] A. Arulselvan, N. Ramasubbu, V. Pandiyarajan, Experimental investigations on the effect of using distilled water in a heat pipe with copper screen wick, AIP Conf. Proc. 2161 (2019). https://doi.org/10.1063/1.5127601.

[30] J.H. Ambrose, L.C. Chow, J.E. Beam, Capillary flow properties of mesh wicks, J. Thermophys. Heat Transf. 4 (1990) 318–324. https://doi.org/10.2514/3.183.

[31] S.C. Tan, C. Guo, Y.Y. Jiang, T. Wang, C.Z. Li, Investigation on permeability of ultra-thin screen wick with free surface using gravity flow and numerical simulation methods, Int. Commun. Heat Mass Transf. 131 (2022) 105879. https://doi.org/10.1016/j.icheatmasstransfer.2022.105879.

[32] G. Rong, J.W. Palko, D.I. Oyarzun, C. Zhang, J. Hämmerle, M. Asheghi, K.E. Goodson, J.G. Santiago, A method for quantifying in plane permeability of porous thin films, J. Colloid Interface Sci. 530 (2018) 667–674. https://doi.org/10.1016/j.jcis.2018.05.062.

[33] S. Patari, P. Sinha Mahapatra, Imbibition of Liquids through a Paper Substrate in a Controlled Environment, Langmuir. 38 (2022) 4736–4746. https://doi.org/10.1021/acs.langmuir.2c00318.

[34] L.M. Skinner, J.R. Sambles, The Kelvin equation-a review, J. Aerosol Sci. 3 (1972) 199–210. https://doi.org/10.1016/0021-8502(72)90158-9.

[35] F.J. Granados-Ortiz, A. López-Martínez, F.D. Molina-Aiz, C.H. Lai, A. Peña-Fernández, J.A. Martínez-Lao, D.L. Valera-Martínez, Improvements in the Characterisation of Permeability and Inertial Factor of Insect-Proof Screens through Pressure Drop Coefficients, Agronomy. 13 (2023). https://doi.org/10.3390/agronomy13020602.

[36] F.A.L. DULLIEN, Capillarity in Porous Media, Porous Media. (1992) 117–236. https://doi.org/10.1016/B978-0-12-223651-8.50008-0.

[37] H.J. Cho, D.J. Preston, Y. Zhu, E.N. Wang, Nanoengineered materials for liquid-vapour phase-change heat transfer, Nat. Rev. Mater. 2 (2016) 1–17. https://doi.org/10.1038/natrevmats.2016.92.

[38] F.A.L. Dullien, M.S. El-Sayed, V.K. Batra, Rate of capillary rise in porous media with nonuniform pores, J. Colloid Interface Sci. 60 (1977) 497–506. https://doi.org/10.1016/0021-9797(77)90314-9.

[39] H.P.J. De Bock, K. Varanasi, P. Chamarthy, T. Deng, A. Kulkarni, B.M. Rush, B. a Russ, S.E. Weaver, F.M. Gerner, Experimental Investigation of Micro/Nano Heat Pipe Wick Structures, in: Proc. IMECE2008, 2008: pp. 1–6.

[40] M. Shattique, K. Ramirez, G. Montross, A. Byron, C. Cruz, R. Giglio, E.M. Dede, M. Asheghi, K.E. Goodson, J.W. Palko, Immiscible Fluid Disposition and Permeability in Thin Porous Structures, in: APS March Meet., 2023. https://march.aps.org/sessions/K18/3.

[41] E.M. Dede, C. Zhang, Q. Wu, N. Seyedhassantehrani, M. Shattique, S. Roy, J.W. Palko, S. Narumanchi, B. Kekelia, S. Hazra, K.E. Goodson, R. Giglio, M. Asheghi, Techno-economic feasibility analysis of an extreme heat flux micro-cooler, IScience. 26 (2023) 105812. https://doi.org/10.1016/j.isci.2022.105812.

[42] M.E. Schrader, Wettability of clean metal surfaces, J. Colloid Interface Sci. 100 (1984) 372–380. https://doi.org/10.1016/0021-9797(84)90442-9.

[43] D.Y. Kwok, D. Li, A.W. Neumann, Fowkes' surface tension component approach revisited, Colloids Surfaces A Physicochem. Eng. Asp. 89 (1994) 181–191. https://doi.org/10.1016/0927-7757(94)80117-7.

[44] D.Y. Kwok, A.W. Neumann, Contact angle measurement and contact angle interpretation, 1999. https://doi.org/10.1016/S0001-8686(98)00087-6.

[45] F.M. Fowkes, Additivity of Intermolecular Forces At Interfaces. I. Determination of the Contribution To Surface and Interfacial Tensions of Dispersion Forces in Various Liquids 1 , J. Phys. Chem. 67 (1963) 2538–2541. https://doi.org/10.1021/j100806a008.

[46] R.J. Hulse, R.S. Basu, R.R. Singh, R.H.P. Thomas, Physical Properties of HCFO-1233zd (E), J. Chem. Eng. Data. 57 (2012) 3581–3586.

[47] M.H. Rausch, L. Kretschmer, S. Will, A. Leipertz, A.P. Fröba, Density, surface tension, and kinematic viscosity of hydrofluoroethers HFE-7000, HFE-7100, HFE-7200, HFE-7300, and HFE-7500, J. Chem. Eng. Data. 60 (2015) 3759–3765. https://doi.org/10.1021/acs.jced.5b00691.

[48] S.N. Joshi, F. Zhou, Y. Liu, D.J. Lohan, J. Lee, E.M. Dede, S. Member, A review of select patented technologies for cooling of high heat flux power semiconductor devices, IEEE Trans. Power Electron. PP (2023) 1–5. https://doi.org/10.1109/TPEL.2023.3243546.

[49] S.C. Wong, M.S. Deng, M.C. Liu, Characterization of composite mesh-groove wick and its performance in a visualizable flat-plate heat pipe, Int. J. Heat Mass Transf. 184 (2022) 122259. https://doi.org/10.1016/j.ijheatmasstransfer.2021.122259.

[50] A. Faghri, Heat Pipe Science and Technology, Taylor & Francis Ltd, 1995.

[51] N. Fries, K. Odic, M. Conrath, M. Dreyer, The effect of evaporation on the wicking of liquids into a metallic weave, J. Colloid Interface Sci. 321 (2008) 118–129. https://doi.org/10.1016/j.jcis.2008.01.019.

[52] G.E. Healthcare, L. Sciences, Laboratory filtration Principles and chemical compatibility chart, (2016).

[53] Z. Liu, J. Hu, Y. Zhao, Z. Qu, F. Xu, Experimental and numerical studies on liquid wicking into filter papers for paper-based diagnostics, Appl. Therm. Eng. 88 (2015) 280–287. https://doi.org/10.1016/j.applthermaleng.2014.09.057.

[54] B.M. Cummins, R. Chinthapatla, F.S. Ligler, G.M. Walker, Time-Dependent Model for Fluid Flow in Porous Materials with Multiple Pore Sizes, Anal. Chem. 89 (2017) 4377–4381. https://doi.org/10.1021/acs.analchem.6b04717.

[55] D. Deng, Y. Tang, G. Huang, L. Lu, D. Yuan, Characterization of capillary performance of composite wicks for two-phase heat transfer devices, Int. J. Heat Mass Transf. 56 (2013) 283–293. https://doi.org/10.1016/j.ijheatmasstransfer.2012.09.002.

[56] A. Elkholy, J. Durfee, J.P. Mooney, A.J. Robinson, R. Kempers, A rate-of-rise facility for measuring properties of wick structures, Meas. Sci. Technol. 34 (2023). https://doi.org/10.1088/1361-6501/acad1c.

[57] C.T. Yeh, W.H. Tuan, Oxidation mechanism of aluminum nitride revisited, J. Adv. Ceram. 6 (2017) 27–32. https://doi.org/10.1007/s40145-016-0213-1.

2.8 Supporting Materials

Permeability of Single-Layer-Free-Standing Meshes at Varying Capillary Pressure via a Novel Method

2.8.1 Comparison of Pressure Drops at Different Capillary Pressures

We calculate viscous pressure drop along the section of interest (L^* in the text) and compare it with capillary pressure for low (~490 Pa), medium(~686Pa) and high (~1000Pa) capillary pressure cases. For all cases, the ratio of viscous pressure drop in the section of interest to capillary pressure is <25% (**Figure 2.10 SM1**.).

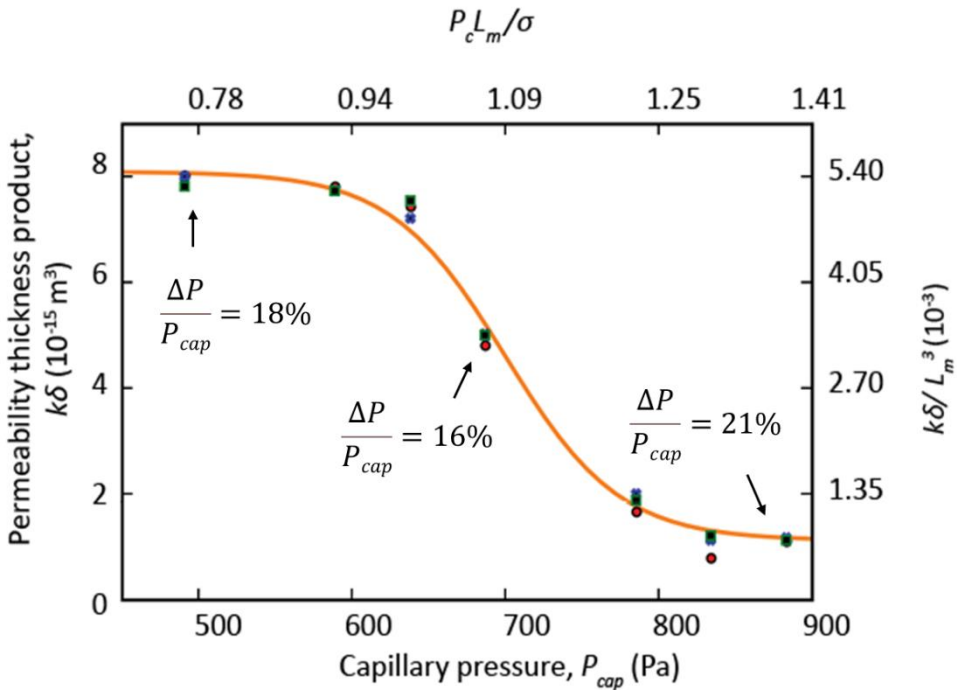

Figure 2.10 SM1. Ratio of viscous pressure drop across region of interest and capillary pressures for three capillary pressure cases: low (~490 Pa), medium(~686Pa) and high (~882Pa).

2.8.2 Dimensional Analysis

Volume flow rate, v' is inversely proportional to wick length, the viscosity of the fluid, and proportional to the width of the wick and pressure drop along the wick. We can write,

$$\frac{\frac{v'}{w}\mu L}{\Delta P} = k\delta = f'(\sigma, L_m, P_c) \quad \text{(SM1)}$$

3 dimensions (M, L, T)

4 variables ($k\delta, \sigma, L_m, P_{cap}$)

π Buckingham's = (# of vars) – (# of primary dimension) = 4-3 = 1

$$\frac{k\delta}{L_m^3} = f'\left(\frac{P_c L_m}{\sigma}\right)$$

Nondimensionalized version of Equation (9)

$$\frac{u\delta\mu l}{\sigma L_m^2} = \frac{(a+d)}{\sigma L_m^2}\Delta P - \frac{a}{b\sigma L_m^2} ln\left(e^{b(\Delta P - c)} + 1\right) + \frac{p_0}{\sigma L_m^2} \quad \text{(SM2)}$$

2.8.3 Measurement of Porosity of Copper Mesh (#100)

Porosity,

$$\phi = \frac{v_{pore}}{v_{total}} = \frac{v_{total} - v_{solid}}{v_{total}} = 1 - \frac{v_{solid}}{v_{total}} = = 1 - \frac{\rho_{Cu} v_{solid}}{\rho_{Cu} v_{total}} = 1 - \frac{m_{mesh}}{\rho_{Cu}\delta A_{total}} \quad \text{(SM3)}$$

For copper (#100) mesh described in section 2.1 ($\rho_{Cu} = 8960\,\frac{kg}{m^3}$), we cut a 1 cm^2 section and measured the mass using a microbalance, $m_{mesh} = 0.0873\ x\ 10^{-3}\ kg$.

From Equation (SM3) Porosity, $\phi = 65\%$.

2.8.4 Application to other porous structures

For non-ductile porous samples like glass, ceramics, and hard metals/polymers, any mechanical deformation can alter the internal pore structure. To measure permeability of other thin, porous structures that are not amenable to bending, a standardized wick may be used to transmit liquid to and from the region of interest. This approach avoids bending/mechanical deformation of samples. **Figure 2.11 SM2** provides a schematic for measurements using a composite setup.

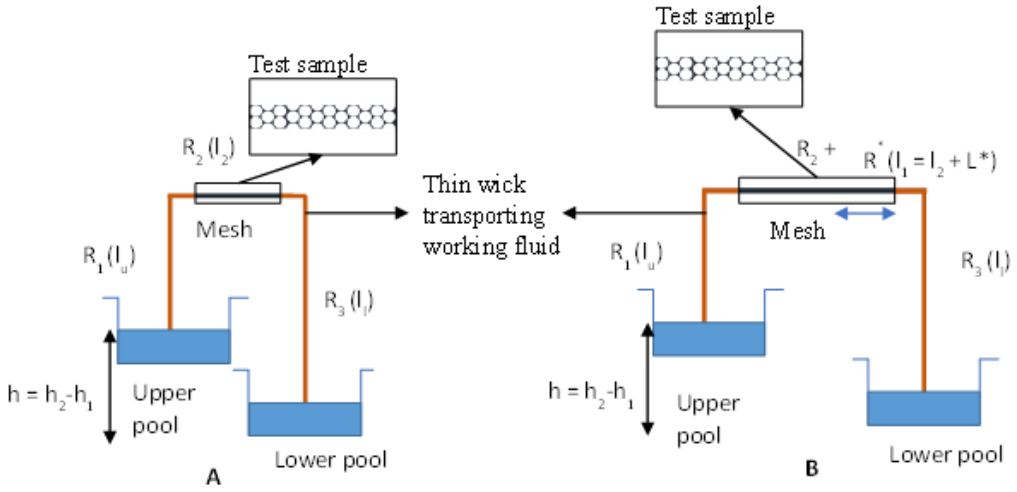

Figure 2.11 SM2. Schematic of measuring permeability-capillary pressure relationship of various thin porous structures using a composite wick.

2.8.5 Cross validation of the method with rate-of-rise method for intrinsic permeability

We performed permeability measurement of Whatman 1 paper through the siphon bridge method resulting in a measured permeability of k = 1.718 x 10^{-13} m^2. The paper thickness in a dry state is 180 µm and after wetting and swelling is 230 µm. The porosity of the Whatman 1 paper is taken as 67.4% [54]. The length

of L* = 1.5 cm. Width of the paper is 1 cm. Pool height difference is 1 cm. The experiment is conducted for 1.5 hours. The relative humidity is controlled to ~100%. The mass of the water pools is measured before and after the experiments to calculate the volumetric flow rates and the resulting permeability-thickness product is obtained from Equation (5) and then divided by the thickness of the swelled paper to determine permeability.

We also conducted a rate of rise[55][1,56] test to measure permeability of Whatman 1 paper to validate our method. A strip of 1 cm width and 10 cm length was hung vertically, and the bottom end dipped in a water pool. The sample was marked with a laser ablator every 0.5 mm to visually measure the height of rise. We captured the rise height vs time with a camera (15fps) for 72 seconds. We then converted the recorded video to a series of single frames for analysis. We fit the height versus time data with the model provided in Holey and Faghri [1,56], Equations SM4, SM5 using a least square method via Python's SciPy.Optimize package and the curve_fit function (**Figure 2.12 SM.3**).

$$- [2\frac{\sigma}{r_e} ln\left(1 - \frac{\rho g r_e}{2\sigma} h\right) + \rho g h] = \frac{k\rho^2 g^2}{\varepsilon\mu} t \qquad \text{(SM4)}$$

Solving for time we find,

$$t = - \frac{\varepsilon\mu}{k\rho^2 g^2} [2\frac{\sigma}{r_e} ln\left(1 - \frac{\rho g r_e}{2\sigma} h\right) + \rho g h] \qquad \text{(SM5)}$$

From the fit we find, k = 1.96 x 10^{-13} m^2 , and effective pore radius, r_e = 19.9 μm.

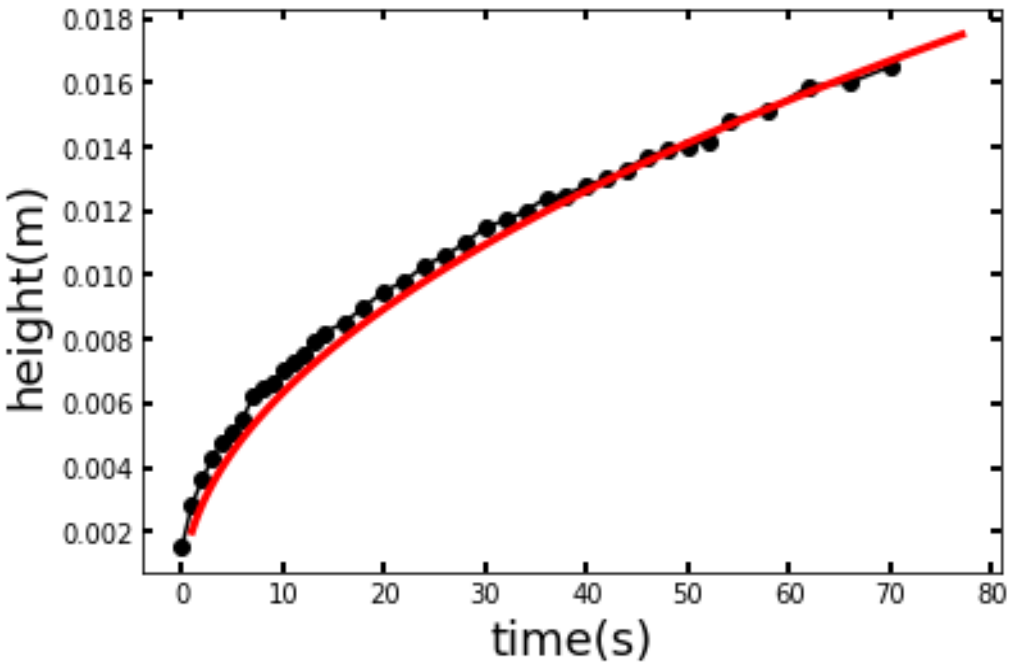

Figure 2.12 SM3. Plot of height(m) versus time(s) from a rate of rise experiment of Whatman 1 filter paper. Black dots represent experimental data. The data were fit with Equation (SM4) using a least square method as shown by the red solid line.

Our measured permeability numbers are then compared with existing literature data [33,53] and found to be in reasonable agreement.

Chapter 3

Permeability-Capillary Pressure Relationship of a Surface Modified Single Layer-Free Standing Copper Mesh

3.1 Introduction

Surface properties of porous materials are crucial for chemical, physical, and biological processes. [1], [2] For capillary driven transport in porous materials, texturing can tune the wettability of a surface for specific application resulting to desired capillary pressure and permeability. Surface texturing of porous metallic materials can be achieved either by subtractive (e.g., through chemical/dry etching, laser interaction) or additive processes (e.g., growing oxide microstructures, lithography of nanostructures).

While lithography, self-assembly of molecules, have been widely used to process nano/micropatterning[3] [4], for bulk processing of complex shaped porous materials, practical methods are required for mass adoption where batches of the bulk porous material can be surface treated in a one-step bulk processing route. Here, we focus on adding microstructures of a free-standing copper mesh that can be applied to two-phase heat transfer process using capillary fluid delivery. From existing literature review, we found multiple reports of using copper surfaces to generate micro- and nanoscale copper oxide *needles* as a facile surface texturing technique, among many other shapes. [5]–[8] We identified that, one of the primary challenges in the process of incorporating tiny *needle-like* oxide structures into a complex network of pores is to regulate their surface characteristics without impeding the structure's ability to transport mass efficiently. To illustrate, when thick metal oxide nanostructures are added to porous materials with micrometer to sub micrometer-sized pores, they can potentially block these pores and obstruct the flow of substances. Thus, for surface modification, achieving uniform copper oxide deposition along pore surfaces, preserving fluid-permeable pathways with a thin oxide layer, and maintaining stable hydrophilicity under varying environmental conditions are desired. For adding *needle-like* copper microstructures on a porous copper three major categories of surface texturing techniques may be identified: thermal, chemical, and electrochemical processes.

3.1.1 Thermal oxidation in air of copper

The effects of processing parameters on thermal growth of copper oxides have been investigated in detail by [9].By exposing the material to high temperature for various times, thermal oxidation can be used to texture surfaces. For instance, Cu_2O is formed after a relatively brief treatment of about 30 minutes at a lower temperature of 110°C, which gives the material an orange tint. In contrast, CuO, which is distinguished by its black hue, is formed when the material is heated at or above 300°C for 60 to 80 minutes. The hydrophilic nature of this CuO surface increases its affinity for water. The yield and size distribution of thermally oxidized copper have been shown to be significantly impacted by a number of synthesis parameters, including temperature, time, airflow, and others. Typically, the synthesis of oxide microstructures takes place between 200^0 C and 500^0 C. Due to an accelerated rate of copper oxidation, synthesis that takes place in the presence of water vapor typically produces micro/nanostructures that are longer and thinner. **Figure 3. 1**.

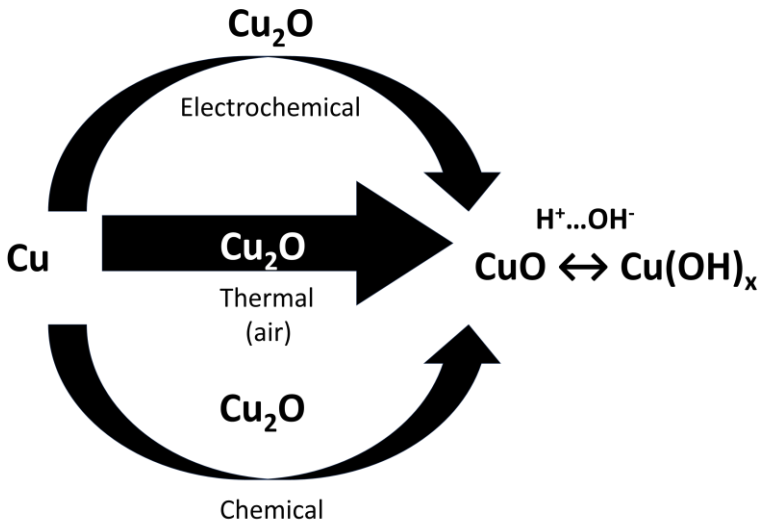

Figure 3.1 Several routes to process copper oxide micro-structures. Cuprous oxide (Cu_2O) is often an intermediate step during the processing. The final microstructure can be a combination of CuO, Cu_2O, and Cu $(OH)_2$, in an aqueous environment.

3.1.2 Chemically modifying copper surface

Another method involves chemical treatment for the growth of metal oxides. Two methods developed that has shown success in achieving stable growth of oxide needle like structures are discussed by the investigation of [10]shown success in achieving stable growth of oxide *needle-like* structures. The first formula employs a solution containing NaOH (5g), $NaClO_2$ (3.75g), Na_2PO_4 .12 H_2O (10g), and 100 ml of water, heated to 100°C. This solution yields elongated structures resembling grass, with dimensions reaching up to 1 micron. In contrast, the second formula involves NaOH (5g), $NaClO_2$ (16g), and 100 ml of deionized (DI) water, and then heated to 100°C, resulting in the growth of comparatively shorter *grass-like* structures, measuring 100 nm in dimensions on average.

3.1.3 Modifying copper surface via electro-oxidation

An alternative approach to achieving surface modification involves electrochemical methods, which offer enhanced control over the uniform structuring of curved surfaces. Copper, in this case, undergoes oxidation in a basic solution, akin to the anodizing process employed for aluminum. Numerous combinations of electrolytes, potentials, and currents have been documented for the anodizing of copper, reflecting the diversity of techniques and strategies in this realm.[5] Unlike anodizing of aluminum the anodizing of copper may result to a combination of oxides and hydroxides (CuO, Cu_2O, $Cu(OH)_2$)[5], [7], [11]–[13]

Electrochemical copper oxidation can give rise to the formation of both Cu_2O and CuO, with CuO being generated through the oxidation of both copper and Cu_2O. Consequently, the initial phase of copper anodization involves the creation of Cu_2O **Figure 3.2**, represented by the electrochemical and chemical reactions outlined in Equations (i) to (iii):

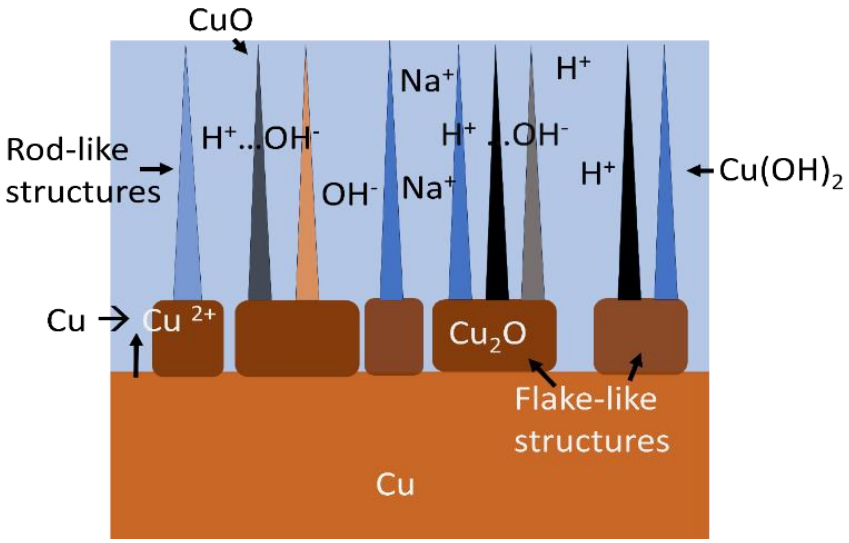

Figure 3.2 Anodizing of copper in an aqueous solution. Several oxide microstructures form during the nucleation and growth stage.

$$Cu + OH^- = CuOH + e^- \quad \text{(i)}$$

$$2CuOH = Cu_2O + H_2O \quad \text{(ii)}$$

$$2\,Cu + 2\,OH^- = Cu_2O + H_2O + 2e^- \quad \text{(iii)}$$

In subsequent stages, both Cu_2O and CuO are directly formed via the oxidation of metallic copper. Simultaneously, Cu_2O undergoes successive conversion into Cu(I) species and can be partially transformed into CuO through the reactions described in Equations (iv) to (vii):

$$Cu_2O + 2OH^- + H_2O \rightarrow 2\,Cu(OH)_2 + 2e^- \quad \text{(iv)}$$

$$CuOH + OH^- + H_2O \rightarrow Cu(OH)_2 + e^- \quad \text{(v)}$$

$$Cu + 2OH^- \rightarrow Cu(OH)_2 + 2e^- \quad \text{(vi)}$$

$$Cu + 2OH^- \rightarrow CuO + H_2O + 2e^- \quad \text{(vii)}$$

Following these stages, the growth of copper oxides and hydroxides continues, leading to the consumption of copper for the formation of both Cu (I) and Cu (II) compounds, with partial utilization of Cu(I) to generate Cu (II) species. Additionally, a chemical equilibrium between $Cu(OH)_2$ and CuO at room temperature and pressure is also observed in the presence of water. An excellent work by Cudennec and Lecerf [14] describes this mechanism in detail.

The introduction of copper oxides as surface textures can impart differing surface energy characteristics. Consequently, a heterogenous modification of the surface's wettability is possible. Another possibility is hydrogen bonding between a polar fluid and the oxide surface The effect of concentration of alkaline electrolyte and the applied potential on the size of micro-rod/grass type structures are reported.[15] A blend of elevated electrical potential and reduced electrolyte concentration facilitates the creation of consistent and conformal copper oxide crystals at the nanoscale, approximately measuring 80 nm, along the curvature of the pores, with minimal alterations to the via diameters. Conversely, when employing a lower electrical potential (below 0.75 V) or higher electrolyte concentration, this process results in the formation of elongated copper hydroxide wires, ranging from 2 to 4 μm in length.

The electric field plays a role in determining the lengths, thicknesses, and shape of the microstructures because it promotes the diffusion of Cu and O ions along the growth direction of the nanowires, parallel to the external electric field. At lower concentration of the aqueous solvent, local depletion during copper oxide nucleation and growth process gives rise to long *rod like* structures aligned towards to the external field. On the contrary, in a high concentration of the solute the concentration depletion during the growth process is lower and the electric field strength is weaker giving rise to more *flower/flake like* structures of copper oxide.[6], [9], [16]

The surface wettability of the oxide surfaces is influenced by the heterogeneity of the chemical compositions and shape-and size of the copper oxides. Furthermore, the copper surfaces with grown oxide microstructures can trap tiny air pockets near the surface giving rise to a *Cassie-Baxter* state of wettability. [5], [17]While thermodynamic properties, such as contact angle and wettability, have been extensively studied in relation to these structures when in

contact with a liquid, to our knowledge, flow properties like permeability, especially the influence of capillary pressure on permeability within copper-meshes with surface oxide textures, are not well-studied. Dendritic microstructures have the promise of increasing surface wettability as well. We focused our process on the *needle like* structures in this work. The readers are encouraged to read the detailed work of H. Mehrabi *et al*. on the electrochemical modification of copper surfaces with hierarchical dendritic structures. [20] Furthermore, here we investigate the effect of capillary pressure of a copper mesh with micro-needles on its permeability.

3.2 Materials and Methods

In this section we describe an electrochemical method for growing copper oxide microneedles by oxidizing copper mesh in bulk:

3.2.1 Materials

We used copper mesh with similar geometry described in Chapter 2 as cathode and anode for the electro-oxidation step. For electrooxidation 1M NaOH (Sigma Aldrich) solution was prepared. Furthermore, we used chemical resistant plastic meshes as separators (McMaster Carr) between the electrodes. A TekPower model TP3005T is used as a power supply during the electrooxidation process. De- Ionized (DI) water is used to measure permeability.

3.2.2 Methods

Surface cleaning of as received copper mesh following the process in Table 2.1 in Chapter 2. Mass of meshes is measured using a microbalance (120g x 0.1mg, 0.0001g Lab Precision Scale).

An electrochemical cell described in **figure 3.3** is constructed for electro-oxidation of copper. The anode mesh, two layers of chemical resistant plastic

mesh and the cathode mesh are pressed and rolled and placed in beaker at ambient condition.

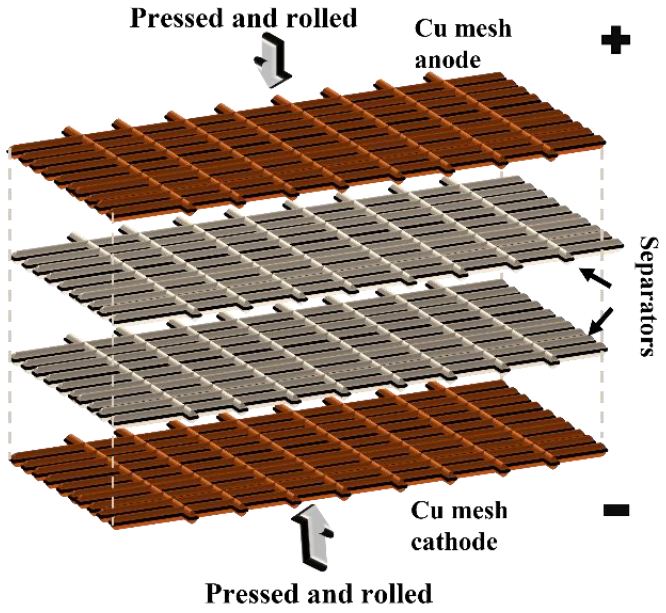

Figure 3.3 Electrooxidation of the copper mesh. Anode and cathode mesh are separated by plastic separators, pressed and rolled together for electrooxidation.

A cyclic electrooxidation method, where 600 mV of constant voltage is applied for 40 seconds and switched off for 20 seconds is carried out over 100 cycles. After the electrooxidation step, the oxidized mesh is cleaned in DI water and then dried under vacuum for 24 hours. The microstructure of the mesh is imaged by an SEM (Zeiss Gemini SEM 500). ImageJ software is used for image analysis. The permeability and maximum capillary pressure experimental setups and methods are described in Chapter 2, section 2.2.3, and section 2.3.2, respectively.

3.3 Results and discussions

In this section, the experimental findings of growing copper microneedles on a mesh, the resulting permeability-capillary pressure relationship and fluid flow modeling study in an electrooxidized copper mesh is discussed:

3.3.1 Surface area of pristine copper mesh

Electro-oxidized mesh with micro-needles has an increase in surface area than a pristine mesh. We can estimate the enhanced surface area from the surface area of a pristine mesh and an electro-oxidized mesh. treated copper mesh a pristine mesh. In this section we discuss the surface area of a pristine copper mesh.

We measure the mass of a 1 cm^2 copper (#100) mesh, m = 0.0722 g. The volume, V, of the copper mesh,

$$V = \frac{m}{\rho} \tag{3.1}$$

Where, ρ is the density of copper is 8.96 g/cm^3. Since the mesh is made of individual wires for *n* numbers of wires of length *l* in a mesh, individual wire radius of *r*, the volume of the mesh, $V = n\pi r^2 l$. Similarly, the surface area of the mesh, $SA = n2\pi rl$. The ratio of volume by surface area can be written as

$$\frac{V}{SA} = \frac{n\pi r^2 l}{n2\pi rl} = \frac{r}{2}$$

Surface area, $$SA = \frac{2V}{r} \tag{3.2}$$

The volume is determined by measuring the mass of 1 cm^2 mesh and dividing it by the density of copper. V = 0.0722/8.96 = 0.008 cm^3 . Wire radius of the mesh, r = 0.0057 cm.

From Equation 3.2 we can estimate the surface area of a 1 cm^2 pristine copper (#100) mesh,

$$SA = \frac{2\times 0{\cdot}008}{0.0057} = 2.8 \text{ cm}^2.$$

3.3.2 Surface morphology of the electrooxidized copper

From the SEM, **figure 3.4 (a)**, we observe the growth of *micro-needle* like structures on the copper mesh after the electro-oxidation process. **Figure 3.4 (b)** is an SEM of a larger magnification. The microneedles are oriented randomly.

The density of the needles= 2 needles/μm² (20,000 needles/cm²). From image analysis, we determined average height h = 2 μm, average base diameter d_b = 0.5 μm, and average tip diameter d_t = 0.18 μm. The needles are conical cylindrical in shape.

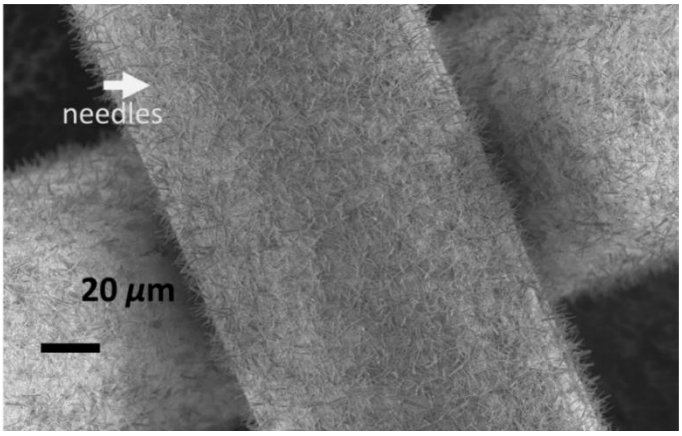

(a)

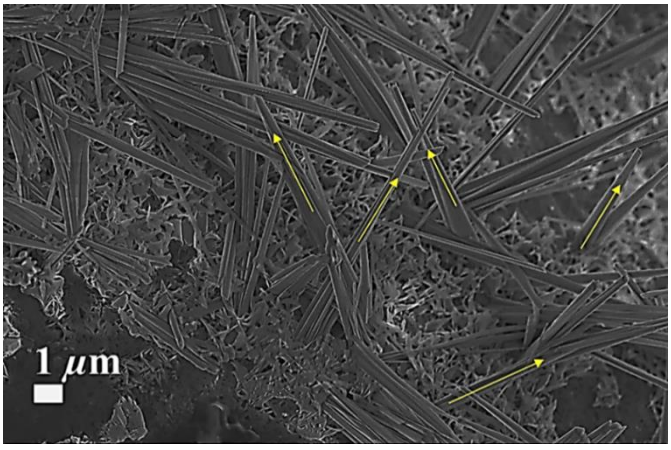

(b)

Figure 3.4 (a) SEM of CuO microneedles grown on copper mesh via electrooxidation in 1M NaOH solution. After the treatment, we grow microneedles on the body of the wires of the mesh. **(b)** from a higher magnification we observe that the needle orientations are random (yellow arrows are showing orientations).

3.3.3 Calculating surface area of the oxidized mesh

In this section we estimate the surface area increase of a copper mesh due to the growth of copper oxide microneedles (**Figure 3.5)** from electro-oxidation process described in section 3.2.2. In this estimation we exclude the surface area contribution of the flake like micro-structures that adhere to the copper mesh surface due to their irregular and complex geometry **Figure 3.4 (b).** More SEM analysis of the surface micro-structure is provided in the supplementary section of this chapter.

We can calculate the lateral surface area (cylindrical part) and the base/top surface area, **Figure 3.5.**

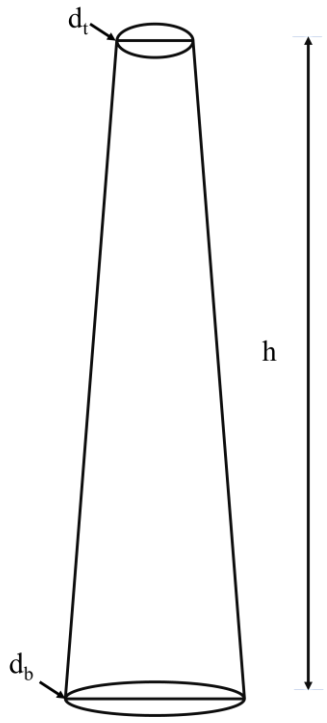

Figure 3.5 Copper oxide needles are estimated to have a conical cylindrical shape with base diameter d_b, heigh h and tip diameter d_t.

Calculating lateral surface area:

Lateral Surface Area (Cylindrical Part), LSA = 2π x radius x height=

$$LSA = 2\pi r_{cylinder} h \quad (3.3)$$

The average radius ($r_{cylinder}$) can be calculated by averaging the base and tip diameter).

$$r_{cylinder} = \frac{d_b + d_t}{4} \quad (3.4)$$

$r_{cylinder}$ = (0.5 + 0.18) / 4 = 0.17 μm.

Lateral Surface Area = 2 x π x 0.17 μm x 2 μm ≈ 2.69 μm².

Calculating base and top surface area:

Assuming the base and top of the needle are circles,

Base Surface radius: $r_b = d_b / 2 = 0.5 / 2 = 0.25$ μm

Base Surface Area, $BSA = 4\pi r_b^2$ (3.5)

BSA= 4 π (0.25 μm)^2 ≈ 0.7852 μm²

Tip Surface radius: $r_t = d_t / 2 = 0.18 / 2 = 0.09$ μm.

Tip Surface Area, $TSA = 4\pi r_t^2$ (3.6)

TSA= 4π (0.09 μm)^2 ≈ 0.102 μm².

Now, Surface Area of one needle, SA_{Total} = LSA + BSA + TSA = (2.69 + 0.102 + 0.7852) μm² ≈ 3.57 μm²

The approximate average surface area of each needle is 3.57μm^2. Surface Area of 20000 needles = 3.57 μm^2/needle × 20,000 needles = 714000 μm^2 ≈ 7.14 cm². The calculation presented above can be carried out simply by using the formula of the surface area of a conical frustum as well.

The total surface area of the oxidized mesh, surface area of a pristine mesh + surface area of copper oxide needles, (7.14+2.8) cm^2 = 9.94 cm^2 for a 1 cm x 1 cm sample. Our estimation suggests that the surface area increased on average (9.94-2.8/2.8) x 100%, or by 250% for the oxidized mesh. By growing microneedles on a copper mesh, we can significantly increase the total surface area of the mesh. If the surface area of the flake-like micro-structures is also considered, we anticipate a surface area enhancement that is greater than our estimate.

3.3.4 Maximum capillary pressure of the modified mesh

We measured the equilibrium height of the maximum capillary rise, h_{max} = 11.8 ± 0.2 cm. The method is described in the previous chapter. This gives us a maximum capillary pressure of the anodized copper mesh to be 1157 ± 10 Pa (~22% increase in maximum capillary pressure from a non-anodized mesh[18]).

3.3.5 Permeability of an electrooxidized mesh at varying capillary pressure

Following the method of measuring permeability described in chapter 2, section 2.2.3. we plot permeability vs. capillary pressure relationship in **Figure 3.6 (a)**. All the data measured is plotted. The data presented in **Figure 3.6** is fitted with the following equation using a least square method (orange curve):

$$\kappa\delta = a\, e^{-bx} + c \tag{3.7}$$

Where, a = 7.8 x 10^{-15} m^3, b = 2.4 x 10^{-3} Pa^{-1}, c = 4.8 x 10^{-16} m^3

In **Figure 3.6 (b)** we plot the permeability-thickness product vs. capillary pressure for the pristine copper mesh. and surface oxidized copper mesh in the same plot. From the plotted data we observe that the surface oxidized copper mesh has lower permeability compared to the pristine copper mesh.

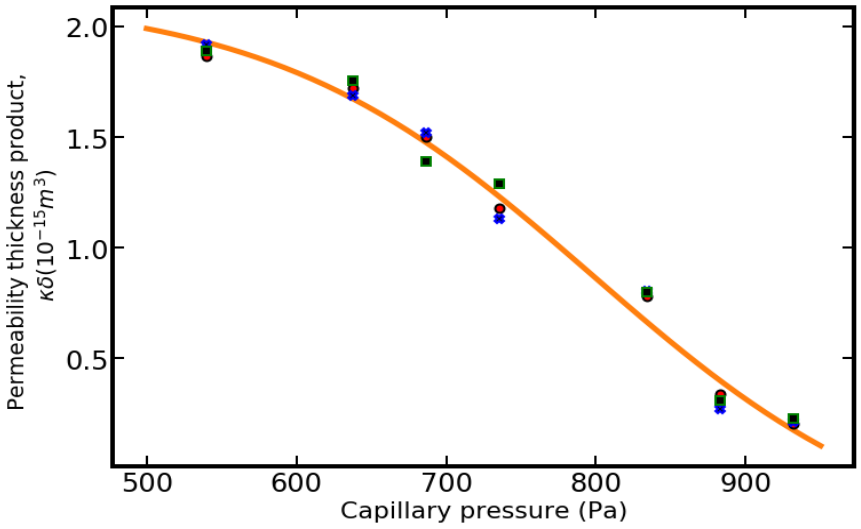

(a)

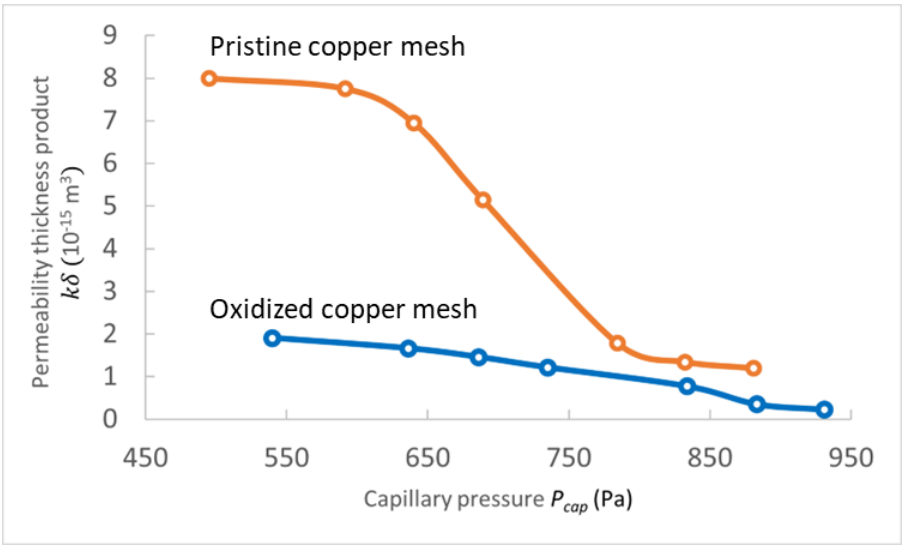

(b)

Figure 3.6 (a) Plot of data collected from the permeability measurements of pristine copper mesh at varying capillary pressures. **(b)** Data of permeability at varying capillary pressures for pristine and surface oxidized copper mesh are plotted together. The orange curve and blue curve plot data of oxidized copper mesh. Oxidized meshes exhibit lower permeability compared to pristine copper mesh.

Integrating Darcy's law (equation 2.1), we find, $u\delta\mu l = \int_o^P \kappa\delta(p_g - p)dp$

$$u\delta\mu l = cx - a\frac{e^{-bx}}{b} + p_0 \qquad (3.8)$$

With p_0 = 3.522 x 10^{-12} Pa.m^3. For different pressure differences, $x = \Delta P$ we can plot Equation 3.8 in **Figure 3.7.**

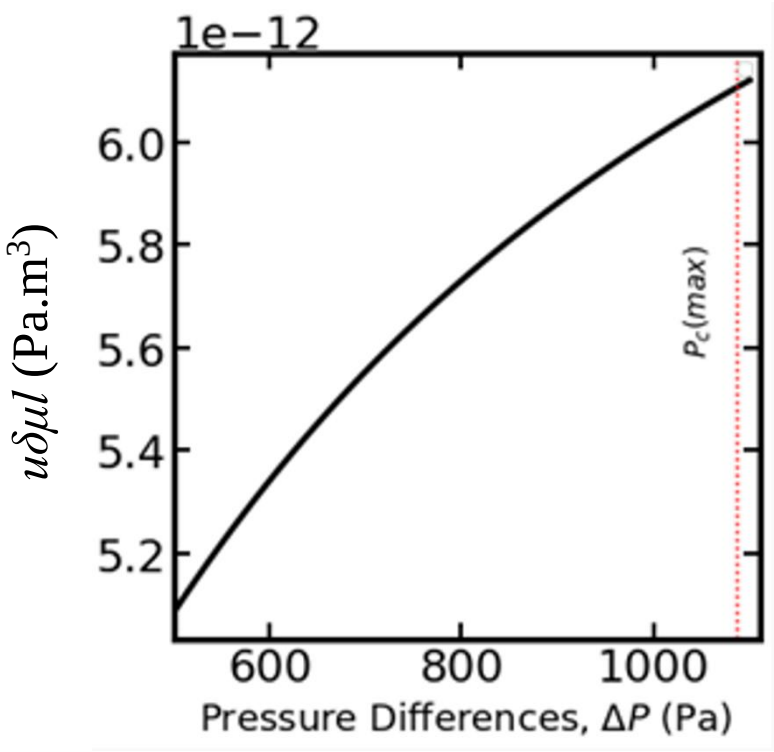

Figure 3.7 $u\delta\mu l$ vs. pressure differences of a copper mesh with oxide needles. The red dotted line is the maximum capillary pressure.

We find that the normalized superficial velocity ($u\delta\mu l$) increases with increasing pressure difference until the maximum capillary pressure of the oxidized mesh.

3.3.6 Parametric studies for water as the working fluid

Equation 3.8 can be applied to understand the performance of mesh in specific cases. We can consider the maximum flowrate that can be achieved for DI water in copper #100 mesh with plain weave and wire diameter 0.114 mm assuming a driving pressure equal to the maximum capillary pressure. **Figure 3.8 (a)** shows $u\delta$ in the mesh at wicking lengths of l = 0.25 cm, l = 0.50 cm, l = 0.75 cm, and l = 1 cm versus total pressure drop for DI water (dynamic viscosity at boiling point of water, μ = 0.282 mPa s), demonstrating higher $u\delta$ through shorter wicking distance with increasing pressure differences. **Figure 3.8 (b)** shows the values of superficial velocity through a single layer free standing mesh wick, $u\delta$, at maximum driving pressure for different dynamic viscosities, 0.282 mPa s, 0.354 mPa s, 0.466 mPa s, 0.6527 mPa s, and 0.95 mPa s, respectively. For a fixed capillary pressure, $u\delta$ decreases with increasing wicking length asymptotically approaching zero at rates determined by the liquid viscosity.

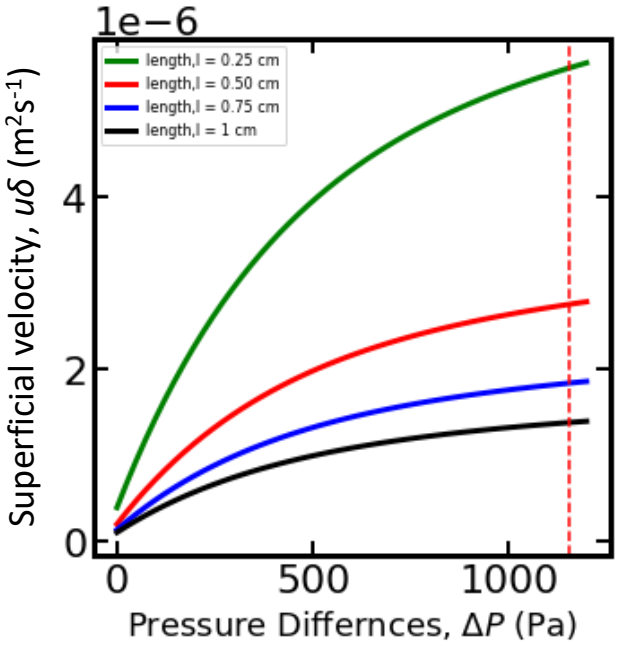

(a)

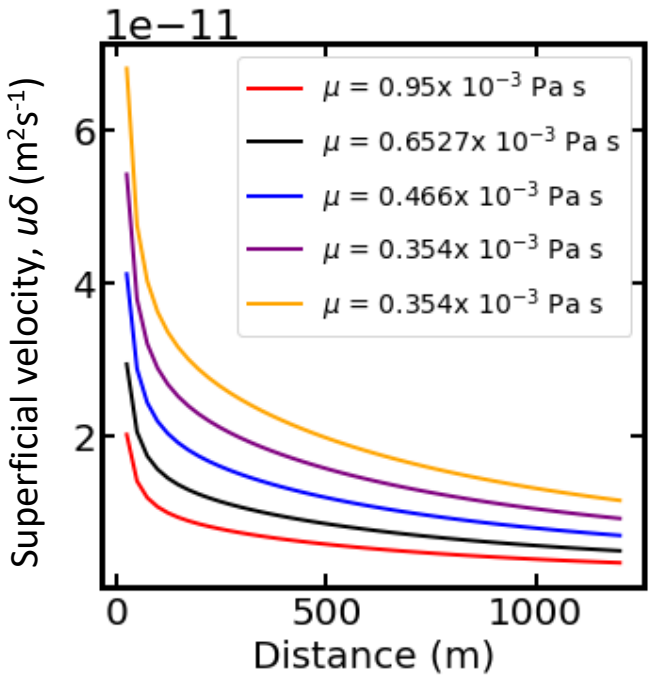

(b)

Figure 3.8 Parametric studies of water flow behavior of water on a copper mesh with CuO microneedles. **(a)** $u\delta$ ($m^2\ s^{-1}$) versus pressure difference, ΔP (Pa), at different wicking lengths. The red-dotted straight line indicates the maximum capillary pressure, *Pc (max)*. **(b)** Superficial velocity through a single layer free standing mesh wick, $u\delta$ ($m^2\ s^{-1}$), decreases with increasing wicking distance at maximum capillary pressure. Longer wicking lengths experience more considerable viscous drag compared to shorter wicking lengths. $u\delta$ of DI water is thus lower for longer wicking lengths than that of shorter wicking lengths.

3.3.7 Parametric studies for HFO1233zd and HFE7100 as the working fluid

We conduct parametric studies for two common heat transfer fluids HFO1233zd (at 25 °C surface tension, σ = 12.57 mN m^{-1} and dynamic viscosity, μ = 0.469 mPa s, $\theta \approx 0^0$) and HFE7100 (at 25 °C surface tension, σ = 13.345 mN m^{-1} and dynamic viscosity, μ = 0.58 mPa s, $\theta \approx 0°$), in plain weaved single layer

copper #100 mesh with 0.114 mm wire diameter to understand their flow properties in a surface oxidized copper mesh.

The behavior of $u\delta$ for HFO1233zd and HFE7100 in #100 mesh at wicking lengths of l = 0.25 cm is plotted in **Figure 3.9 (a)**. $u\delta$ increases with driving pressure differences (There is a marginally higher $P_{c(max)}$ for HFO1233zd than HFE7100).

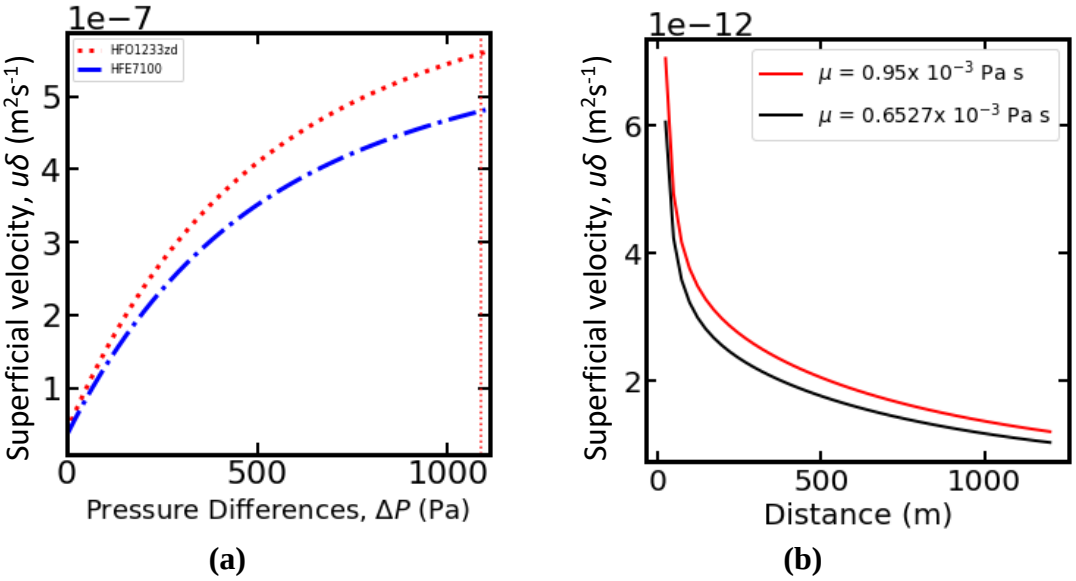

(a) **(b)**

Figure 3.9 (a) $u\delta$ (m^2 s^{-1}) versus pressure difference, ΔP (Pa), at wicking length of l = 0.25 cm for HFO1233zd and HFE7100, respectively. The red-dotted straight line indicates the maximum capillary pressure, *Pc* (max) of HFO1233zd. The blue-dotted straight line indicates the maximum capillary pressure, *Pc* (max) of HFE7100. **(b)** $u\delta$ (m^2 s^{-1}) with increasing wicking distance at maximum capillary pressure for common fluids used in electronics cooling application (HFO1233zd and HFE7100, respectively).

In **Figure 3.9 (b)** we show the values of $u\delta$, at maximum driving pressure for dynamic viscosities of 0.469 mPa s (HFO1233zd) and 0.581 mPa s (HFE7100). Due to the lower surface tension of these fluids than DI water at similar temperature, the maximum driving force (pressure difference) we can apply is significantly lower than that of DI water.

3.4 Analysis and further investigations

In this chapter we have delved into enhancing fluid flow properties in a copper mesh via electro-oxidation method by growing copper oxide microneedles. At different capillary pressures, we find that copper meshes with developed oxide needles have lower permeability than a naked mesh. We anticipated that the surface treatment of copper mesh with microneedles would improve its wettability and improve the flow parameters of permeability and capillary pressure. We will address the ramifications of the few factors we have identified to help explain our experimental results. In addition, we will outline a few approaches to investigate these causes:

3.4.1 Chemical heterogeneity of copper oxides

We hypothesize that heterogeneity of the microstructures and chemical compositions of copper oxides (Cu_2O, CuO, $Cu(OH)_2$) **figure 3.10** give rise to a non-uniform wetting of the surface treated copper mesh**.** These oxides have different surface energies; the interaction energies with water and the resulting wettability vary heterogeneously along the surface of the mesh structure.

3.4.2 Geometrical heterogeneity of copper oxides

The copper oxides are geometrically heterogeneous; just at the surface of the oxidized mesh, cuprous oxide (Cu_2O), which resembles flake-like crystals, first develops, then cupric oxide (CuO), **Figure 3.10** which resembles needle-like microstructures, grows. The localized contact angle of a liquid and spreading-imbibition behavior can both be affected by microstructural heterogeneity, relative proportions, and heterogeneity. In hierarchical porous materials, the liquid frequently exhibits *'hemi-wicking'* behavior, where the microstructures first help in spreading the liquid and generating a thin film attached next to the surface of porous materials, and then the incoming fluids later imbibe into the porous material with an existing liquid film. It has been demonstrated that in such a situation, a hierarchical porous material meets *Wenzel's* requirement and

is entirely wet if the substrate and microstructure are likewise completely wet. However, the presence of hydrophobic substances from adsorption in the surrounding environment and the presence of tiny air bubbles can impair the wettability. [19]

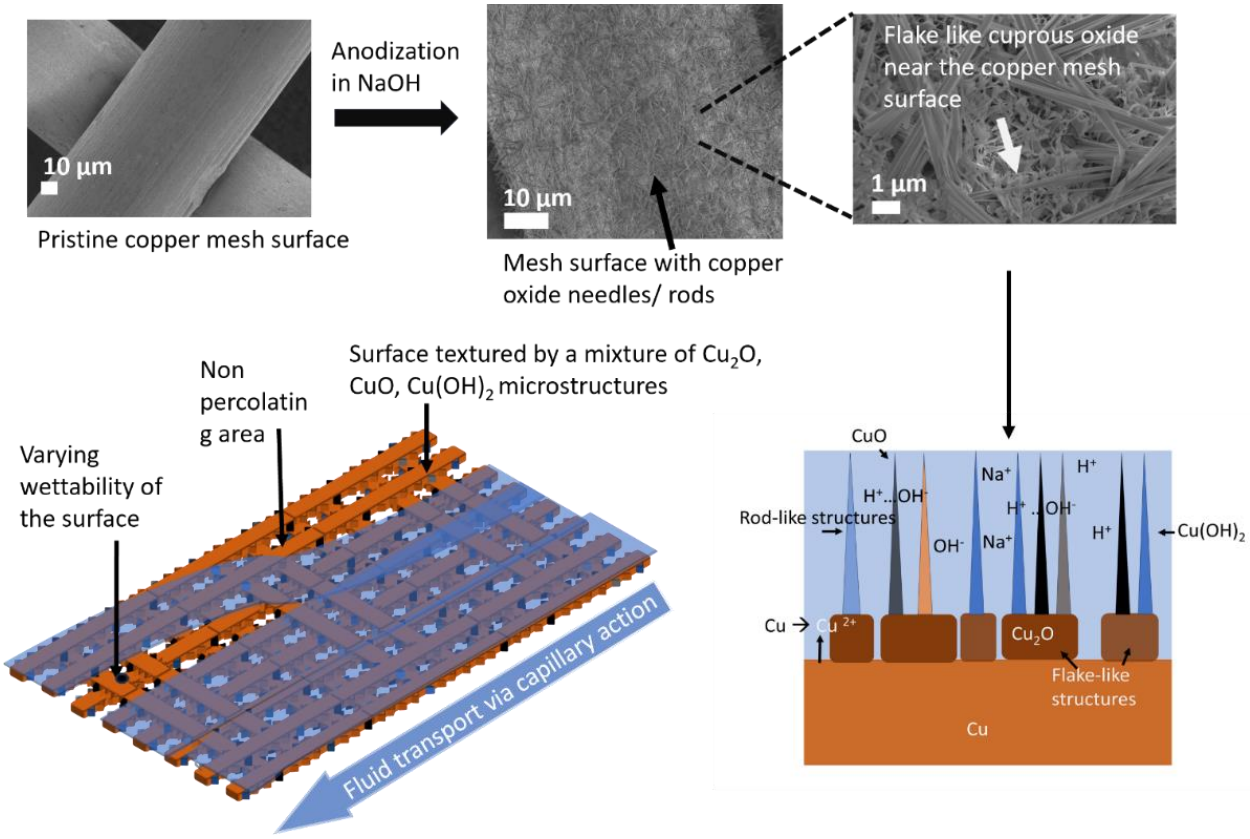

Figure 3.10 A surface with variable wettability is created via the anodizing of copper mesh, the permeability in the in-plane direction is influenced by the differences in wettability in different regions.

3.4.3 Constriction of the liquid at intersection of the wires

A wire mesh has complex geometry; for a plain weave a wire goes over another wire making narrow intersections. The capillary pressure at the intersections is higher than the mesh openings due to the smaller dimensions of the mesh which would in turn tend to pull the liquid towards. For a liquid flowing through the mesh, these intersections of higher capillary pressures would then reduce the saturation of the liquid in the pores. For an oxidized mesh with microneedles, such an effect can be enhanced by the existence of smaller microstructures within the wire intersections. **Figure 3.11**

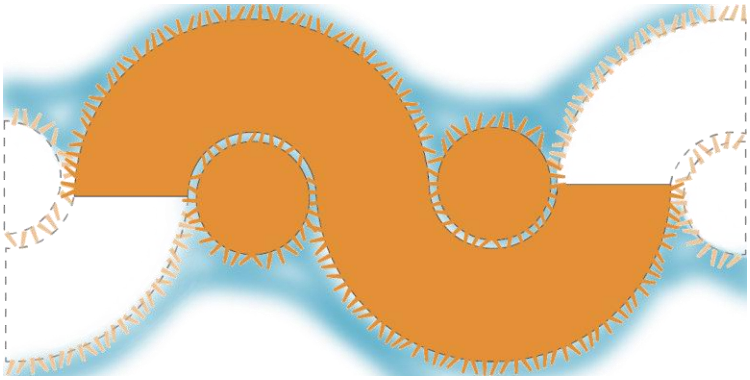

Figure 3.11 A cartoon of the cross-section of a mesh like structure with random oxide microneedles grown via electrooxidation technique. The intersection of the wire creates smaller regions of higher capillary pressure, constricting the fluid in these regions; the oxide microneedles enhance this effect.

3.4.4 Determination of the shape of the liquid meniscus in oxidized mesh

The shape of the liquid meniscus in wire mesh openings contains the information of the true capillary pressure in a complex wire mesh type structure with microneedles. This shape, although complex, can be determined either by using (a) Numerical approach or by (b) experimental methods:

(a) Numerical approach:

Utilizing thermodynamic modeling software such as SurfaceEvolver, a potent tool for describing equilibrium meniscus shapes. This software can be employed to predict the equilibrium shape of a meniscus within an oxide microstructure-grown copper mesh. A significant challenge is accurately defining the geometry of a complex woven structure with oxide needles on top, which is required as input for the software to perform calculations. Implementing image analysis and developing code to describe the vertices, edges, and faces of the mesh can be instrumental in overcoming this challenge.

(b) Experimental methods:

Here we outline experimental methods that can be applied individually or in a combination to verify our findings:

I. Liquid Metal Penetration: Experimentally determine the meniscus shape using a different working fluid, such as liquid metals. Liquid metals can infiltrate the porous structure at higher temperatures while in a liquid state and subsequently freeze to form the shape of the meniscus. Subsequent analysis involving precise cross-sectioning, polishing, electron microscopy, and image analysis will yield valuable insights into the actual shape of the meniscus. Moreover, dimensional analysis can be employed to predict the meniscus shape for other working fluids exhibiting similar wetting characteristics.

II. Fluorescent Dye Imaging: Utilizing fluorescent dyes is a powerful method to directly image the meniscus. Researchers often employ this technique to study various aspects of fluid dynamics and interface behavior. Once a suitable fluorescent dye is chosen, it can be dissolved in water and would minimally alter its surface energy. Common dyes used include Rhodamine B, Fluorescein, or various quantum dots. A light source with the appropriate wavelength is directed onto the meniscus region, exciting the fluorescent dye molecules. A camera or imaging system captures the emitted fluorescence, creating a visual representation of the meniscus. The intensity and distribution of fluorescence can reveal information about the meniscus's shape, stability, and interactions with other substances.

III. Interference Techniques: Interference-based methods are another valuable approach for imaging the meniscus with water. Interference arises when two or more waves overlap, resulting in variations in light intensity. A common setup involves the use of a light source, typically a laser, directed onto the meniscus at a specific angle. As the laser light hits the meniscus, it undergoes both reflection and refraction due to the change in the refractive index at the interface between air and water. The reflected and refracted light waves interfere with each other, creating an interference pattern that can be observed and recorded. The interference pattern is highly sensitive to changes in the meniscus shape. By analyzing the interference pattern, we can deduce information about the curvature, thickness of the meniscus, and surface tension of the liquid.

3.5 Conclusions

In this work, we have surface treated copper mesh via electro-oxidation method in a NaOH solution to grow copper oxide micro-needles. The oxidized mesh exhibits higher maximum capillary pressure than a pristine copper mesh. Furthermore, we have characterized permeability of the treated copper mesh at varying capillary pressures. The experimental data were fit with an exponential decay curve using the least square fit method. The integration of Darcy's law gives us a master curve for superficial velocity of transporting liquid via capillary action inside the treated mesh. We also conduct parametric calculations of flow behavior for different wicking lengths and varying viscosity of liquid. We observed that permeability of the treated mesh is lower than the pristine mesh at lower capillary pressures. We proposed models to analyze this behavior, chemical heterogeneity and constriction of fluid in wire intersections may contribute to the lower permeability of the oxidized mesh case. This work provides some key insights in capillary driven flow in surface treated mesh like structures.

3.6 References:

[1] E. P. K. Currie, W. Norde, and M. A. Cohen Stuart, “Tethered polymer chains: surface chemistry and their impact on colloidal and surface properties,” 2003.

[2] H. J. Cho, D. J. Preston, Y. Zhu, and E. N. Wang, “Nanoengineered materials for liquid-vapour phase-change heat transfer,” Nature Reviews Materials, vol. 2, no. 2. Nature Publishing Group, Dec. 06, 2016. doi: 10.1038/natrevmats.2016.92.

[3] N. Vigneswaran, F. Samsuri, B. Ranganathan, and P. Padmapriya, “Recent advances in nano patterning and nano imprint lithography for biological applications,” in Procedia Engineering, Elsevier Ltd, 2014, pp. 1387–1398. doi: 10.1016/j.proeng.2014.12.420.

[4] J. Aizenberg, P. V. Braun, and P. Wiltzius, “Patterned colloidal deposition controlled by electrostatic and capillary forces,” Phys Rev Lett, vol. 84, no. 13, Mar. 2000, doi: 10.1103/PhysRevLett.84.2997.

[5] W. J. Stepniowski and W. Z. Misiolek, “Review of Fabrication Methods , Physical Properties , and Applications of Nanostructured Copper Oxides Formed via Electrochemical Oxidation,” pp. 1–19, 2018, doi: 10.3390/nano8060379.

[6] D. Giziński, A. Brudzisz, J. S. Santos, F. Trivinho-Strixino, W. J. Stępniowski, and T. Czujko, “Nanostructured anodic copper oxides as catalysts in electrochemical and photoelectrochemical reactions,” Catalysts, vol. 10, no. 11, pp. 1–38, 2020, doi: 10.3390/catal10111338.

[7] C. Gattinoni and A. Michaelides, “Atomistic details of oxide surfaces and surface oxidation: the example of copper and its oxides,” Surf Sci Rep,

vol. 70, no. 3, pp. 424–447, 2015, doi: 10.1016/j.surfrep.2015.07.001.

[8] F. Soroush, T. E. Liu Qianying Wu Chi Zhang Mehdi Asheghi Kenneth Goodson, and L. Marco Egger Christian Rittner Martin, “A HYBRID MICROPOROUS COPPER STRUCTURE FOR HIGH PEROFMRANCE CAPILLARY-DRIVEN LIQUID FILM BOILING” 2021. [Online]. Available: http://asmedigitalcollection.asme.org/InterPACK/proceedings-pdf/InterPACK2021/85505/V001T05A001/6802665/v001t05a001-ipack2021-73309.pdf

[9] R. Sondors et al., “Size distribution, mechanical and electrical properties of cuo nanowires grown by modified thermal oxidation methods,” Nanomaterials, vol. 10, no. 6, 2020, doi: 10.3390/nano10061051.

[10] F. Soroush et al., “Contact angle tuning of copper microporous structures,” Proceedings of ASME 2021 International Technical Conference and Exhibition on Packaging and Integration of Electronic and Photonic Microsystems, InterPACK 2021, pp. 1–7, 2021, doi: 10.1115/ipack2021-73334.

[11] M. J. Siegfried and K. S. Choi, “Directing the architecture of cuprous oxide crystals during electrochemical growth,” Angewandte Chemie - International Edition, vol. 44, no. 21, pp. 3218–3223, 2005, doi: 10.1002/anie.200463018.

[12] F. M. Chang, S. L. Cheng, S. J. Hong, Y. J. Sheng, and H. K. Tsao, “Superhydrophilicity to superhydrophobicity transition of CuO nanowire films,” Appl Phys Lett, vol. 96, no. 11, 2010, doi: 10.1063/1.3360847.

[13] W. Jiang, J. He, F. Xiao, S. Yuan, H. Lu, and B. Liang, “Preparation and Antiscaling Application of Superhydrophobic Anodized CuO Nanowire Surfaces,” Ind Eng Chem Res, vol. 54, no. 27, pp. 6874–6883, 2015, doi: 10.1021/acs.iecr.5b00444.

[14] Y. Cudennec and A. Lecerf, “The transformation of Cu(OH)2 into CuO, revisited,” Solid State Sci, vol. 5, no. 11–12, pp. 1471–1474, 2003, doi: 10.1016/j.solidstatesciences.2003.09.009.

[15] Q. N. Pham, B. Shao, Y. Kim, and Y. Won, “Hierarchical and Well-Ordered Porous Copper for Liquid Transport Properties Control,” ACS Appl Mater Interfaces, vol. 10, no. 18, pp. 16015–16023, 2018, doi: 10.1021/acsami.8b02665.

[16] C. H. Xu, C. H. Woo, and S. Q. Shi, “The effects of oxidative environments on the synthesis of CuO nanowires on Cu substrates,” Superlattices Microstruct, vol. 36, no. 1–3, pp. 31–38, 2004, doi: 10.1016/j.spmi.2004.08.021.

[17] R. Zhou, S. Lin, F. Shen, S. Y. Khew, and M. Hong, “A universal copper mesh with on-demand wettability fabricated by pulsed laser ablation for oil/water separation,” Surf Coat Technol, vol. 348, no. April, pp. 73–80, 2018, doi: 10.1016/j.surfcoat.2018.05.035.

[18] M. R. Shattique et al., “Permeability of Single-Layer-Free-Standing Meshes at Varying Capillary Pressure via a Novel Method,” Adv Mater Interfaces, 2023, doi: 10.1002/admi.202300326.

[19] J. Bico, U. Thiele, and D. Quéré, “Wetting of textured surfaces,” Colloids and Surfaces A: Physicochemical and Engineering Aspects, ISSN: 0927-7757, Vol: 206, Issue: 1, Page: 41-46, 2002. https://doi.org/10.1016/S0927-7757(02)00061-4

[20] Mehrabi, H., Conlin, S.K., Hollis, T.I., Gattis, B.S., Nelson Weker, J. and Coridan, R.H. (2023), Electrochemical Control of the Morphology and Functional Properties of Hierarchically Structured, Dendritic Cu Surfaces. Energy Technol., 11: 2201124. https://doi.org/10.1002/ente.202201124

Supplementary materials

In this supplementary section, we provide SEM images of the pristine copper mesh and electro-oxidized copper mesh with oxide microstructures:

3.6.1 Pristine copper mesh

SEM of the pristine copper mesh surface at varying magnification is presented below:

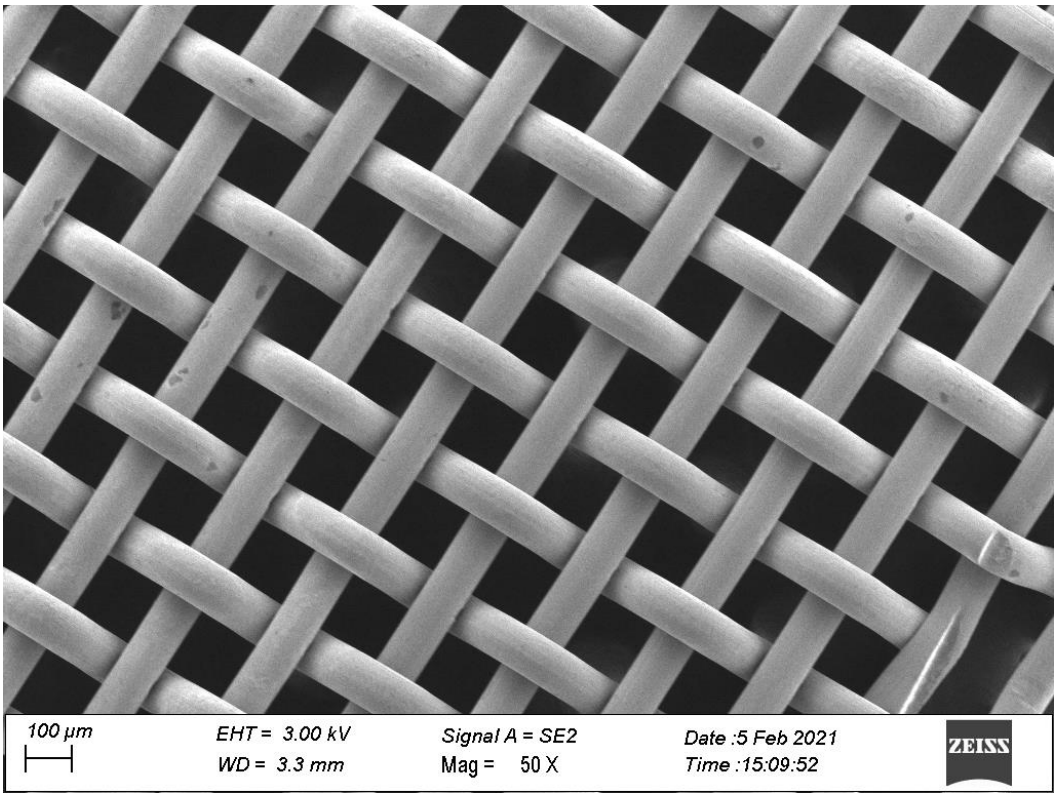

(a)

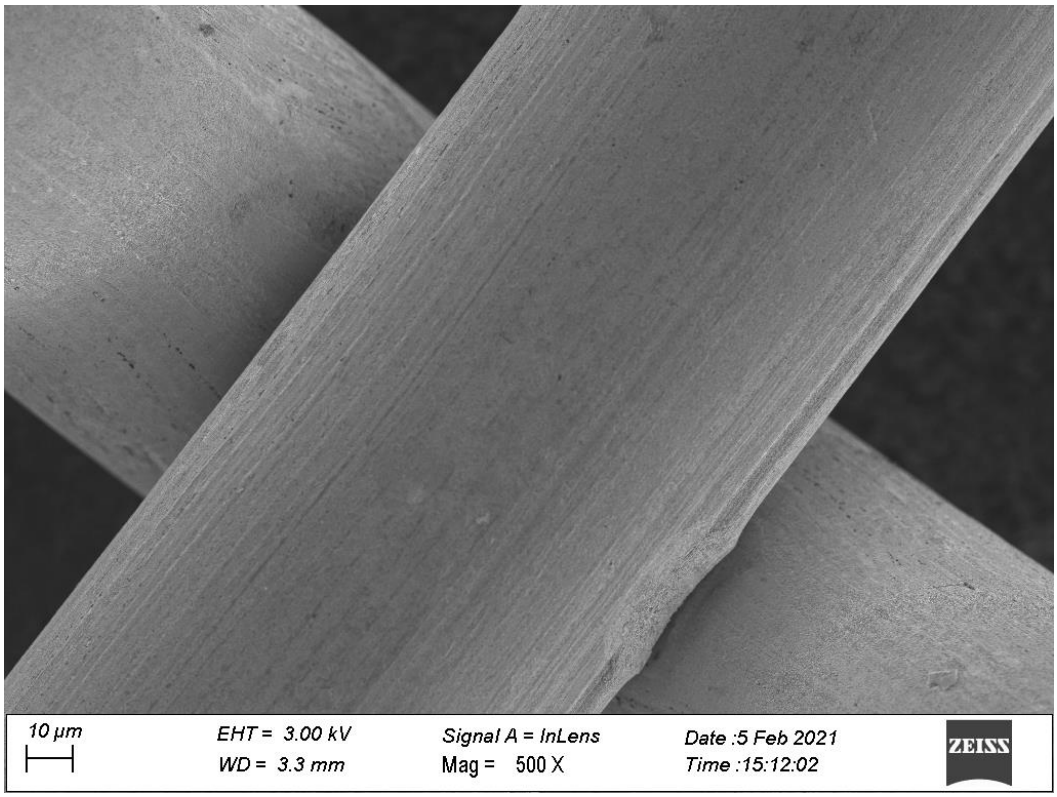

(b)

Figure 3.12 3SM1(a-b) SEM of pristine copper mesh surface

3.6.2 Oxidized copper mesh surface

In this section, we provide SEM images of electro-oxidized SEM surface at varying magnifications:

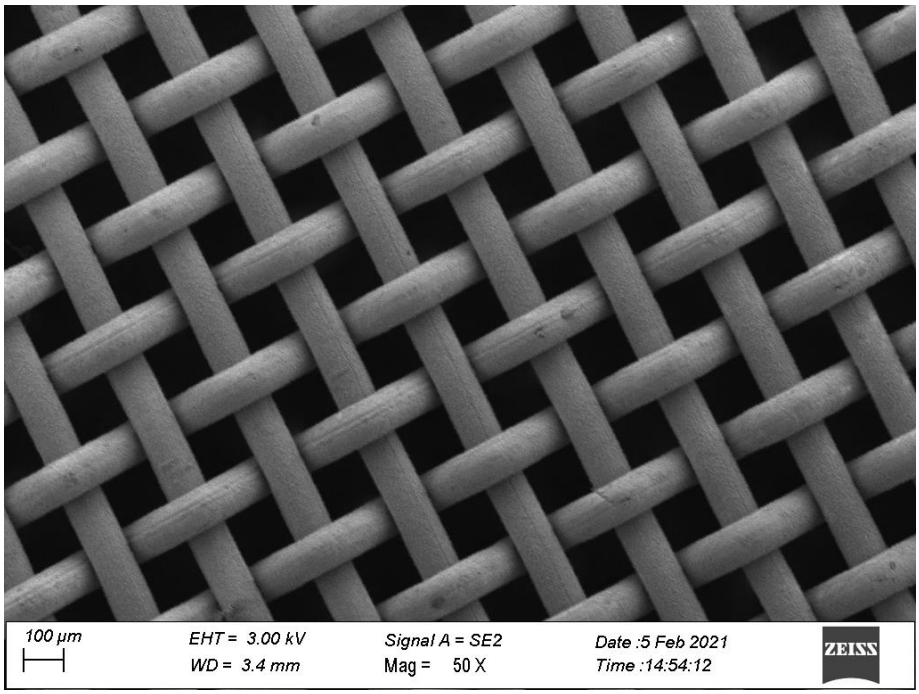
100 µm
EHT = 3.00 kV
WD = 3.4 mm
Signal A = SE2
Mag = 50 X
Date :5 Feb 2021
Time :14:54:12
ZEISS

(a)

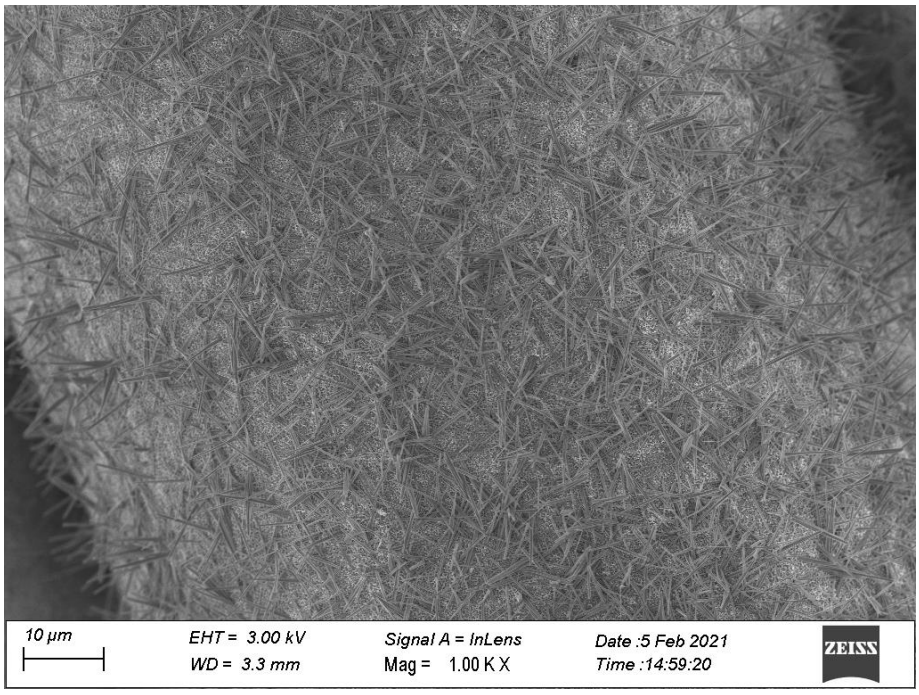
10 µm
EHT = 3.00 kV
WD = 3.3 mm
Signal A = InLens
Mag = 1.00 K X
Date :5 Feb 2021
Time :14:59:20
ZEISS

(b)

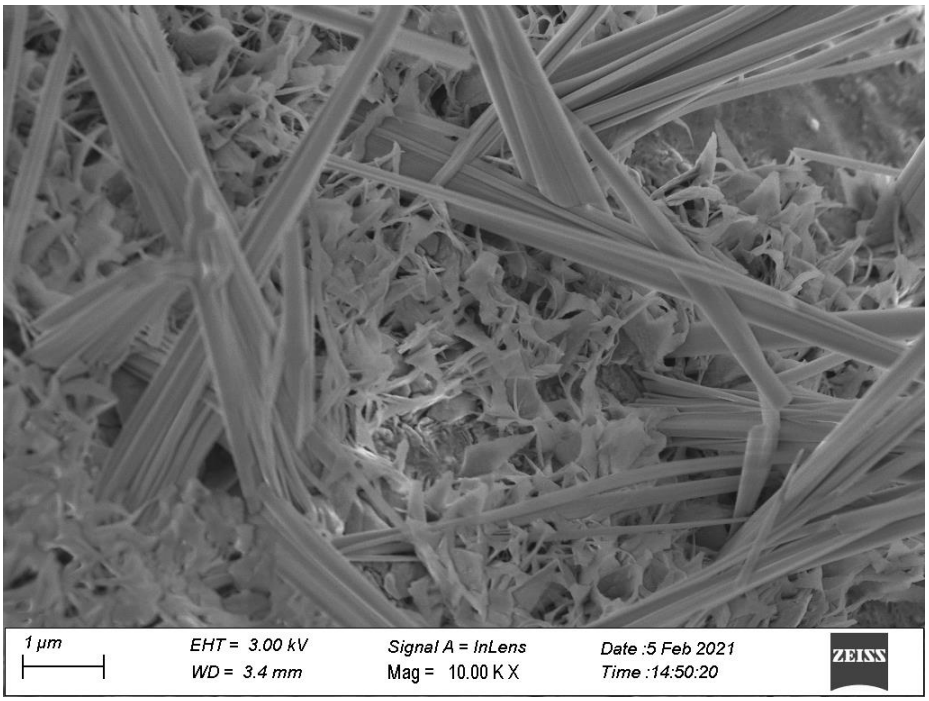

(c)

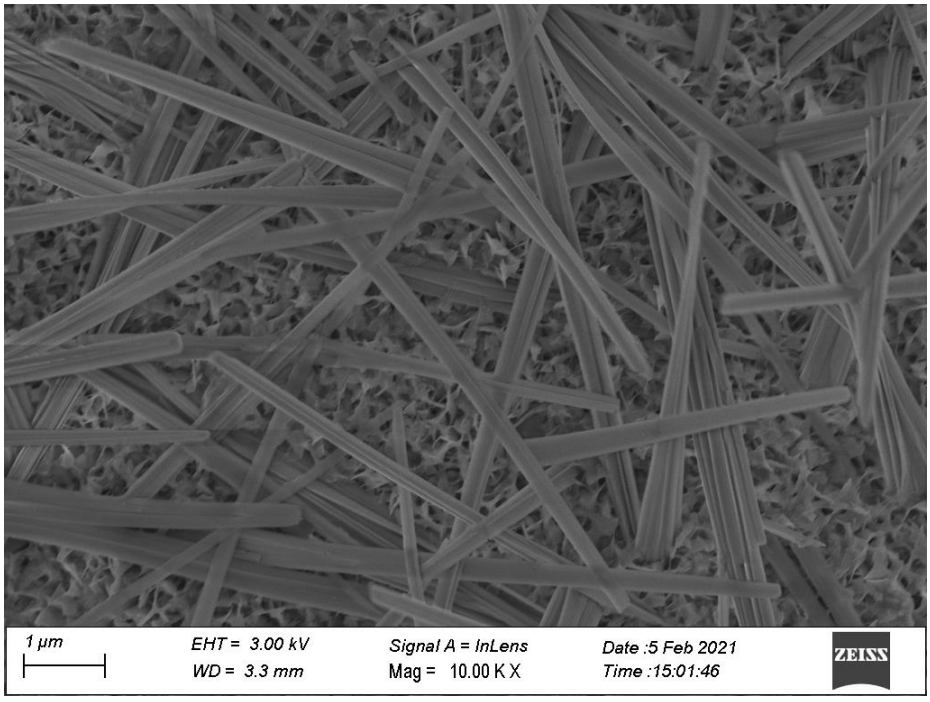

(d)

Figure 3.13 3SM2 (a-d) SEM of electro-oxidized copper mesh surface at varying magnification.

3.6.3 Surface of the counter electrode

In this section we provide the SEM image of the surface of the counter electrode mesh during electrooxidation:

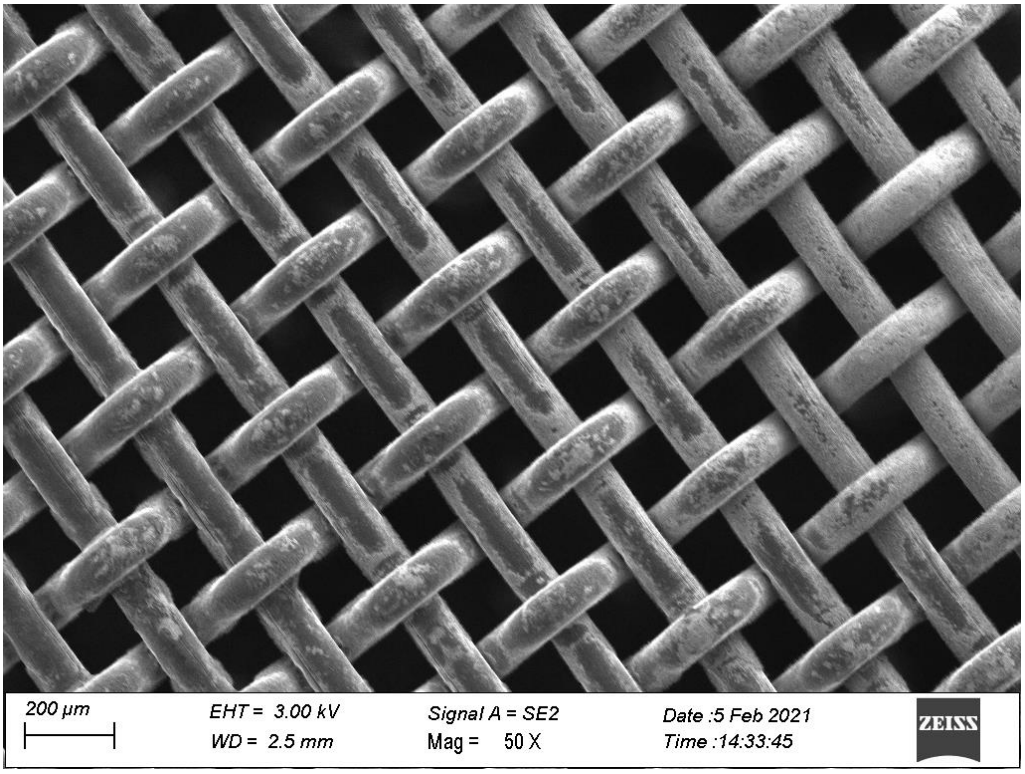

(a)

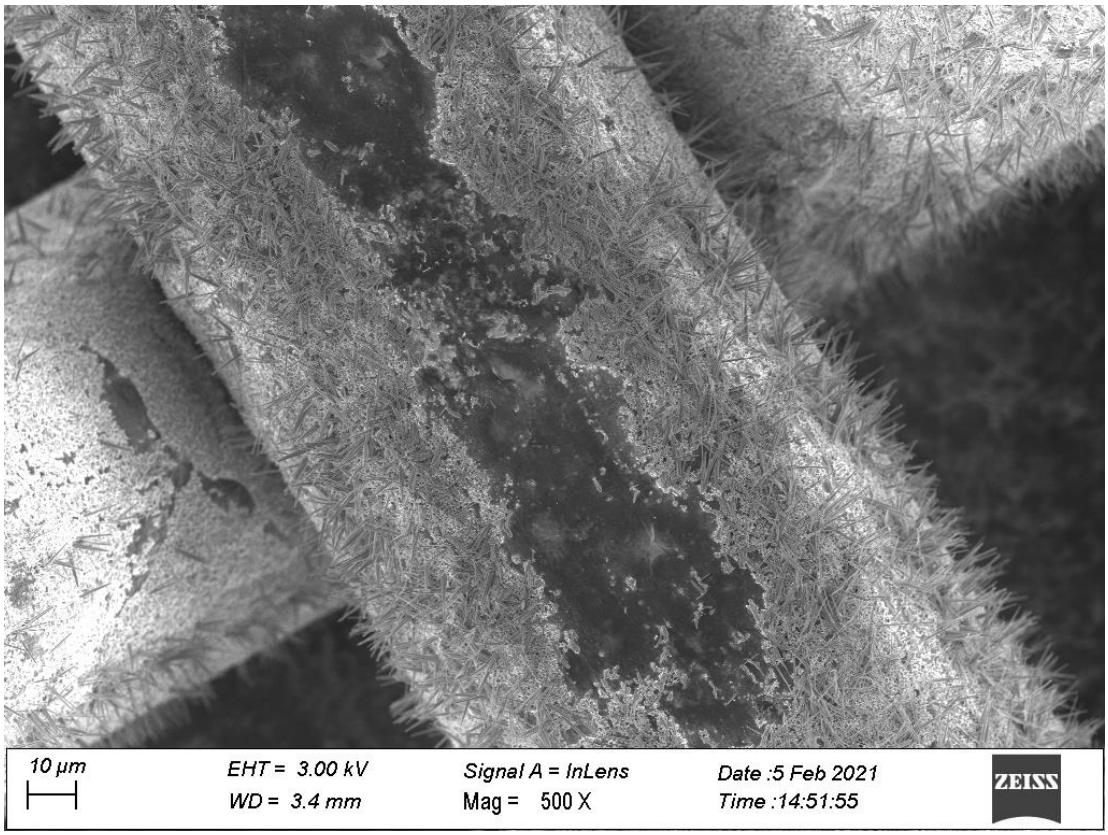

(b)

Figure 3.14 3SM2 (a-b) SEM of copper mesh counter electrode after electrooxidation step at varying magnification.

Chapter 4

Design and synthesis of a three-dimensional manifold to enhance two-phase heat transfer

4.1 Introduction

Currently, power electronics account for 30% of all electricity used, a percentage that is predicted to increase three times over the next fifteen years. Power transistors used in electric vehicles, renewable energy converters, and 3D-integrated microelectronics are a few examples. The use of wide band-gap (WBG) semiconductors in vehicle power electronics may also increase fuel efficiency for the following generation of electric vehicles by up to 10%.[1]-[5] Due to the improved performance of electronic devices, there has been a growth in demand for efficient heat management in electronic cooling systems recently two-phase liquid/vapor cooling stands out among different cooling systems for its exceptional heat transfer capabilities and effectiveness in heat dissipation.[4]

The efficacy of boiling heat transfer has been enhanced by changing planar surfaces with microstructures and roughness to promote wettability. This improvement expands the region where heat transfer can occur, makes it easier to convert thermal energy into latent vaporization heat, and controls the dynamics of vapor bubbles. Porous heat spreaders can be integrated into designs of effective devices that use boiling heat transfer. Importantly, since the liquid and vapor phases coexist in these devices, and their interaction affects performance, it is crucial to regulate them.

The design and synthesis of a three-dimensional manifold that can efficiently control the simultaneous transport of liquid and vapor are covered in this chapter.

4.2 Designing an efficient two-phase cooling device

The transport of heat transfer liquid to the porous heat spreader is limited by the viscous pressure drop of the liquid **figure 4.1(a).** Shorter liquid transport distances are required to maintain adequate pressure for the fluid to flow to the heated surface. Shorter transport distances can be enabled by supplying liquid uniformly to the porous evaporator, **Figure 4.1(b).** At higher heat-fluxes, the vapor from the liquid covers the heated surface hindering the liquid flow.

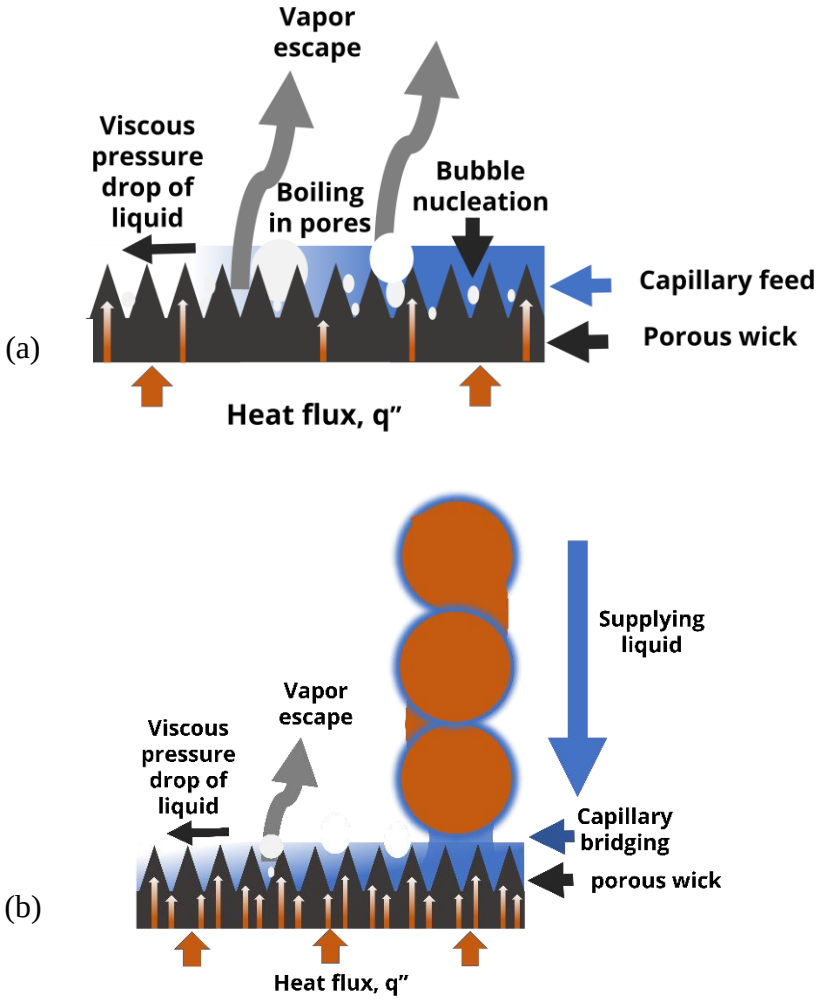

Figure 4.1 (a) Liquid pressure drop due to viscous loss of the liquid depletes the porous wick of heat transfer liquid. Furthermore, nucleation and growth of vapor bubbles during boiling competes with the liquid path. Both can be a

limiting factor for critical heat flux (CHF). (b) Supplying liquid to the porous evaporator can elevate liquid pressure in the wick. The figure is not to scale.

Now we will discuss our design of an efficient two-phase heat transfer device for fluid management with the aim of increasing CHF. **Figure 4.2** shows the design of a two-phase cooling system that reduces the liquid pressure drop and effectively handles the competition between liquid delivery and vapor escape. Multiple parallel liquid lines (i) transport liquid uniformly to a porous evaporator (ii), which is created directly on the substrate material using simple in-situ techniques. Additionally, the vacant gaps between the parallel liquid channels (iii) provide pathways for the vapor escape, minimizing competition between liquid and vapor flow and boosting process efficiency.

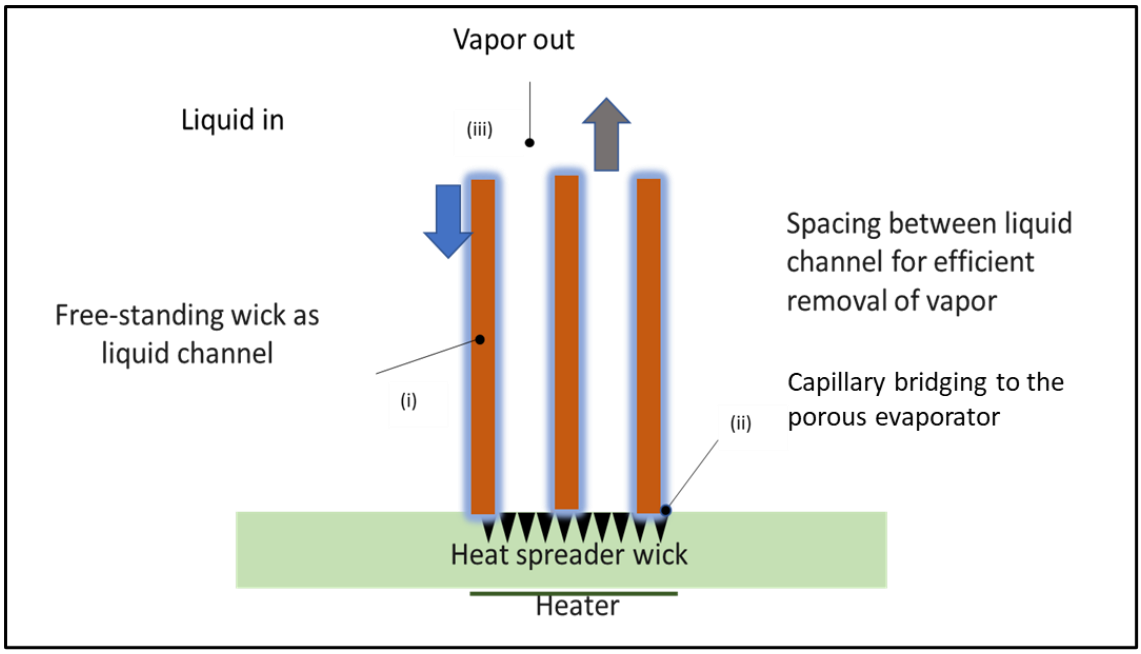

Figure 4.2 Designing an efficient two-phase cooling system. Uniform liquid delivery aided by parallel equally spaced liquid delivery paths to a porous evaporator crafted on a substrate material and paths for vapor escape in between the liquid channels increase the efficiency of the system.

4.2.1 Design and synthesis of liquid channels

The liquid channel serves the function of containing and conveying liquid to the porous evaporator region within a thermal system. In this context, the liquid channel facilitates the heat transfer process by ensuring the controlled delivery of the working fluid to the evaporator.

To optimize the performance of the thermal system, the design of the liquid channel adheres to certain key considerations. Firstly, the liquid channel is designed to minimize its physical thickness or cross-sectional dimension. The crucial objective of maintaining a thin liquid channel is to create sufficient available space within the channel for the vapor phase of the working fluid to escape. During the evaporation process within the porous evaporator, the liquid undergoes phase change, transitioning from liquid to vapor. This phase change necessitates the displacement of the liquid as it transforms into vapor. To ensure an unobstructed and efficient escape path for the vapor, the liquid channel's thickness must be optimized to allow for the volumetric expansion associated with the phase change. A thin liquid channel ensures that the vapor can be accommodated without encountering undue resistance or restrictions, thereby enabling a smooth and effective phase transition within the evaporator.

However, the channel must also mitigate viscous pressure losses along the liquid flow path. Viscous pressure loss arises due to the frictional resistance encountered by the flowing liquid as it traverses the channel. Pressure loss is minimized by maximizing the cross-sectional area for flow. A balance must be established between impeding vapor and liquid flow. Furthermore, the channel must be able to retain liquid within it at adequate capillary pressure (equal to the difference between the liquid and vapor pressures).

4.2.1.1 Different approaches of designing liquid channels

In our liquid channel design, we implement two distinct design approaches: a micro channel and a porous wick based on copper materials. Clean surfaces of copper materials are hydrophilic, and copper is a readily available material. We design the liquid channel with copper-based material.

A micro channel is made of two separated solid walls with fluid flow passage generally on the scale of 50 μm to 500 μm in between the walls. A pumping mechanism drives fluid flow within the microchannels. **Figure 4.3(a)**

In our design, liquid microchannel consist of two solids walls of 25 μm thickness, made of copper sheets separated by a thin middle layer designed to control the direction of the liquid, the thickness of this middle layer is 50 μm. The liquid channels are physically separated for the vapor escape. **Figure 4.4**

A liquid channel can be made of a porous wick as well. Small pores inside a wick exhibit capillarity when in contact with a fluid. For a liquid channel the liquid is held and transported using the capillarity of the porous wick. Copper based porous materials like copper foam or copper mesh can be used as a liquid channel **Figure 4.3(b)**

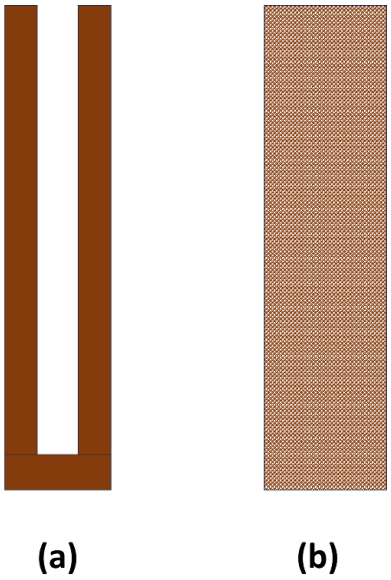

Figure 4.3 Schematic of liquid channel in a manifold: **(a)** a microchannel or **(b)** a porous wick can be used as a liquid channel in a manifold design.

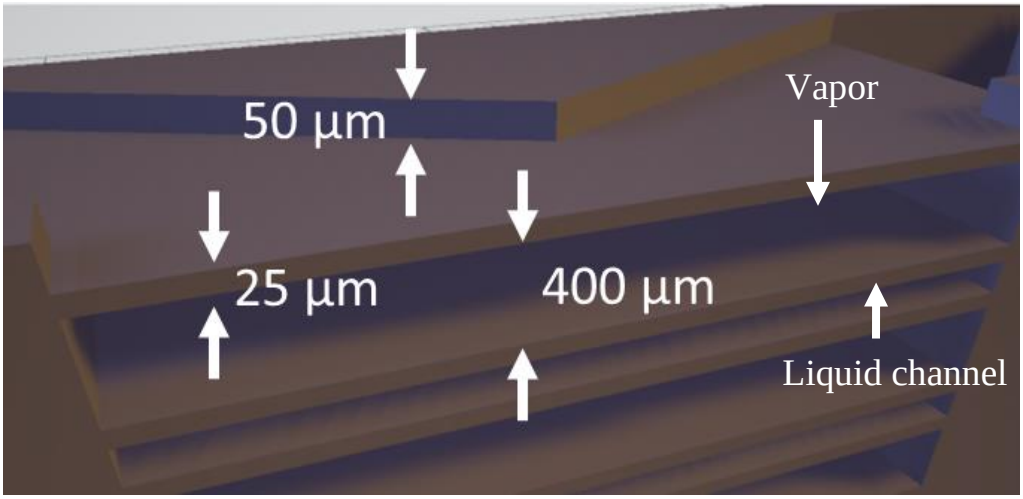

Figure 4.4 Design of the liquid microchannel made of thin copper sheets. The microchannels are stacked on top of each other and are kept apart by using separator layers.

4.2.1.2 Approaches of processing liquid channel

The geometrical requirements of the microchannels provide some challenges to process them using copper base materials. In the following sections we will describe a few different approaches that can be taken to process liquid channels based on copper materials**:**

(i) Layer-by-layer additive manufacturing of the liquid channel

The manifold design with microchannels contains alternating layers of liquid channel, the liquid channels are physically separated to provide paths for vapor to escape. For processing, we adopt a layer-by-layer additive manufacturing approach. In this technique, individual liquid channels are processed separately and then stacked-on top of each other, physical separators are placed in between liquid channels. The space in between the liquid channel consists of the vapor channel.

The initial stage of this process entails the precise shaping of layers with specific geometric dimensions. To achieve this precision, we employ a nanosecond-pulsed ultraviolet (ns-pulsed UV) laser, Keyence Tech UMD series, which has a 10 μm resolution. The selection of the ns-pulsed UV laser is based on its ability to interact with different materials effectively. This laser possesses a high absorbance across a broad spectrum of materials. As a result, it is highly versatile and suitable for a wide range of substances. One notable advantage of the ns-pulsed UV laser is its ability to generate exceptionally clean cuts with a level of resolution that surpasses other laser types. This precision in cutting is primarily attributed to the minimal heat affected zone (HAZ) associated with the ns-pulsed UV laser. Compared to infrared (IR) or carbon-dioxide (CO_2) lasers, the HAZ produced by the ns-pulsed UV laser is significantly smaller. The reduced HAZ minimizes any undesirable thermal effects on the surrounding material, ensuring that the cut edges remain sharp and undistorted.

Following the precise cutting of the individual layers, the next step in the process involves their consolidation. Traditionally, ultrasonic welding has been a

commonly employed method for consolidating thin sheets. The use of ultrasonic welding comes with certain considerations, particularly when dealing with thin parts. One notable concern is the potential for the mandrel of the ultrasonic welder to cause deformation in these thin components.

An alternative is to thermally fuse the individual components together. This method addresses some of the problems with ultrasonic welding, particularly when working with thin materials, and has the clear advantage of being low-cost. In **Figure 4.5**, the concept of processing microchannels using an additive layer-by-layer technique is shown. To create three-dimensional geometry, thin, two-dimensional sheets with the necessary geometry can be piled on top of one another (using laser cutting, chemical etching, or stamping methods). Following pressing, the stack can be heated to a temperature that will result in a monolithic piece (typically, less than 0.5 T_m, where T_m is the melting point). If the layers are made of different materials, attention should be paid to addressing the thermal expansion mismatch between them.

(ii) Thermal sintering of liquid-microchannels

In thermal sintering, the layers that need to be fused together at their interfaces are subjected to a controlled application of heat and pressure. This method can be customized to the materials and thicknesses involved, reducing the possibility of thin portions deforming. Strong bonding between the layers can be achieved without jeopardizing the integrity of the thin components by carefully controlling the temperature, pressure, and sintering time.

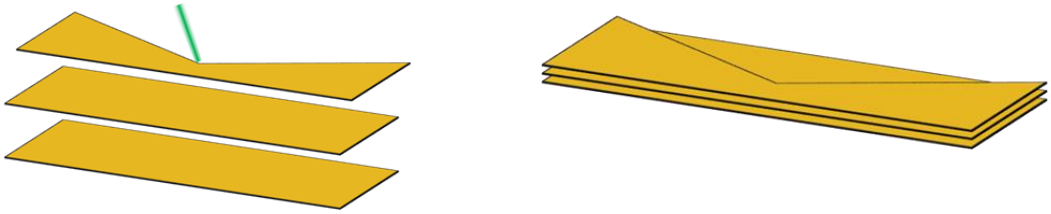

(a) Precision layer cutting by UV-laser (b) Consolidation

Figure 4.5 (a) Processing thin layers ns-pulsed UV-laser with greater than 10 μm resolution. (b) each layer is then consolidated to process liquid microchannel.

Copper layers are processed from copper shim stocks (TrinityBrand). A range of shim thickness is used for each component of the manifold. For a liquid channel the walls are prepared from 25 μm shim and the fluid routing layer in the middle of the walls is prepared from 50 μm shim. Thes spacers are prepared from stacking four 100 μm shims together. For laser cutting of copper sheets a fluence of 0.5 J/cm^2 (for 25 μm and 50 μm thickness) and 0.8 J/cm^2 (for 100 μm thickness) are applied. Fluence is calculated using the following formula:

Fluence = [((Number of repetitions x Power /Frequency) / Nominal spot size) / Raster speed] (4.1)

The cut copper sheet layers are aligned and stacked on top of one another using a stainless steel (SS316) jig. Using SolidWorks, the jig is designed to have the necessary geometry for stacking and aligning thin copper sheets. The bottom portions of the jig have two vertical *'poles'* attached to them, which can be used to align and stack copper layers in the bottom half of the jig. In essence, the top portion is made to apply consistent pressure to the stack to hold each layers together. Additionally, sufficient pressure for sintering is provided by spring and screw loading at the four corners that pass through both the top and bottom sections. Then, using springs, screws, and nuts, the jig is compressed. Next, a furnace is used to sinter the assemblage. **Figure 4.6 (a-c)**

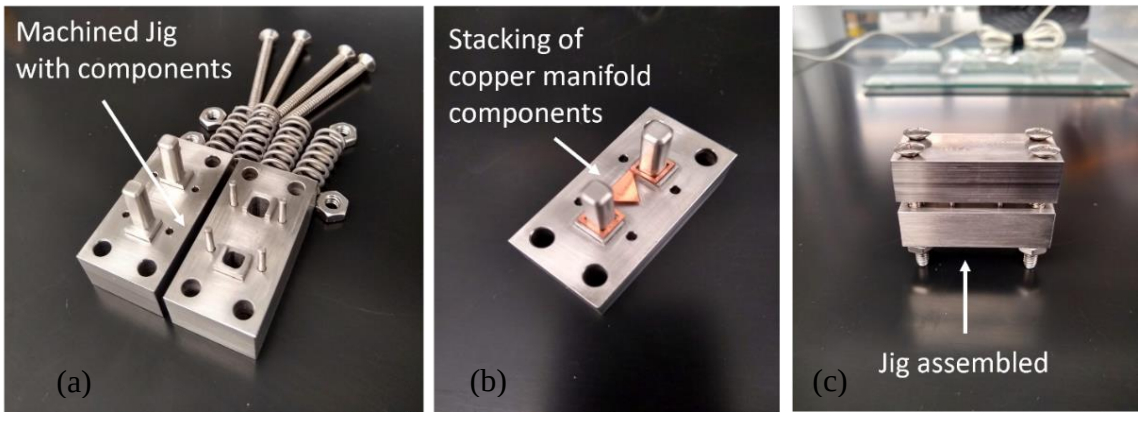

Figure 4.6 (a-c) SS-jig with top and bottom parts to sinter cut copper sheets with ns-pulsed UV laser. Poles of the jig help to stack and align each layer.

(iii) Silver assisted diffusion bonding of liquid channel from copper sheets

We use silver (Ag) plating to assist in diffusion bonding. Silver has a higher diffusion coefficient in copper than the self-diffusivity of copper. This allows us to use silver on a copper surface to aid diffusion bonding by lowering the sintering temperature, time, applied pressure or a combination of these. [6], [7]

To enhance the sintering process the copper is coated with a layer of silver by electroless plating (JAX electroless silver plating solution). Laser cut copper sheets are first cleaned in de-ionized (DI) water and then in 90% isopropanol for 5 minutes each. The copper sheets are then etched in 1% H_2SO_4 solution at 80 ^{0}C for 40 minutes, followed by a DI rinse. The etching step further cleans and roughens the copper surface. This provides better adherence of the silver coating to the copper surface during the electroless plating stage. Copper sheets are dipped into the electroless silver plating solution for 5 minutes. Then let it dry in the air for 30 minutes.

(iv) Liquid channel with copper sheets using silver microparticles

Silver particles provide an added advantage of high surface area besides the higher diffusivity in copper. The silver particles can be used in diffusion bonding of thin copper sheets. The Ag metal precursors can be composed of polymers or colloidal suspensions of metal micro and/or nano-particles suspensions. By adding water to the binder, the binder-particle mix can be made into a slip of varying viscosity. This slip can be used for micro processing of devices, a common process is the doctor-blading technique for micro-structuring. Nash *et al*. provides a comprehensive detail of the processes. [8]

For our purpose, silver microparticles in a polymeric binder (PMC silver clay) are mixed in water (1:1 ratio) to make a slurry to facilitate the doctor-blading process. Subsequently, a polyamide mask is prepared by UV-ablation using a ns-pulsed laser system. Copper sheets on which the doctor blading would take place are cleaned in DI water and subsequently etched in 1% sulfuric acid at room temperature for 10 minutes followed by another DI water rinse and drying in air.

A layer of slurry is then applied on top of the polyamide mask, and the doctor-blading technique is employed to achieve the desired design print of the middle layer of the liquid channel, consistency of the print and dimensional uniformity. Care is taken to screen-print the micropattern in a humid environment and in rapid subsequent after the slurry preparation since solvent evaporation is rapid which the viscosity of the slurry and resulting geometrical reproducibility of the micropattern.

Following the removal of the polyamide mask, the second copper sheet is placed and aligned with the underlying layer using aligning marks in rapid subsequence to mitigate the evaporation of solvent related issues. The assembly is then subjected to pressure using C-clamps and followed by drying procedures for 2 hours in the air.

We then executed liquid channel processing, starting with sintering the material in a reducing atmosphere while employing activated carbon as the reducing agent, and we maintained this condition for a duration of 30 minutes. Following this, we cleaned the sintered material with deionized (DI) water to eliminate any residues. Subsequently, we performed precise laser cutting to shape the material according to our requirements. After the laser cutting, we carried out another round of cleaning procedures, which included rinsing with DI water, followed by immersing in isopropanol and an etching step (1% sulfuric acid at room temperature for 10 minutes, and finally, a thorough DI water rinse).

(v) Liquid channel from free-standing porous wick

In this approach, the capillarity of the wick holds the working fluid in the channel rather than a rigid wall. The wick requires to be sufficiently thin to promote multiple wick installation for efficiency without losing mechanical integrity. Aligning the wicks vertically enables the implementation of a 3D structure where more liquid channels can be stacked to promote efficiency and the sufficiently high volumetric flow rate can be ensured. The wick's primary function is to hold the liquid and supply it to the porous evaporator, **Figure 4.7.** At higher powers, the liquid consumption increases and the liquid saturation on the wick decreases as discussed in previous chapters**.** For two-phase boiling**,** the heat rate can be related to the mass flow and latent heat of evaporation as,

$$q'\,[\mathrm{W}] = \dot{m}\ h_{fg} = \rho \dot{V}\ h_{fg} = (uA)\,\rho\ h_{fg} \qquad (4.2)$$

Where, $\dot{m}$ is the mass flow rate in the mesh, h_{fg} is the latent heat of evaporation, ρ is the density of the fluid, $\dot{V}$ is the volume flow rate, A is the cross-sectional area of flow and u is the superficial velocity of the fluid. We see that the superficial velocity of the fluid u in the wick is a function of the heat rate.

In the previous chapter Darcy's law is discussed in detail. According to Darcy's law the superficial velocity of the fluid,

$$u = -\frac{k_i k_r}{\mu}\nabla p \tag{4.3}$$

In the free-standing wick, the intrinsic permeability k_i is related to the geometry of the wick, porosity, and pore sizes. The relative permeability k_r is dependent on liquid saturation, **Figure 4.8.** When completely saturated the relative permeability is equal to one, when the capillary pressure of the mesh exceeds the maximum capillary pressure of the free-standing wick, then there is no percolating liquid in the wick and the relative permeability drops to zero. The saturation dependency of the relative permeability is usually experimentally determined. Furthermore, the capillary pressure also exhibits saturation dependency. We use a copper mesh as our porous wick for liquid delivery to the porous evaporator in this approach. The geometry of the wick is described in the previous chapter. A rigorous discourse on this topic is discussed in [9].

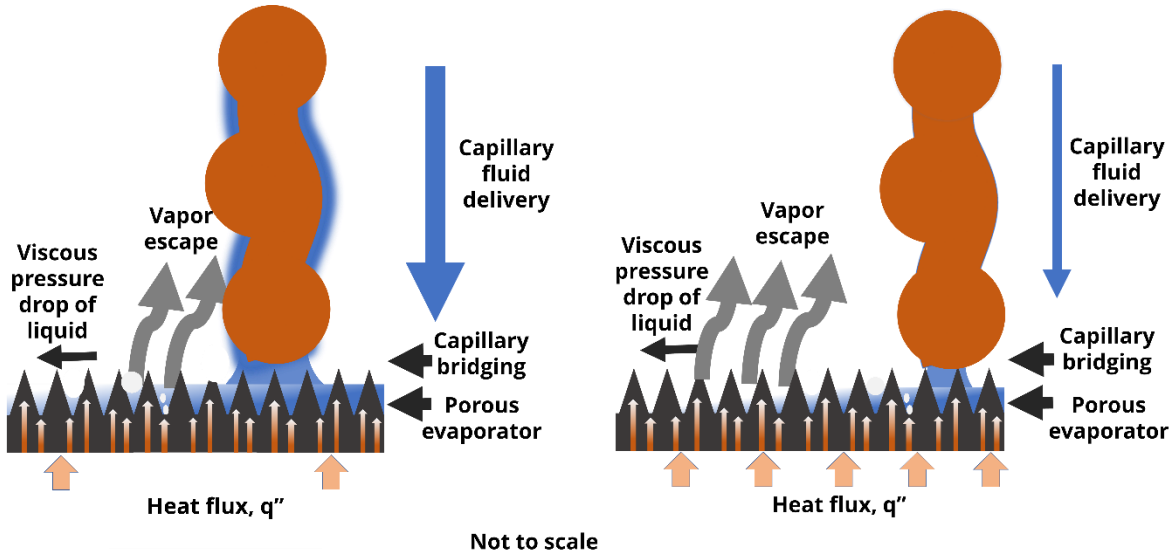

Figure 4.7 Liquid saturation of a free-standing wick changes with heat flux of a porous heat-spreader.

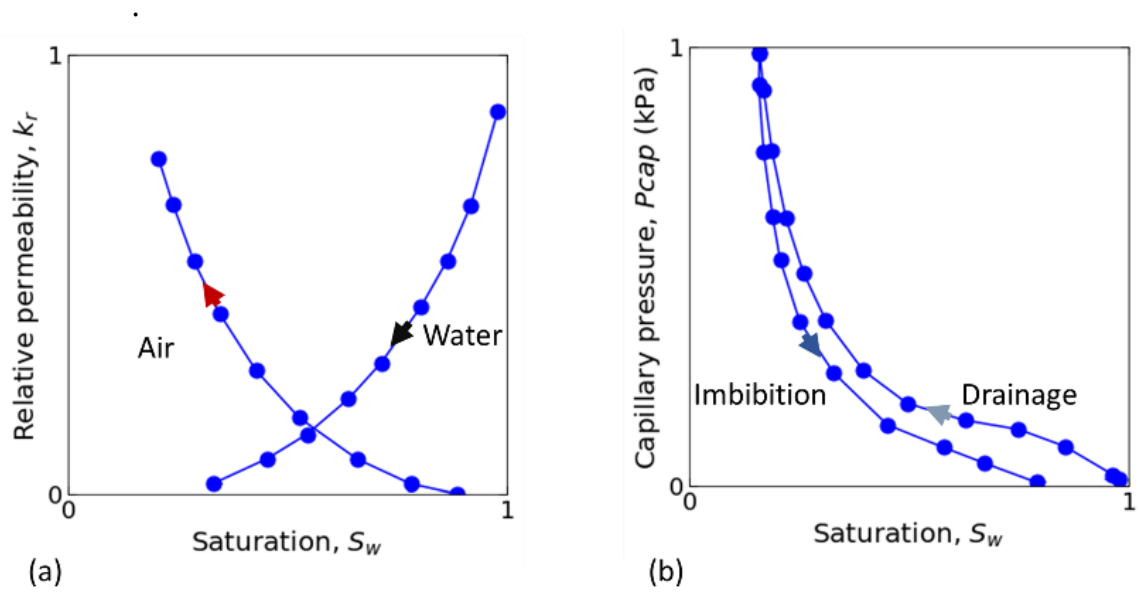

Figure 4.8 Saturation dependence of relative permeability and capillary pressure.

4.2.2 Controlled Distribution of Phases via 3D Manifold

A three-dimensional manifold structure consisting of parallel free-standing porous wick can be integrated in a three-dimensional manifold structure. The space in between liquid channels is utilized as the vapor escape channel. **Figure 4.9** schematically describes the geometry of the 3D manifold to control fluid delivery and vapor escape. The free-standing mesh, for example, a copper mesh can transport liquid via capillary action to the heated surface. We can use spacers, for example, copper spacers in between the meshes to create empty spaces for vapor to escape, vapor channel. The meshes and the spacers are stacked alternatively using a stainless-steel jig similar to the process described in **Figure 4.6** and then sintered at 800^0C for an hour in a furnace in a reducing atmosphere. After sintering, the manifold is rinsed in DI water and acetone for 10 minutes and then etched in 1% sulfuric acid for 10 mins and then rinsed in DI water and then dried in air.

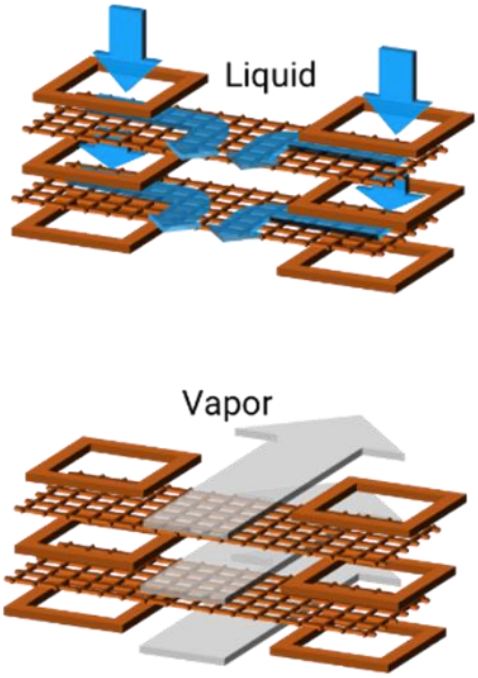

Figure 4.9 Design of a 3D manifold with free-standing mesh wick

4.2.3 Porous heat spreader

The function of the manifold does not depend on the specifics of the porous heat spreader employed. However, the manifold design discussed is interfaced with an AlN, pin-fin porous wick. AlN is a good thermal conductor (~150 W/mK) but is electrically insulating. These properties make AlN an attractive substrate material for electronics packaging. The porous heat spreader is crafted in AlN using a ns-pulsed UV laser. These microstructures aid in capillary suction of heat-transfer liquid and maintain a thin film on the evaporator surface to enhance the heat transfer performance of the two-phase heat transfer system.

4.2.4 Modeling of fluid flow in mesh liquid channel at varying capillary pressure

Based on the wick behavior determined in Chapter 2, we simulate fluid flow on a single mesh wick in the manifold at different heat flux conditions. Permeability changes with capillary pressure of the fluid flow inside the copper mesh which can be used to capture pressure distribution and fluid superficial velocity distribution in the mesh liquid channel in different heat flux conditions.

We simulate a single mesh, half of its actual width and apply a periodic boundary condition to the right side of the mesh. The other half of the mesh will essentially contain the mirror image of fluid flow properties. The simulated mesh geometry is 2.5 mm in x-axis and 5 mm in y-axis, which means this is a half section of 5 mm x 5 mm mesh. The mesh boundary at the bottom is subject to a uniform heat flux for the entirety of the 2.5 mm length. No-flux boundary conditions are applied to the top and right border and constant pressure boundary conditions are applied to the left. We apply a fixed velocity boundary condition at the bottom. The velocities ($u\delta$) are varied corresponding to each heat fluxes, q''. **Figure 4.10.**

If we have a total heat flux of 460 W/cm² and an area of 1 cm², this results in a total power of 460 W when considering a length of 1 cm and a gap of 625 μm. In this configuration, we can divide the 1cm length by the 625 μm gap, which yields 16 meshes.

As a result, each mesh will handle (460 W / 16) = 28.75 W of power.

The thickness-normalized superficial velocity of the fluid for corresponding heat-rate can be determined by the following formula:

$$u\delta = q'' / (h_{fg}\, \rho\, w) \tag{4.4}$$

where w is the width of the mesh, ρ is the density of the fluid and h_{fg} is the latent heat of evaporation of the fluid.

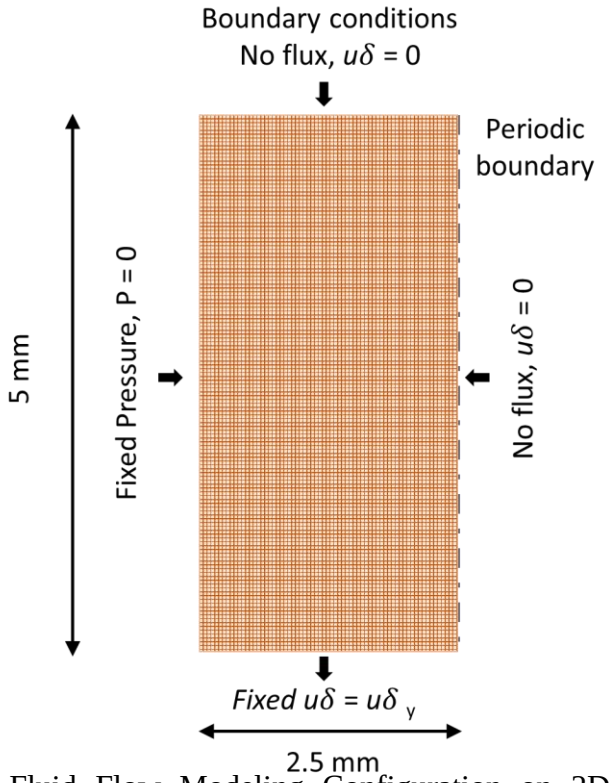

Figure 4.10 Fluid Flow Modeling Configuration on 2D Mesh Liquid Channel Using Finite-Difference Method: The simulation involves a 2.5 mm x-direction and 5 mm y-direction area of copper mesh. Boundary conditions consist of a fixed pressure (P=0) at the left, no flux at the right and top boundaries. A dotted line on the right boundary signifies periodic behavior, mirrored beyond this line. At the bottom boundary, a fixed $u\delta$ is enforced, aligned with the applied heat flux.

For heat fluxes varying from 115 W/cm^2 to 460 W/cm^2, corresponding $u\delta$ of 1.6 x 10^{-6} m^2/s to 5.6 x 10^{-6} m^2/s, respectively, calculated using Equation 4.4.

The flow equation was solved using a finite difference method written in MATLAB which solves the following equation,

$$P_{new} = P_{old} + (dt / \mu\alpha) [((k_i\, dP_i + k_j\, dP_j) / dx^2 + (k_l\, dP_l + k_m\, dP_m) / dy^2)] \qquad (4.5)$$

Where, μ = viscosity, dt = time differences, k_i, k_j, k, k_m is permeability in left cell, right cell, top and bottom cells, respectively. d_{Pj}, d_{Pj}, d_{Pl}, d_{Pm} are pressure

differences along the left, right, top, and bottom directions. A is the stability criterion. P_{old} is the original pressure matrix that is being updated. When the difference between P_{new} and P_{old} reaches the tolerance limit, the pressure converges. The gradient of the pressure matrix gives the fluid velocity direction for each iteration, respectively. α is a variable used for the stability of the equation.

4.3 Results and discussions

In this section we will discuss our findings from different processing methods of liquid channels discussed in the previous section. We will then discuss 2D flow modeling behavior of liquid in a mesh wick:

4.3.1 Sintering of Cu-Cu liquid channel

The ns-pulsed UV laser cut cleanly different thicknesses of copper sheets **figure 4.11(a).** The copper sheets that were stacked and aligned inside the SS-jig are fully consolidated after sintering at 800^0C for one-hour. However, due to the thermal expansion of copper, grain coarsening and softening, and differences of thermal expansion in different sections of the liquid channel unevenness in the openings appeared. **Figure 4.11 (b).**

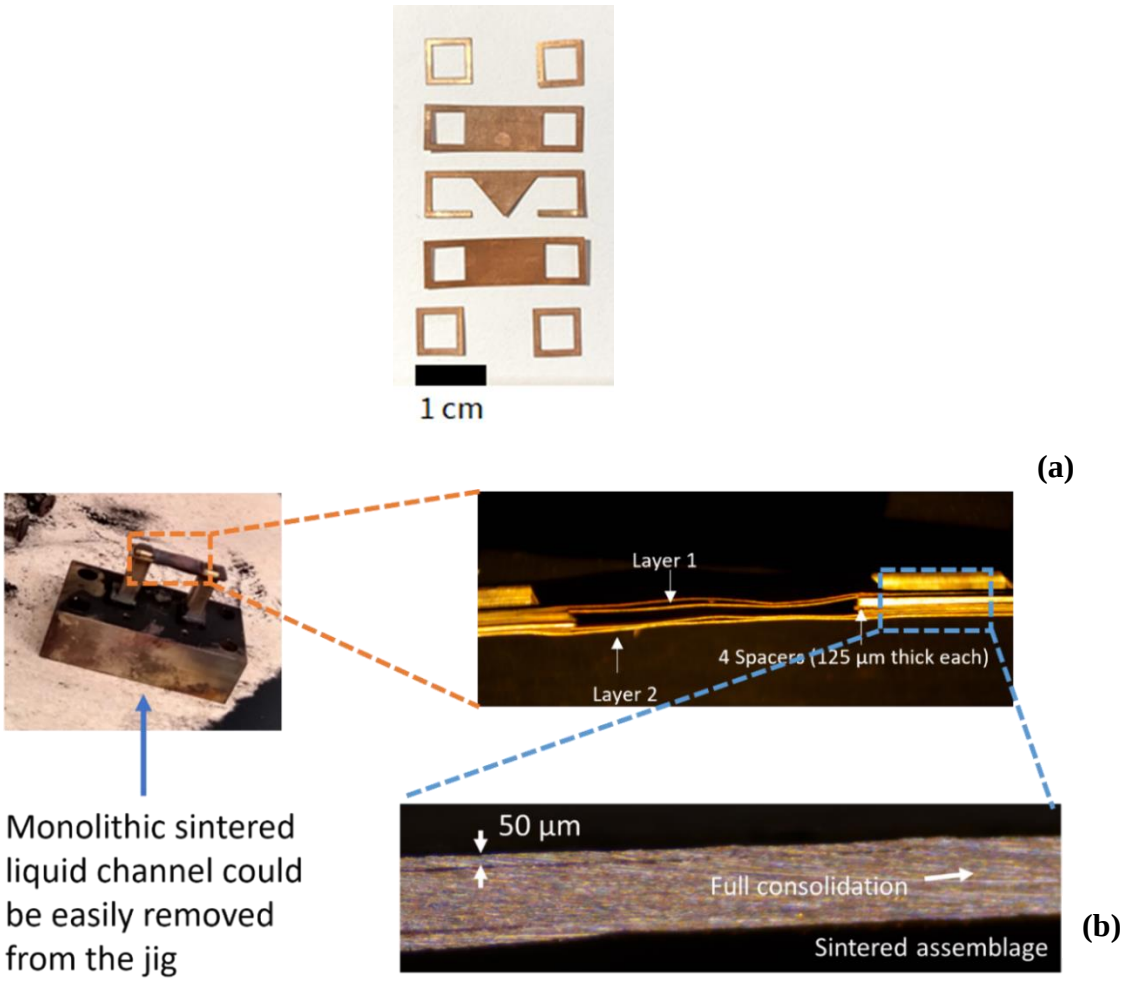

Figure 4.11 (a) cut copper sheets with required dimensions using ns-pulsed UV laser. **(b)** monolithic copper liquid channel after sintering. The middle unsupported part shows unevenness after sintering due to difference in thermal expansion coefficient.

When copper thin sheet layers are pushed together and given support to hold the stack together, this technique ensures sufficient bonding between the layers. Reaching the necessary geometrical tolerance is challenging in the unsupported region, though. This can be resolved extrinsically by adding external layers that hold and separate the unsupported parts and do not bond with the copper during sintering, or intrinsically, by designing microchannels that offer columns of support in the middle layer and designing jig assemblies that allow for thermal expansion mismatch. For this purpose, thin carbon sheets are found functional.

4.3.2 Sintering of silver assisted copper liquid channel

The electroless silver plating of copper reduced the sintering temperature from 800 ^{0}C to 700 ^{0}C and sintering time was reduced by an hour.

From **figure 4.12 (a-b)** we observe that, after sintering, consolidation between different thin layers is observed. The unsupported section at the middle show unevenness in the interlayer distances.

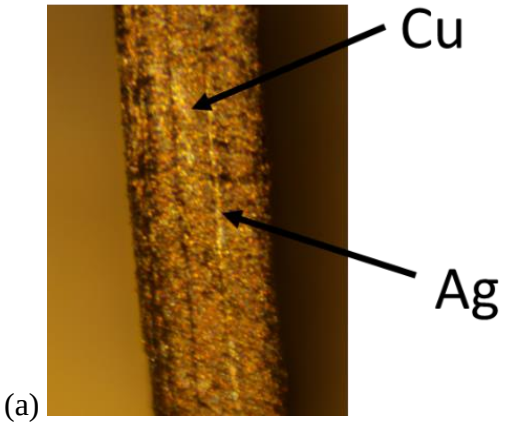

(a)

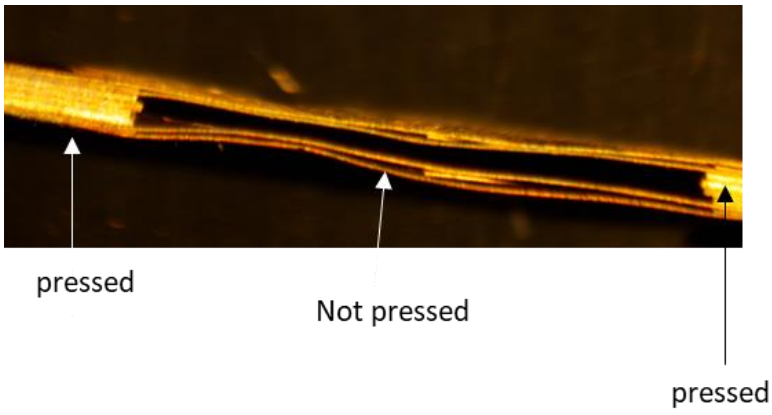

(b)

Figure 4.12 Silver assisted diffusion bonding of liquid channel with thin copper sheets and spacers. **(a)** Siler assists in bonding copper sheets. **(b)**The middle part of the liquid channel appears to be uneven, but less so compared to when silver plating is not used for sintering thin copper sheets.

Silver has a higher diffusivity in copper, electroless silver plating on thin copper sheets benefits lowering the sintering temperature and time.[7] The copper sheets that have been diffusion-bonded are sufficiently bonded to hold the several layers together as a monolith. In comparison to copper self-diffusion bonding, the unsupported layers have less waviness or unevenness because of the shorter sintering time and lower sintering temperature.

4.3.3 Sintering of silver particles assisted copper liquid channel

The polymer bound silver microparticles can be doctor bladed using a polyimide mask to lay down the required microstructures on a copper surface, **figure 4.13 (a-d).** After pressing, drying and sintering two copper sheets at the top and bottom of the middle microstructure layer from silver microparticles make one monolithic structure. The monolith is subsequently cut using a ns-pulsed UV laser for the required dimension of liquid channel geometry. This process constitutes an even joint, without waviness. **Figure 4.13 (e)** The strength of joints are not tested.

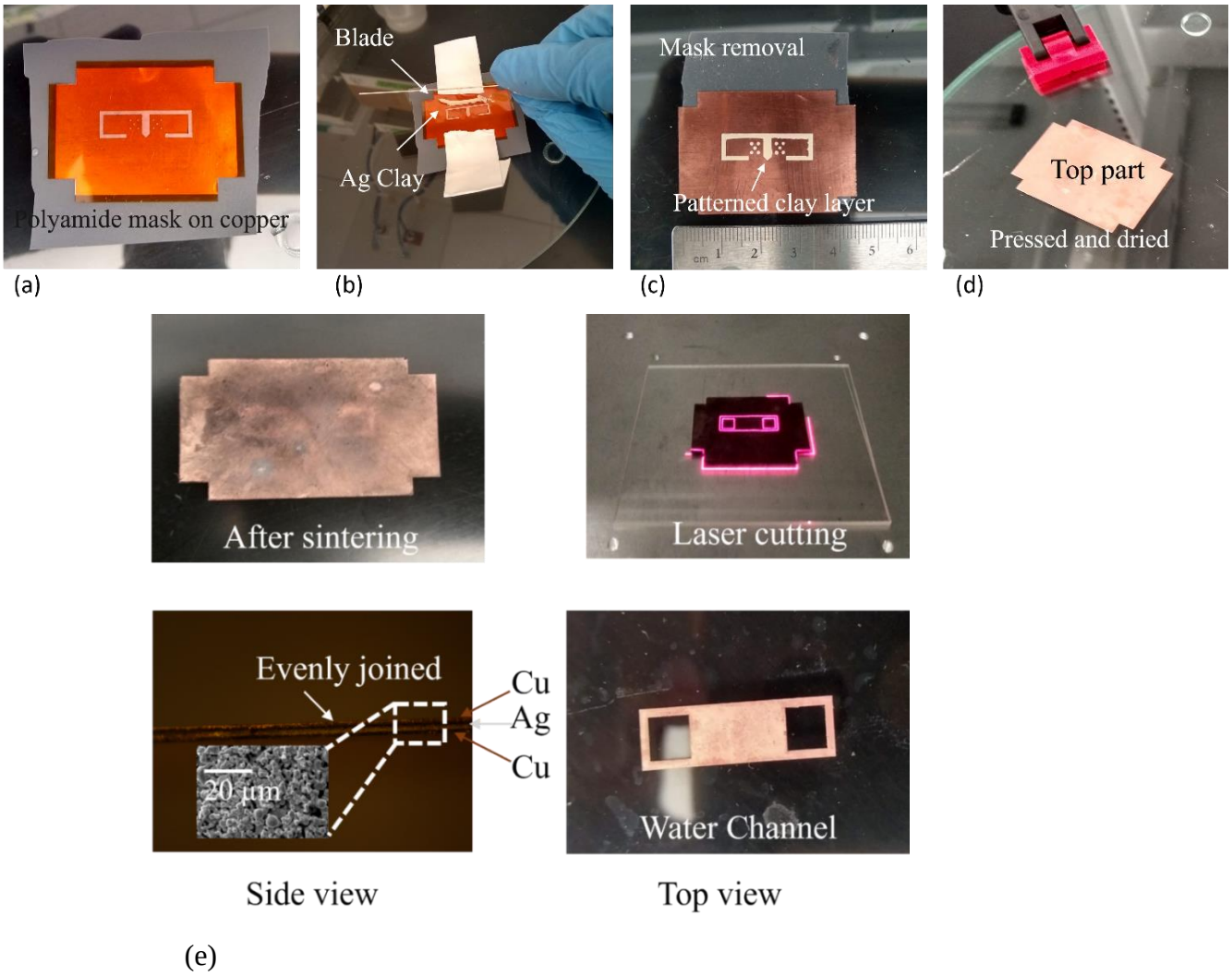

Figure 4.13 Micro-channel processing with silver micro-particles assisted doctor blading diffusion bonding process **(a-e)**

Using silver microparticles for micropatterning has the benefit of creating intricate geometries up to 10 μm resolution, that is, the resolution of the ns-pulsed UV laser sets the limit. Processing microfluidic devices like the liquid channel that was previously addressed can benefit from this. While keeping the geometrical tolerance, the silver particles help to lower the sintering temperature and duration of the processes. We did not witness the waviness and unevenness noted for the other approaches mentioned above.

4.3.4 Manifold using free-standing porous wick

The nanosecond pulsed UV laser can directly process a liquid channel from cutting a from a stock of mesh with required geometrical requirements. A fluence of 1 J/cm^2 is used for cutting the copper mesh. The liquid channel is produced from a copper mesh stock in a one-step process by UV laser cutting and the mesh channel maintains the geometrical requirements. **Figure 4.14**

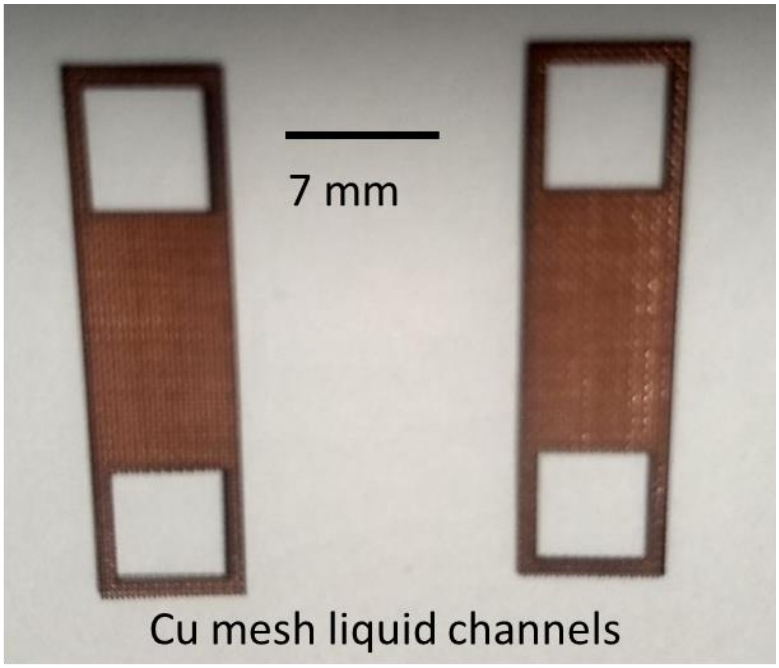

Figure 4.14 Liquid microchannel made of copper mesh, processed by cutting from a stock of mesh by a ns-pulsed UV-laser.

The layer-by-layer additive manufacturing approach described in section 4.2.1 results in a three-dimensional monolithic metallic manifold structure where the mesh liquid channels are separated by copper spacers. **Figure 4.15** The space in between the liquid channels aids in vapor escape.

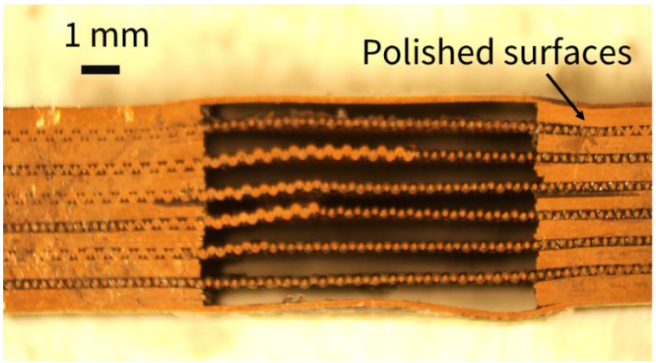

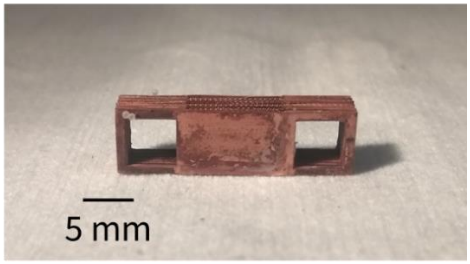

Figure 4.15 Three-dimensional monolithic metal manifold made of copper mesh liquid channel and copper spacers.

4.3.5 Fluid flow simulation results

Figure 4.16 plots the results from the simulations of fluid flow in copper mesh at different heat flux conditions. The relationship between heat flux, velocity, and capillary pressure within a mesh used inside a manifold for fluid distributions at two-phase heat transfer applications is captured. We can visualize capillary pressure (*Pc*) distribution across the mesh, accompanied by fluid the velocity field ($u\delta$), in black arrows. In each distinct scenario denoted as (a) to (d), the heat flux ranges from 115 W/cm² to 460 W/cm², with corresponding uδ values imposed at the lower boundary. Notably, the presence of white region in **Figure 4.16 (e)** signifies regions where the capillary pressure exceeds the maximum capillary pressure of the mesh wick (*Pc(max)*), indicating the absence of percolating water.

Additionally, plot (e) presents $u\delta$ values corresponding to different heat fluxes plotted against capillary pressures, represented by white circles. A sudden and significant rise in capillary pressure beyond a specific $u\delta$ threshold, surpassing the maximum capillary pressure of the mesh wick as denoted by the red dotted line (*Pc(max)*).

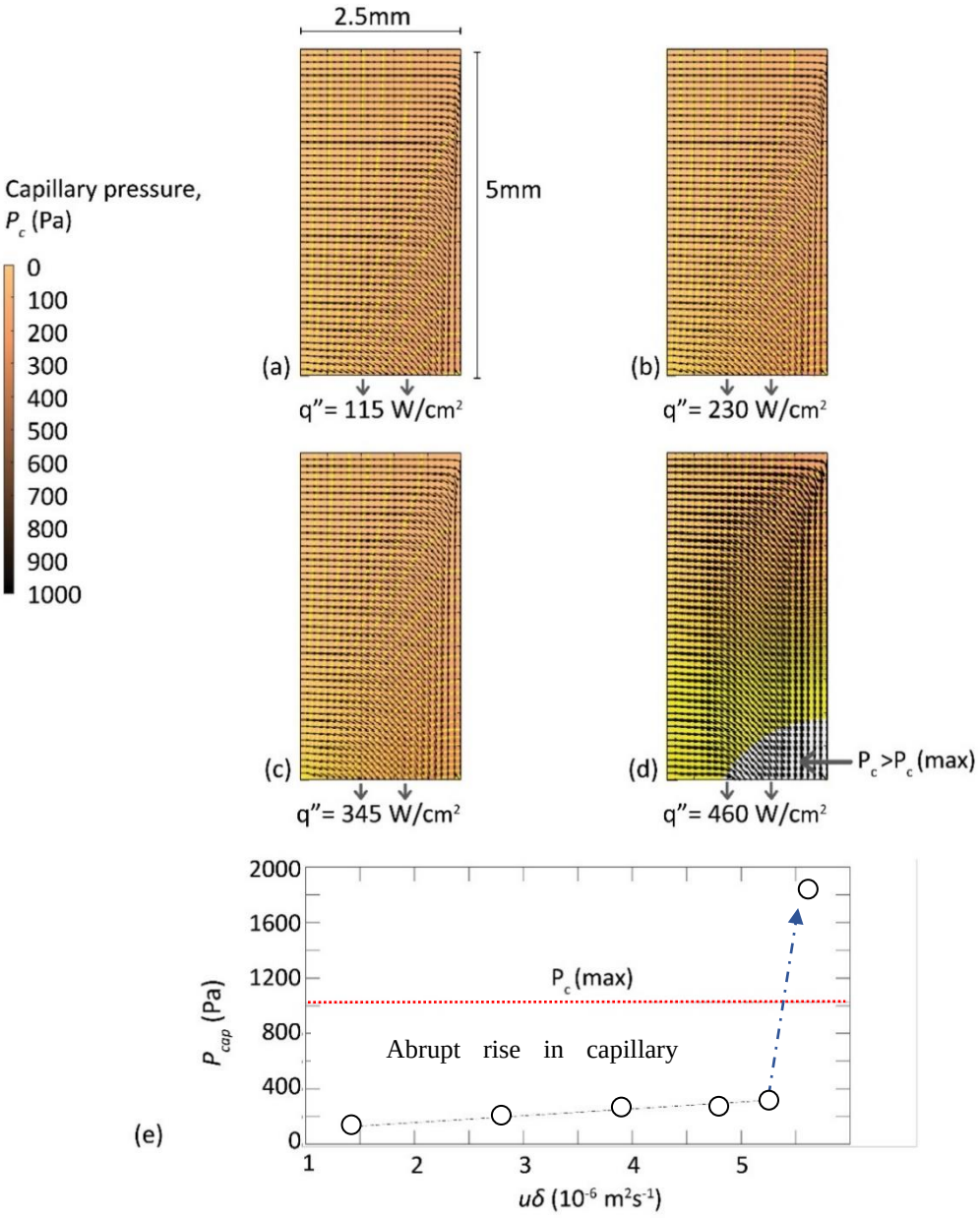

Figure 4.16 Simulation insights into the fluid flow in mesh at different heat flux conditions: The contour plot illustrates the spatial distribution of capillary pressure, *Pc*, across the mesh, complemented by white arrows representing the velocity field $u\delta$. For each scenario (a)-(d), heat flux spans 115 W/cm² to 460 W/cm², with corresponding $u\delta$ values applied at the lower boundary. Notably, the white area indicates regions where P_c surpasses $P_{c\ (max)}$, signifying the absence of percolating water. (e) plots the $u\delta$ corresponding to different heat

fluxes vs, capillary pressures, white circles. We see an abrupt increase in capillary pressure beyond a certain $u\delta$ value which exceeds the maximum capillary pressure of the mesh wick (red dotted line, $P_c(max)$)

According to our 2D simulations of fluid flow through a mesh, the capillary pressure rises above the maximum capillary pressure of the mesh with heat fluxes of about 460 W/cm^2. 460 W/cm2 of heat flux can thus be supported by the mesh manifold.

4.3.6 Microstructure of porous heat-spreader

Figure 4.17 shows an SEM image of porous microstructures crafted on AlN using a ns-pulsed UV laser. From the image the pin-fin micro-structures conical pyramidal in shape with approximate diameter of 30 μm and height of 110 μm. Laser ablation results in rough surfaces of the pin fins. We conduct profilometry to measure the surface roughness of 1.25 μm on average. The high surface area and the surface roughness of the AlN pin-fin microstructures aid in capillarity and are effective heat spreaders for capillary driven two-phase heat transfer.

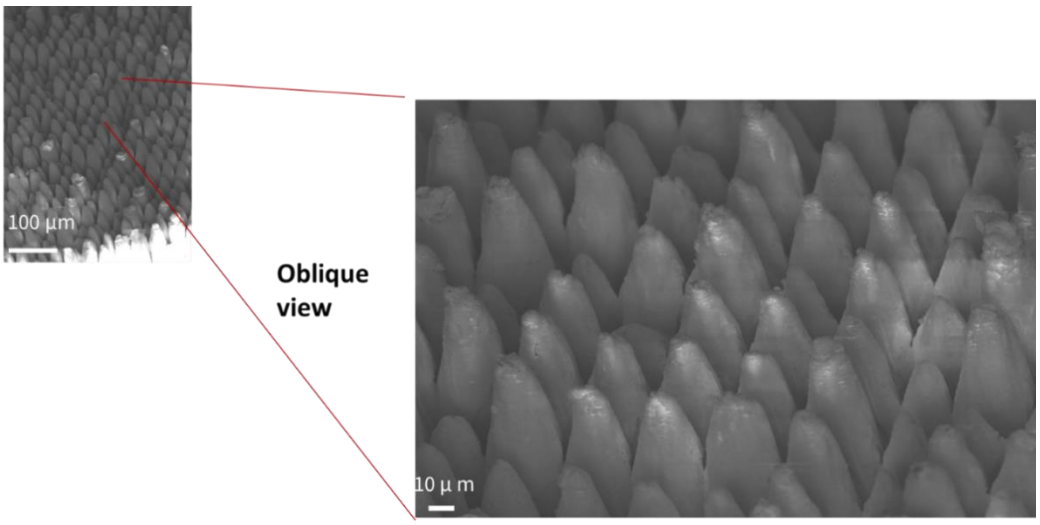

Figure 4.17 SEM of microstructures crafted on AlN using ns-pulsed UV laser.

4.4 Conclusions

We designed a system to enhance the pool boiling performance of a porous heat spreader. The design involves even-distribution of fluid on the heat spreader to tackle the viscous pressure loss the heat transfer fluid. Several equally spaced liquid channels can be used for this purpose, vapor can escape in between the liquid channels. This in turn, reduces the competition between liquid delivery and vapor escape to and from the heat transfer. The liquid channel can be processed by layer by layer thin-sheet additive manufacturing via a sintering route. The thermal expansion mismatch can be an issue in maintaining geometrical integrity. Direct processing of liquid channel from a free-standing mesh like structure is a more straightforward and robust way of processing a liquid channel. After sintering the resulting 3D monolithic manifold exhibits required structural and geometrical consistency.

4.5 References

[1] M. Dede, Ercan M.; Zhang, Chi; Wu, Qianying; Seyedhassantehrani, Neda; Shattique, K. Roy, Souvik; Palko, James W.; Narumanchi, Sreekant; Kekelia, Bidzina; Sougata, Hazra; E. Goodson, M. Giglio, Roman; Asheghi, and *, “Heat Flux Micro Coolers Having Multi-Stepped Features And Fluid Wicking,” 2022

[2] E. M. Dede et al., “Techno-economic feasibility analysis of an extreme heat flux micro-cooler,” iScience, vol. 26, no. 1, p. 105812, Jan. 2023, doi: 10.1016/j.isci.2022.105812.

[3] J. W. Palko et al., “Approaching the limits of two-phase boiling heat transfer: High heat flux and low superheat,” Appl Phys Lett, vol. 107, no. 25, Dec. 2015, doi: 10.1063/1.4938202.

[4] A. Bar-Cohen et al., “The ICECool Fundamentals Effort on Evaporative

Cooling of Microelectronics," IEEE Trans Compon Packaging Manuf Technol, 2021, doi: 10.1109/TCPMT.2021.3111114.

[5] J. W. Palko et al., "Extreme Two-Phase Cooling from Laser-Etched Diamond and Conformal, Template-Fabricated Microporous Copper," Adv Funct Mater, vol. 27, no. 45, pp. 1–8, 2017, doi: 10.1002/adfm.201703265.

[6] Y. L. Chen and C. C. Lee, "Strength of solid-state silver bonding between copper," Proceedings - Electronic Components and Technology Conference, no. May 2013, pp. 1773–1776, 2013, doi: 10.1109/ECTC.2013.6575815.

[7] W. K. Kelley, W. C. Cowden, E. M. Lopez, W. K. Kelley, and W. C. Cowden, "Use of Electrodeposited Silver as an Aid in Diffusion Welding variables influencing the diffusion welding process," no. January, pp. 26–34, 1984.

[8] C. Nash et al., "A Comparative Study on the Conductive Properties of Coated and Printed Silver Layers on a Paper Substrate," J Electron Mater, vol. 44, no. 1, pp. 497–510, Jan. 2015, doi: 10.1007/s11664-014-3434-5.

[9] F.A.L. DULLIEN," 5 - Multiphase Flow of Immiscible Fluids in Porous Media", Porous Media (Second Edition),Pages 333-485,1992https://doi.org/10.1016/B978-0-12-223651-8.50011-0.

Chapter 5

Reliability of Aluminum Nitride (AlN) in Pool-Boiling Conditions

5.1 Introduction

AlN is a useful substrate material because of its high thermal conductivity (polycrystalline AlN has a thermal conductivity of ~150 W/mK), low electrical conductivity, and superior mechanical strength. However, the practical use of AlN wafer substrates in electronic packaging has been difficult due to their water sensitivity. Bowen *et al.* showed that AlN powders react with water at room temperature to create aluminum hydroxides.[1] Morphologically, these hydroxides are porous in nature. The reaction with water follows an unreacted core model, meaning that the kinetics are reaction-controlled.[2]–[5] Similar reaction mechanisms with water at elevated temperatures for AlN powder (up to 90 ^{0}C) were also observed.[6] Abid *et al.* found that AlN powders reacted with water at 100 ^{0}C (10 minutes) to form AlOOH.[7] Sato *et al.* found that water vapor at very high temperatures (900 ^{0}C to 1250 ^{0}C) also reacts with AlN linearly (controlled by surface reactions). [8]

Recent advances in facile micro-processing pave the way to use AlN as a two-phase heat transfer substrate where water boils directly on the AlN microstructures to extract heat from a high heat flux dissipating device. [9], [10]To our knowledge, the corrosion behavior of polycrystalline AlN wafers in the nucleate pool boiling scenario has yet to be studied. In this work, we systematically characterize the corrosion behavior of AlN in pool boiling conditions and the corrosion behavior at varying heat fluxes using profilometry. A profilometer is a surface contact tool that measures a sample's three-dimensional form by dragging a stylus across its surface and is a facile and rapid tool to detect and characterize corrosion on a surface.

Furthermore, we delve into corrosion mitigation strategies by creating a thin, durable surface oxide layer via thermal oxidation in air at atmospheric

pressure. Surface oxidation has been traditionally used for better metallization of the AlN surface for direct bonded copper (DBC) used in electronics packaging. Our investigations find that thermally growing a thin oxide layer on the AlN surface is a facile one-step process to mitigate corrosion of AlN wafers used in two-phase heat transfer. This research may help make AlN a more viable substrate material for electronics packaging, particularly for cooling via two-phase heat transfer.

5.2 Materials and Methods

In this section we will describe our experimental method and the experimental setups to quantify corrosion of AlN during high heat-flux pool boiling conditions. Additionally, we describe the method and experimental setup of quantifying AlN corrosion in ambient pool boiling conditions.

5.2.1 AlN substrate preparation

Coupons of AlN with dimensions 15 mm x 15 mm are cut using a ns-pulsed UV laser (Keyence Tech UMD series) from AlN wafers (MSE Supplies, 0.5mm thickness). Pool boiling is carried out on the AlN surface where it comes into contact with water, at the center of the AlN coupons, for a heated area measuring 4 mm x 4 mm. Then the coupons are cleaned in 90% isopropanol solution for 10 mins by dipping and subsequently dried in a desiccator for one hour.

5.2.2 Heater preparation

The AlN wafers are heated using a thin-film heater, placed at the opposite of the boiling surface. As substrate cleaning and preparation protocol, we dip AlN coupons in isopropanol for 10 minutes, then drying, and plasma cleaning (O_2 + Argon) for 5 minutes. The thin film heater is processed using electron beam (eBeam) evaporation (AJA International, model: ATC-2036-E-T Evaporation Systems). The process of eBeam evaporation involves heating a solid target

source with an electron beam in order to produce vaporized materials that condense on substrates in an environment of high vacuum.

Several coupons are mounted on a large, gridded sample holder using Leit tabs (Fisher Scientific). Leit tabs are double-sided, electrically conductive, carbon-based adhesive discs. **Figure 5.1**. A thin film (20 nm Ti + 200 nm Pt) is deposited on the AlN surface via eBeam evaporation.

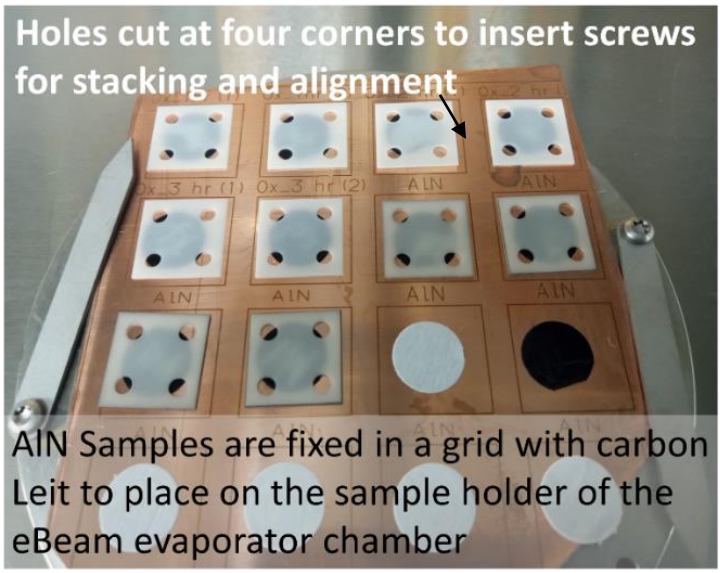

Figure 5.1 15 mm x 15 mm AlN coupons are placed in a gridded sample holder using carbon Leit for eBeam evaporation of Pt thin film.

After the thin-film deposition process, we annealed the thin-film heater in a vacuum oven at 150^{o}C for 3 days to stabilize the temperature coefficient of resistance (TCR) for platinum. The measured sheet resistance is 7 Ω/square sheet resistance. This Pt based thin film heater could operate at 200 W/ cm^2 heat flux without any deterioration; higher heat flux operations were not tested for this experiment.

Additionally, a second set of thin film heaters are prepared with a thin, 12.7 μm thickness, Stainless Steel (SS) shim (TrinityBrand) by cutting a heater

design with a pulsed UV laser. We obtain 4 Ω/square sheet resistance for the heater design shown in **Figure 5.2**. This heater can survive up to a heat flux up of 80 W/cm^2 before melting.

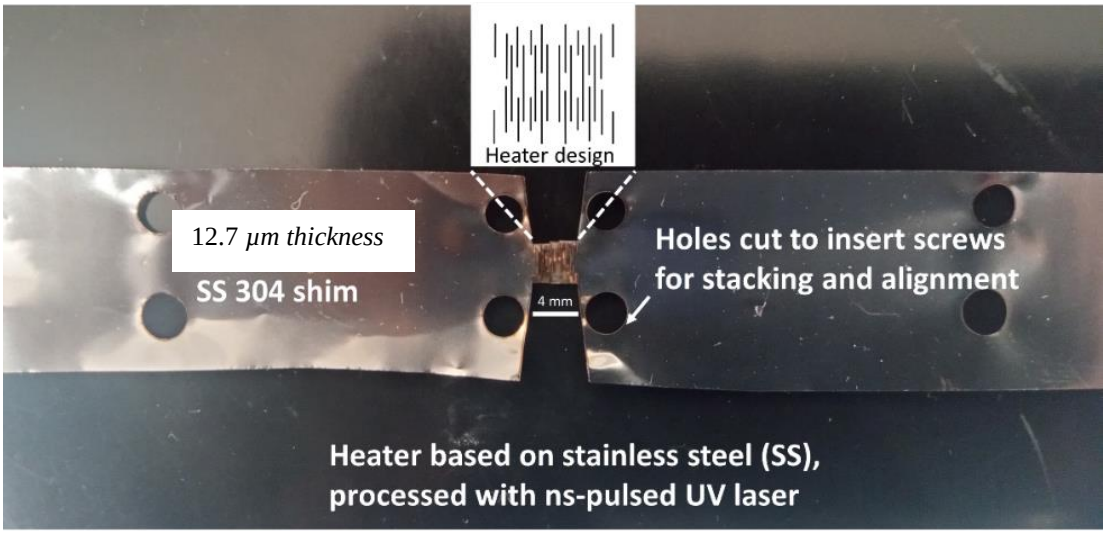

Figure 5.2 Thin film heater made of SS shim 12.7 μm, processed by ns-pulsed UV laser, sheet resistance of 4 Ω/square. The scale bar represents 4 mm.

5.2.3 Surface treatment of AlN

We have investigated three different surface treatment protocols of AlN in order to reduce the corrosion caused by boiling water. We explore processing a thin layer of surface coating grown chemically from the AlN surface that would be durable during the extended high-heat flux conditions of pool boiling. Three different surface conditions are being considered:

5.2.3.1 Thin Al coating on top of AlN without further treatment

This method applies a thin coating of Al on AlN to protect AlN surface from corrosion in pool boiling. For this purpose, we evaporate a 200 nm thick Al layer on AlN via eBeam evaporation technique. No further surface oxidation step is carried out surface coating step with evaporation. The evaporated sample is cleaned in acetone for 5 minutes before the boiling experiment to assess corrosion.

5.2.3.2 Oxidation of plain AlN

We develop a surface treatment of AlN by oxidizing its surface to an elevated temperature in air to grow a protective surface layer of Al_2O_3. Chun-Ting *et al*. investigated oxidation mechanism of bulk AlN in air in the temperature interval from 1050℃ to1450 ℃.[11] Their study found that either diffusion of oxygen or reaction with oxygen of the AlN surface governs the oxidation. The chemical reaction oxidizes AlN to Al_2O_3 and releases N_2.

$$2AlN\,(s) + 1.5\,O_2\,(g) \rightarrow Al_2O_3\,(s) + N_2\,(g) \qquad (i)$$

They report the extant of oxidation through the thickness of the oxide layer. **Figure 5.3 (a)** The oxygen mapping in the surface region is displayed in **Figure 5.3 (b)**. The layer thickens quickly as the temperature above 1250 °C is reached during oxidation. However, after oxidization at 1450 °C for two hours, the thickness of the oxide layer reaches its plateau. The porous nature of the oxide layer plays a part during the oxidation of AlN, **Figure 5.3 (a)** According to**,** reaction (i) nitrogen is formed in tandem with the oxidation of AlN. The release of nitrogen during this reaction leads to small pores, creating a significant amount of new surface area that facilitates subsequent reaction, the oxide layer can grow. On the other hand, the process can only occur when there is a possibility of nitrogen and oxygen exchange. The pore channels permit the gaseous transfer. When the oxide layer reaches a maximum thickness, as shown in **Figure 5.3 (a)**, it is hypothesized that the pore channels might no longer be accessible. Only the diffusion of oxygen ions within the oxide layer is feasible due to the lack of interconnectivity between the pores. Because of the modest ion

diffusion coefficient in Al_2O_3, the thickness rises slowly at high temperatures. About 80 μm is found to be the crucial layer thickness, beyond which no further oxidation occurs even if the time of oxidation is increased. **Figure 5.3 (b)** Oxidation at 1350 °C for 4 hours or 1450 °C for 1 hour is required to obtain this thickness. At these higher oxidation temperatures, the oxidation is diffusion controlled: oxidation thickness increases parabolically with time. The oxidation that occurs between 1050 °C and 1350 °C is reaction controlled and the extant of oxidation is linear with time, its activation energy can be determined. They report 187 kJ/mol is the activation energy value. [11]

Because of the reaction control mechanism and less porous nature of the oxidation product, **Figure 5.3 (a)**, we oxidize our AlN in a furnace at 1050 ^{0}C. We extracted data from the plot to determine oxide thickness vs. time relationship. From **Figure 5.4** we find that for 1 hour, 2 hour and 3 hours of oxidation time, 1 μm, 2 μm and 3 μm thick oxide layers can be grown on AlN, respectively. We, therefore, oxidize each AlN sample in air for 1 hour, 2 hour and 3 hours, respectively inside a furnace.

5.2.3.3 Thin Al coating on top of AlN followed by oxidation at high temperature

These samples are first prepared by coating with a thin Al layer on-top of the AlN surface following the step described above, and then further carrying out an oxidation step. The Al coated AlN are heated in a furnace to 1050 ^{0} C in air environment for 2 hours. Similar mechanism of oxidation is expected for the surface treatment described above, thin Al coating on top of AlN followed by oxidation at high temperature.

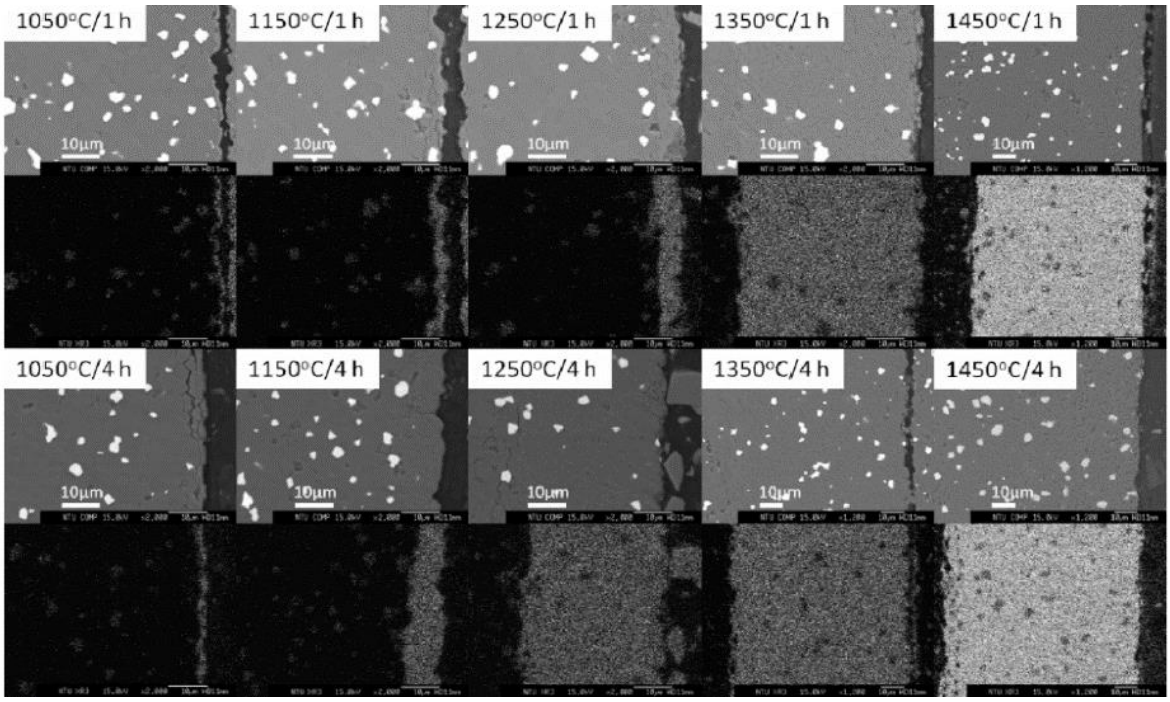

(a)

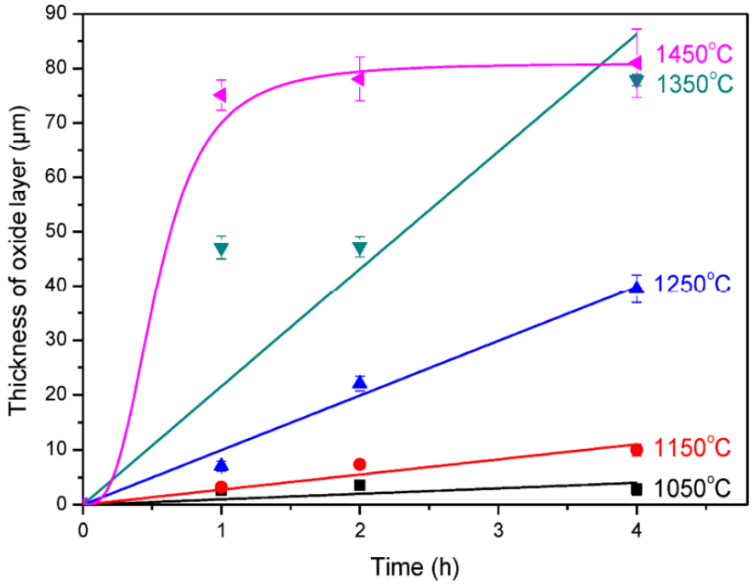

(b)

Figure 5.3 (a) Oxide layer thickness at different temperatures as a function of oxidation time. **(b)** The oxygen maps that correspond to the surface region of oxidized AlN specimens were obtained using SEM back-scattered micrographs. Reprinted with permission from [Yeh, CT., Tuan, WH. Oxidation mechanism of aluminum nitride revisited. J Adv Ceram 6, 27–32 (2017). https://doi.org/10.1007/s40145-016-0213-1licensed under CC BY 4.0.]

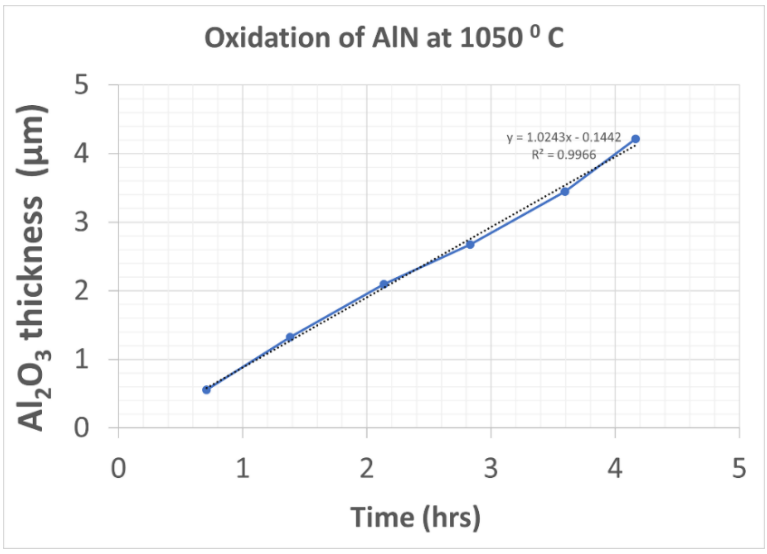

Figure 5.4 AlN reacts with O_2 in air at 1050 ^{0}C. The oxidation mechanism is reaction-controlled; the thickness of the oxide layer grows linearly with oxidation time. Data extracted from **Figure 5.3(a).** [11]

5.2.4 Experimental method of quantifying corrosion of AlN in pool boiling

In this section we describe the experimental method to determine corrosion rate of AlN and surface treated AlN in pool boiling conditions. We consider experiments to measure corrosion rate at varying heat fluxes for pool boiling and a separate experiment for corrosion of AlN at the ambient condition of boiling.

5.2.4.1 Boiling experiments at varying high heat fluxes

Heat is generated at the bottom surface of the AlN sample by current flowing through the thin-film heater. This heat is then transferred through the thickness of the sample to the top surface of the AlN, which is in contact with water. By passing various current densities through the heater with the aid of a power source, heat fluxes can be adjusted. To prevent thermal shock that can burn the heater material, the applied power is ramped up to the target level. Python's Serial module is used to make a Data Acquisition system (DAQ). On the upper surface, water boils and simultaneously interacts with the AlN surface to produce corrosion products. **Figure 5.5.** The boiling experiment setups are insulated from the pool to prevent heat loss to the ambient. Using the above-described procedure, boiling experiments are carried out for sample that are bare as well as for surface-treated AlN.

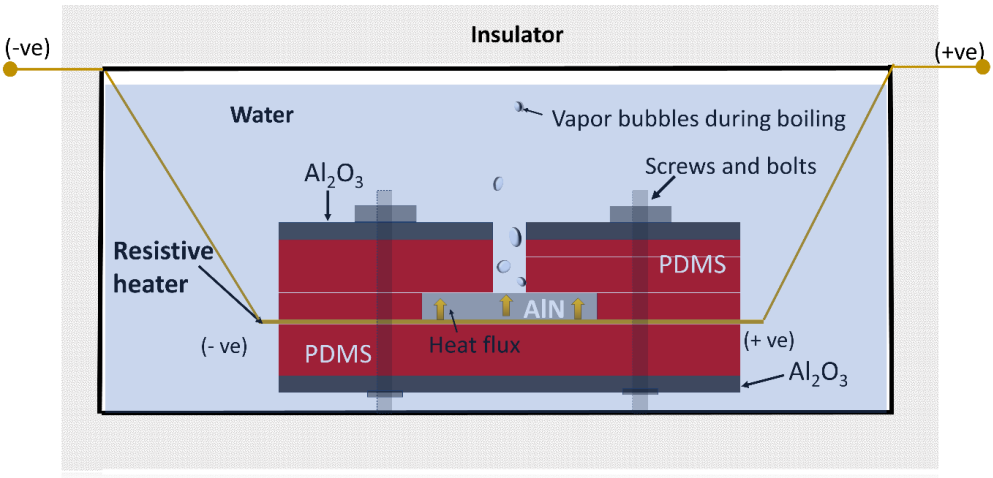

Figure 5.5 Schematic of the experimental setup of pool boiling experiment for long-term reliability test of AlN and surface treated AlN.

5.2.4.2 Quantification of corrosion rates at varying heat fluxes

We analyzed the morphology of the corrosion product on the surface exposed by scanning electron microscope, after being exposed to varying high heat fluxes during boiling. The corrosion products, hydroxides of aluminum are porous powders. To accurately measure the corrosion rates, removal of the corrosion products is needed for detection and quantifying corrosion. Etching of the samples in an acid solution to remove aluminum hydroxides is conducted. Aluminum hydroxides react with HCl to produce dissolvable aluminum chlorides but HCl does not attack the AlN. This provides selective removal of the unwanted corrosion products for further study. For example, $Al_2(OH)_3$ reacts with HCl:

$$3Al_2(OH)_3(s)+3HCl\ (aq) \rightarrow AlCl_3\ (aq) + 3\ H_2O\ (aq) \qquad \text{(ii)}$$

Similar chemical reactions are expected for AlOOH corrosion products. After the removal of the corrosion products, the depth of corrosion compared to a region not reacted with measured is determined. The depth of corrosion over time, measured in hours, can be used to calculate a corrosion rate during pool boiling of AlN.

5.2.4.3 Quantifying corrosion in a boiling ambient

To measure the corrosion rate of AlN in a boiling ambient, for example in a boiling water kettle and compare the corrosion rate for this case to high heat flux conditions we set up a separate experimental method. Conceptually if we place a sample in boiling ambient for an extended period of time and remove the corrosion product following the method described above, we can measure the corrosion rate. Utilizing the mass change between before and after the experiment, the corrosion rate is estimated. The mass change, Δm is converted into a corrosion thickness using $\delta = \frac{\Delta m}{\rho A}$, where ρ is the density of AlN and V is the volume of the sample, $V = A\delta$, A= Area of the sample and δ = thickness of the sample. In this estimation we neglect the corrosion at the four edge faces of the coupon due to their negligible cross-sectional area compared to the surfaces at the top and bottom. We also assume that the corrosion rate in the top and bottom surfaces are equal. Then, corrosion rate is in time, *t (hours)* is,

$$\delta' = \frac{\Delta m}{2\rho A t}(top\ surface) + \frac{\Delta m}{2\rho A t}(bottom\ surface) = \frac{\Delta m}{\rho A t} \qquad (5.1)$$

5.2.5 Experimental procedure

In this section we will discuss the experimental setup of conducting pool boiling experiments for AlN and surface treated AlN and quantifying corrosion rate in detail:

5.2.5.1 Pool boiling experimental setup to study corrosion

The boiling experiment is carried out by constructing a jig-type setup, here we describe the setup in detail. The heater side of AlN is connected with copper conductors using conductive epoxy. Insulation of the sample area to prevent heat loss is made sure using layers of alumina and PDMS. The setup consists of multiple layers stacked on top of one another with four screws running through each of the four corners for alignment. Starting from the bottom, two layers of

alumina measuring 250μm in thickness, three layers of poly-dimethyl siloxane (PDMS) measuring 250μm in thickness, and then on top of these bottom insulations, the AlN sample is placed at the middle. Closely encircling the AlN sample (less than 10 μm tolerance) another layer of PDMS measuring 250 μm thickness is placed. We then add insulating layers on top of the AlN substrate. Boiling occurs at the top surface of AlN, we cut holes in the middle of insulation layers to ensure water-AlN surface contact. The top insulating layers are composed of three layers of PDMS (250 μm thick) and two layers of alumina (250 μm thick), with a center square hole measuring 4 mm x 4 mm. The assembled jig containing AlN sample and insulations is then placed in a glass beaker. Saturated water is poured into the beaker and covered with a lid to minimize mass loss of water due to evaporation. The entire setup is then placed in a secondary container insulated using Rockwool. Power is then supplied using the power source.

5.2.5.2 Dependence on time of corrosion

To study corrosion depth dependence with time, we conduct boiling experiments at 60W/cm^2, and we vary the time of oxidation. Individual samples are prepared to study corrosion depth at 25 hours, 80 hours, 110 hours, and 150 hours respectively.

5.2.5.3 Corrosion dependence on heat-flux

Another set of experiments conducts the effect of heat flux on corrosion depth. Three separate pool boiling experiments are carried out at 60, 70, and 80 W/cm^2 heat fluxes, respectively for 4 days (96 hours).

5.2.5.4 Corrosion dependence on thickness of surface coating

We conduct corrosion test of surface treated AlN with a constant heat flux of 100 W/cm^2 for 1 μm, 2 μm and 3 μm thick surface oxide layers, respectively, for 4 days (96 hours).

5.2.5.5 Corrosion dependence on boiling ambient

Corrosion in boiling ambient is carried out in a kettle for 7 days by placing AlN coupons in a glass beaker of boiling water.

5.2.6 Imaging

The surface of the AlN exposed to boiling water is characterized by an SEM (Zeiss Gemini SEM 500), with 3 kV accelerating voltage and Everhart Thornley secondary electron detectors).

5.2.7 Corrosion Depth Measurements

The corrosion depth of the surface exposed to boiling water is measured using a profilometer (Bruker Dektak XT). The AlN surface is scanned in a straight line by the profilometer's tip, beginning at the surface not exposed to boiling water, moving on to the surface exposed to boiling water, and finally arriving at the AlN surface that is not exposed to boiling water, **figure 5.5 (b).** The corrosion depth is shown by the profilometer's Average Step Height (ASH) mode when bare AlN surfaces—those not exposed to boiling water—are utilized as the reference on either side of the AlN exposed to boiling water.

5.2.8 Chemical composition of surface

The surface chemical composition is measured using the Nexus X-Ray Photoelectron Spectrometer (XPS) with depth profiling capability. Bare AlN substrate and surface oxidized AlN substrates are plasma cleaned ($Ar+O_2$) for 5 minutes before the XPS measurements. The XPS spectra of both the bare AlN substrate and the surface oxidized AlN is collected.

5.3 Results and discussions

In this section the results from the experiments are presented. We discuss corrosion of bare AlN in pool boiling for varying heat fluxes, in boiling ambient and the effect of surface treatment on corrosion of AlN during pool boiling:

5.3.1 Imaging corrosion morphology of AlN after prolonged pool boiling

After 4 days of exposure to boiling conditions at 60 W/cm^2 heat-flux, the surface of the 4 mm x 4 mm optical microscopy and SEM investigations reveal that AlN after reacting with water have produced powder-like corrosion products aluminum hydroxides. The surface of AlN which is not exposed to boiling water, does not exhibit such corrosion, **Figure 5.5 (a).** After cleaning the corrosion products via etching and sonication, we took SEM images which revealed that the corrosion products were removed during cleaning and the corroded surface lay deeper than the bare AlN not exposed to boiling. **Figure 5.5 (b).**

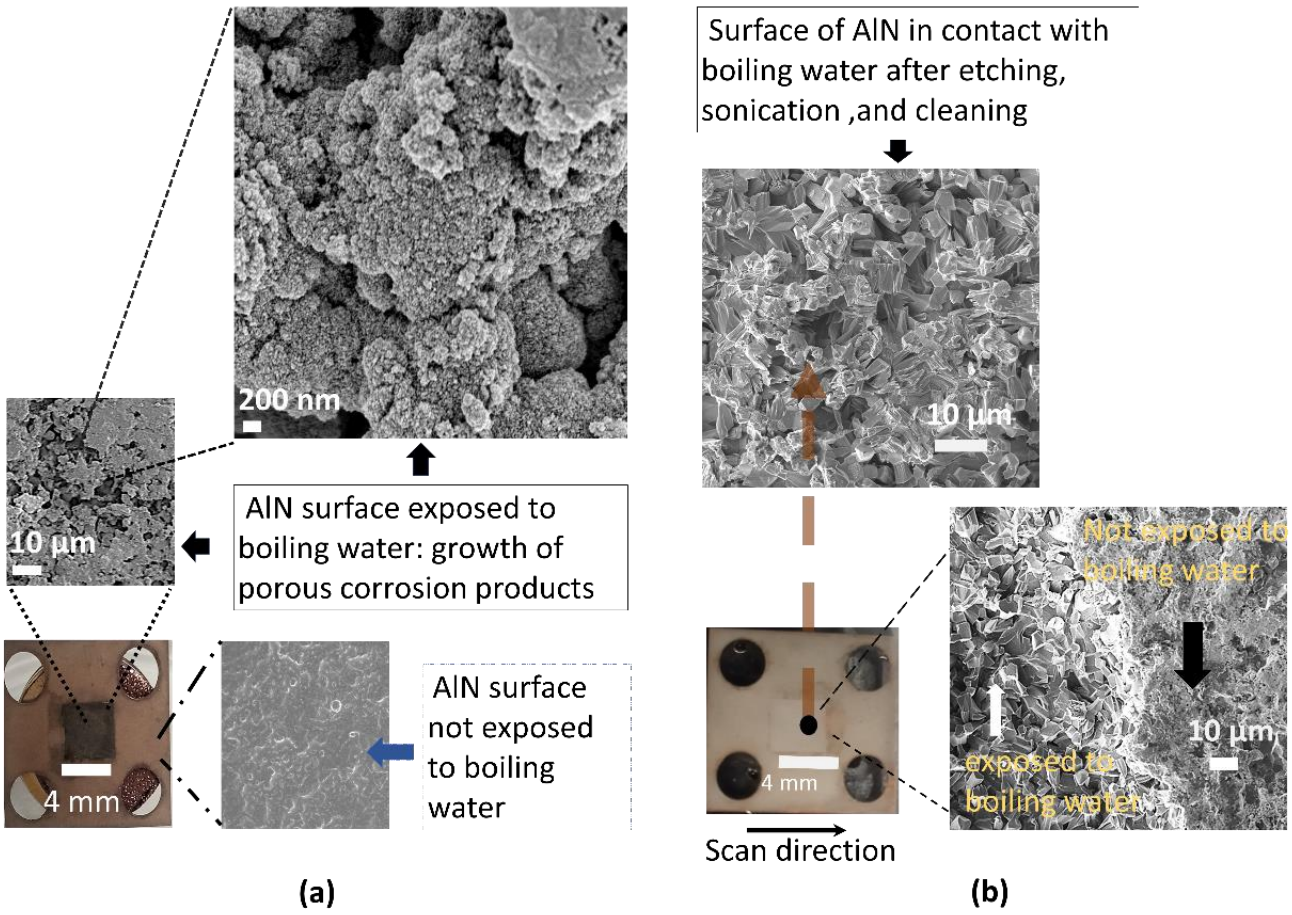

Figure 5.6 (a) Corrosion of AlN in pool boiling. The center region (darker due to gold sputtering for SEM imaging, imaged via optical microscopy) is where the AlN surface was in contact with the boiling water. The corrosion product is porous in nature compared to the surface of AlN which is not exposed to boiling water. **(b)** The sample after etching in 1 M HCl to clean the corrosion products: the plot of profilometry data, scan length in the x-axis, and corrosion depth in the y-axis.

5.3.2 Time dependence of corrosion of AlN in pool boiling

We measure the corrosion dependence of AlN on the boiling time by conducting multiple pool boiling experiments on separate AlN samples that run for varying amount of time (25 hours, 100 hours, 115 hours and 150 hours, respectively) at 60 W/cm^2 heat flux. The corrosion products were cleaned and removed by the method described in the above section, the corrosion depth was measured using profilometry. The profilometer is scanned from left to right: The first 4 mm of the profilometer's scan are on the AlN surface that is not subjected to boiling water, the following 4 mm are on the AlN surface that has been exposed to water, and the final 4 mm are on the AlN surface that has not been exposed to boiling water. At **Figure 5.7 (a)** we plot all the profilometry scan data of the corrosion depth at varying time of pool boiling; **Figure 5.7 (b)** is a scatter plot: average corrosion depth (y-axis) and time in hours (x-axis). A best fit curve reveal a linear relationship of corrosion depth of AlN in pool boiling with time.

5.3.3 Effect of heat flux on corrosion of AlN

Profilometry is used to examine the impact of heat flux on the corrosion of AlN in three separate samples that were subjected to three different heat fluxes for a total of four days. The corrosion depth is 16.1 μm for 60 W/cm^2, 16.8 μm for 70 W/cm^2, and 16.3 μm for 80 W/cm^2. **Figure 5.8** These experimental results imply that the corrosion rate of AlN in pool boiling remains essentially unaffected by changes in heat flux.

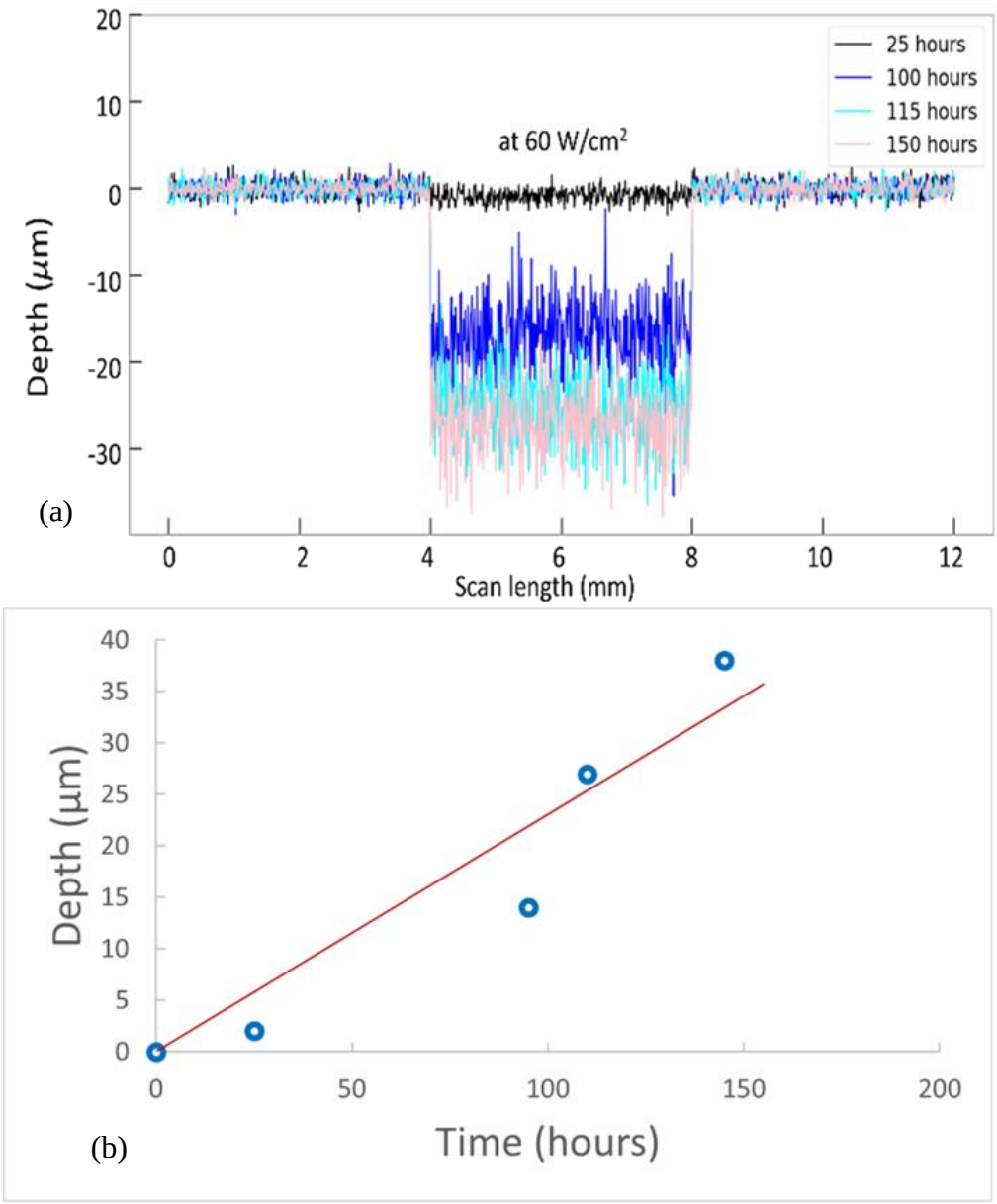

Figure 5.7 (a) Profilometry of corrosion depth of AlN with varying time, all data are plotted. **(b)** x-y scatter plot of average corrosion depth vs. boiling experiment time, reveals a linear relationship. The pool boiling experiments are conducted at 60 W/cm^2 heat-flux.

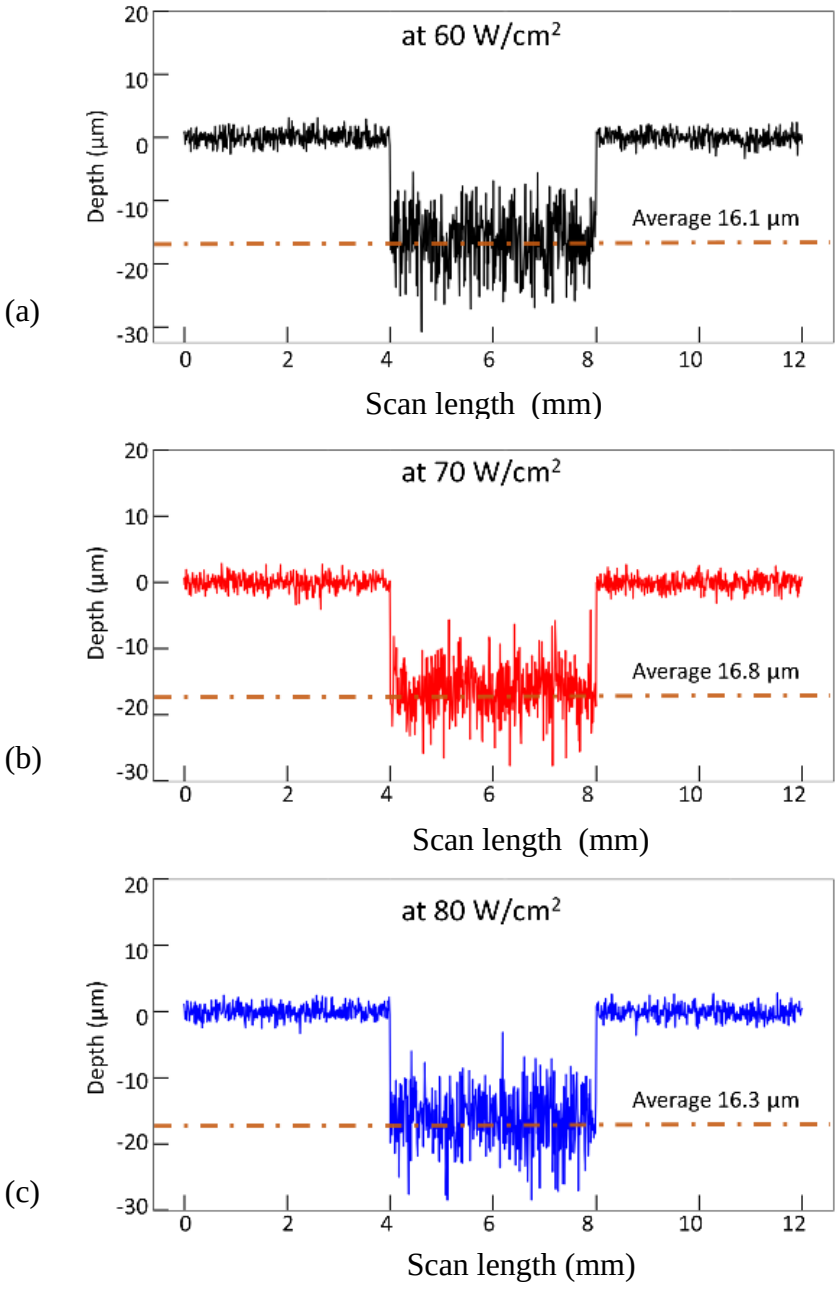

Figure 5.8 Profilometry probing corrosion depth of AlN surface exposed to different heat fluxes in pool boiling conditions relative to the surface not exposed to boiling. At, (a) 60 W/cm^2 corrosion depth is 16.1 µm, (b) 70 W/cm^2 corrosion depth is 16.8 µm, and (c) 80 W/cm^2 corrosion depth is 16.3 µm. The corrosion of AlN is unaffected by changes in heat flux.

5.3.4 Effect of surface treatment on the corrosion of AlN

The SEM image in **Figure 5.9 (a)** shows the formation of a porous, aluminum oxide layer following oxidation of the AlN surface at 1050^0C in air within a furnace. In addition, we image the surface of the surface oxidized AlN under pool boiling conditions, where it was exposed to 100 W/cm^2 for 4 days, **Figure 5.9 (b)**. Although, the protective layer remains relatively intact, the oxide surface undergoes morphological changes, we hypothesize that alumina reacts with water at elevated temperatures and bubble collapse during boiling release energy; we hypothesize that a combination of heat, pressure and chemical reaction of surface alumina with water, may lead to morphological change of the protective surface layer.

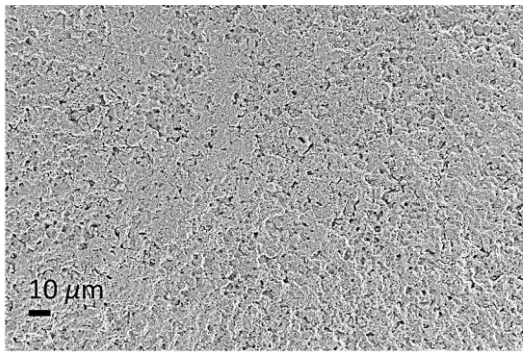

(a)

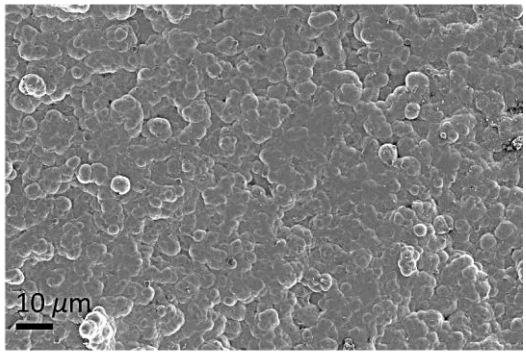

(b)

Figure 5.9 (a) The SEM images reveal the formation of a porous aluminum oxide layer on an AlN surface at 1050°C in air, and **(b)** show that the thick alumina coating undergoes morphological changes during prolonged exposure to pool boiling conditions.

5.3.5 Effect of Surface Treatment on the Corrosion Behavior of AlN in High Heat Flux Pool Boiling

In this section we will discuss the corrosion behavior of bare AlN and surface treated AlN in pool boiling conditions. Profilometry data of the samples undergone pool boiling for 4 days are presented for each surface treatment:

5.3.5.1 Thin Al coating on top of AlN without further treatment

After 4 days of boiling at 60 W/cm^2 we can detect signs of corrosion for the surface treatment of thin aluminum (200 nm, eBeam evaporated) coating on AlN using. In **Figure 5.8 (a),** we plot the data from profilometry. A corrosion depth of 22.4 μm is detected for 4 days of boiling for a corrosion rate of 0.21 μm/hour. Y. Hang *et al.* conducted a detailed study on the hydrolysis behavior of AlN in Al dross.[12] From their study they found that the presence of Al during AlN hydrolysis accelerate the kinetics. We hypothesize that a similar reaction mechanism may take place for this case.

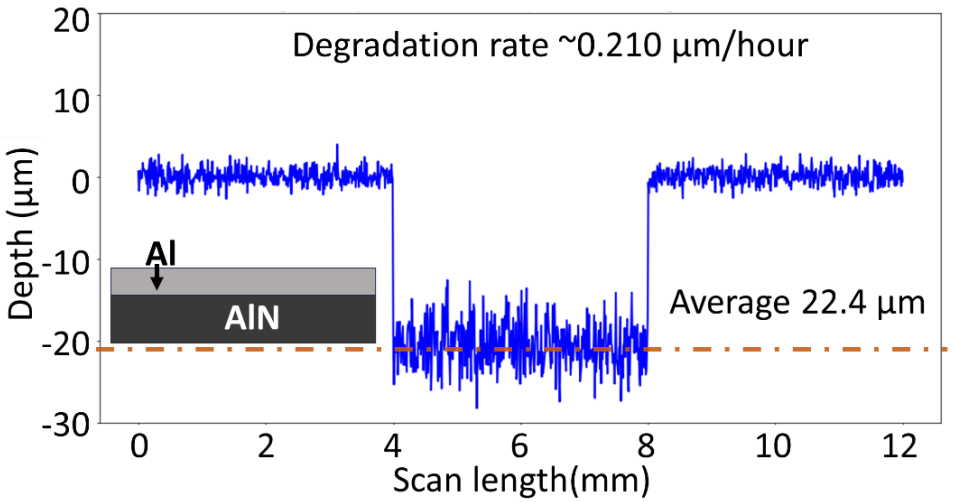

(a)

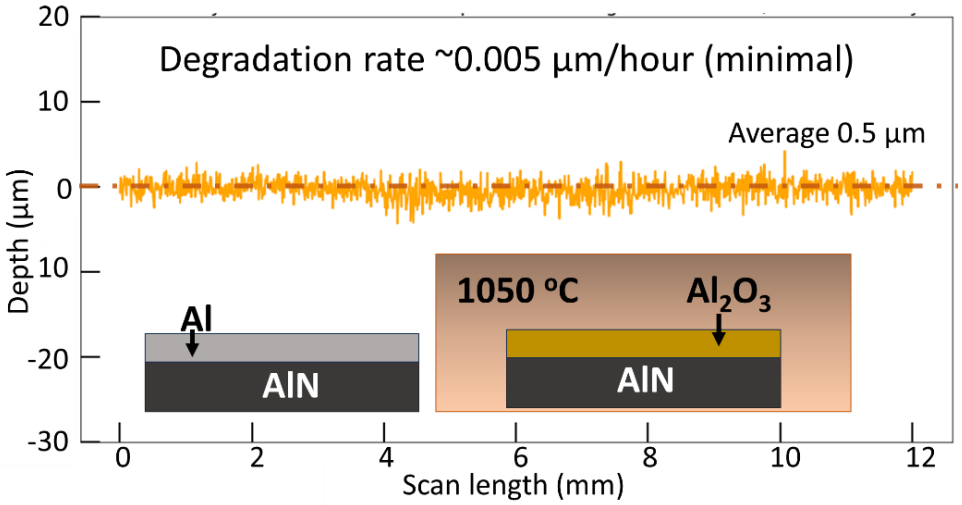

(b)

Figure 5.10 (a) Profilometry of corrosion after boiling of thin Al coating on top of AlN without further treatment. Significant corrosion is observed for this surface treatment in 4 days of boiling at 60 W/cm^2. **(b)** Profilometry of corrosion after boiling of thin Al coating on top of AlN and thermally oxidizing the Al layer. This surface treatment demonstrated minimization of corrosion significantly.

5.3.5.2 Thin Al coating on top of AlN followed by oxidation of the thin coating

In **Figure 5.10 (b),** we plot the profilometry data of pool boiling of thin Al coated on AlN followed by oxidation of the thin coating at 1050 ^{0}C for 2 hours. From the data, we observe that the oxidation to the surface coating of Al can effectively prevent the corrosion of AlN, negligible corrosion (~0.5 μm) is detected using profilometry after 4 days of corrosion.

5.3.5.3 Plain AlN oxidized

In **Figure 5.11 (a-c),** we plot the profilometry data after pool boiling of plain AlN oxidized at 1050^0C for varying time (1 hour, 2 hours and 3 hours of oxidation, respectively). The pool boiling experiment was conducted at 100 W/cm^2 for 4 days. From the data, we observe that by oxidating the plain AlN directly in a furnace at elevated temperature like 1050 ^{0}C can effectively prevent the corrosion of AlN, only negligible corrosion (~0.5 μm on average) is detected using profilometry after 4 days of corrosion for each surface treatment.

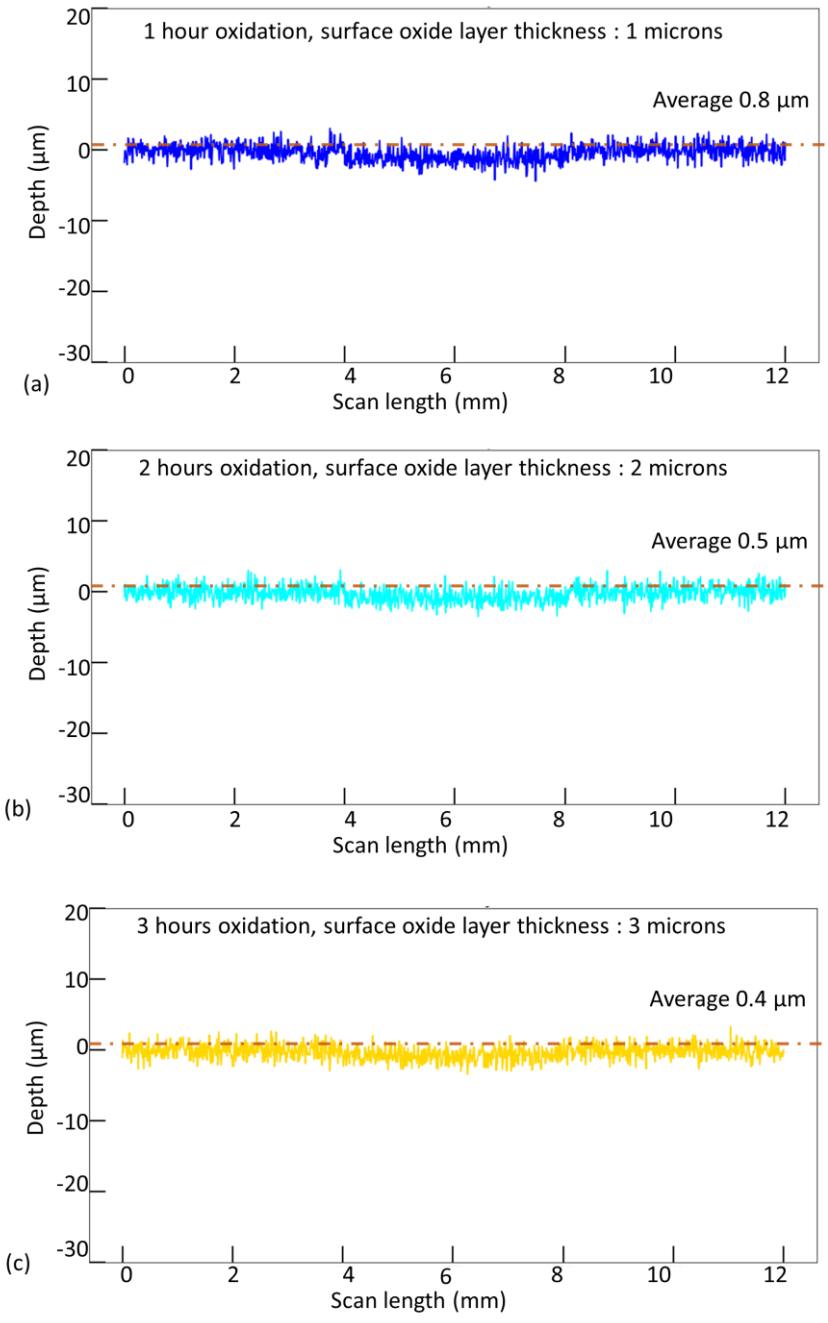

Figure 5.11 (a-c), The profilometry analysis revealed that under pool boiling conditions with a heat flux of 100 W/cm^2 three different surface-treated samples for one hour, two hours, and three hours, exhibited average corrosion of less than 1 μm after four days, in each case.

When we plot the profilometry data of pool boiling corrosion of plain AlN (4 days at 80 W/cm^2) and AlN with thermally grown thin surface coating of Al_2O_3 together, we can observe that the thin surface layer is effective to protect the AlN surface against corrosion of high heat-flux boiling water. **Figure 5.12**

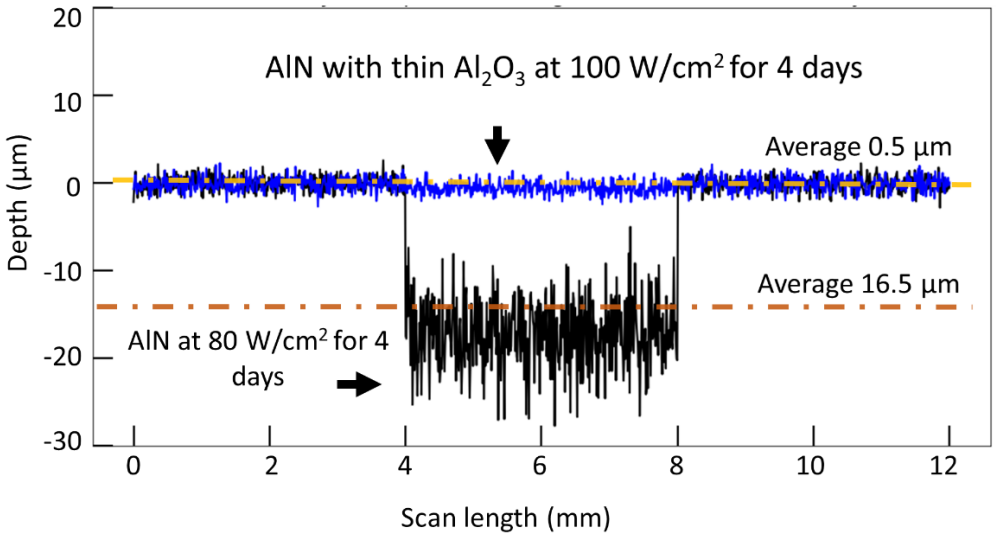

Figure 5.12 We plot the profilometry data of bare AlN exposed to pool boiling condition (80 W/cm^2, for 4 days) and thermally oxidized bare AlN surface (100 W/cm^2, for 4 days) together. The thermal oxidation treatment significantly increases the corrosion resistance of AlN.

5.3.6 Corrosion of AlN Boiling Ambient

Initial mass of AlN coupon is 0.3233 gm. The mass of the sample after boiling ambient for 7 days is 0.3201 gm. Using Equation (5.1), the rate of corrosion in terms of reduction of thickness in 0.024 µm/hour. We note that this is within the order of magnitude of the observation of AlN particles by Bowen *et al*. at room temperature (0.015 µm/hour).[1]

5.3.7 Surface Chemical Composition

X-ray Photoelectron Spectroscopy (XPS) analysis of thermally oxidized aluminum nitride (AlN) reveals a surface composition comprising aluminum and oxygen, indicating the possibility formation of aluminum oxide **figure 5.13 (a)**. Significantly, nitrogen was absent on the surface of the thermally oxidized sample compared to a pristine AlN sample **figure 5.13 (b)**.; suggesting that the thermal oxidation process removed or pushed nitrogen deeper into the material.

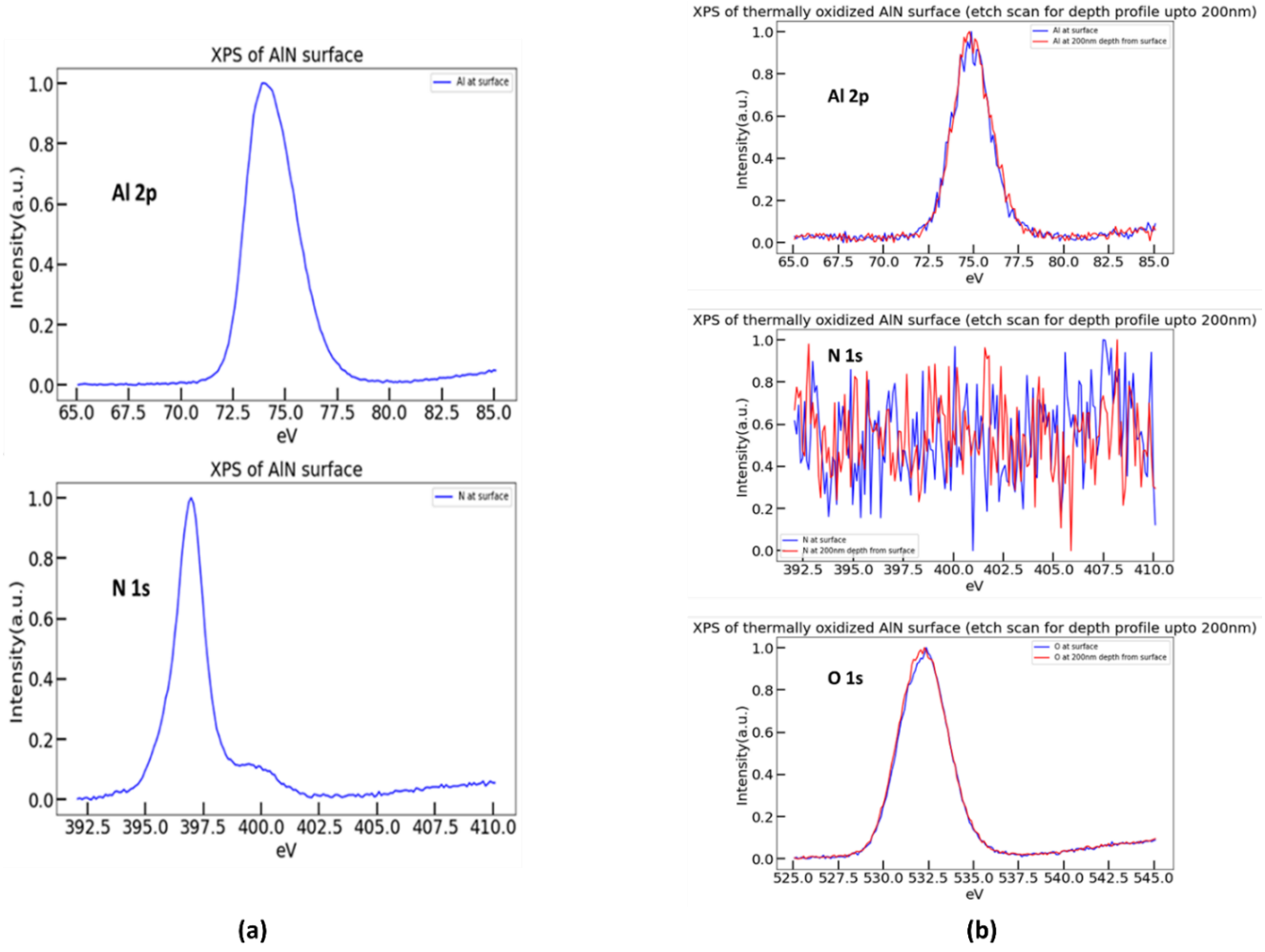

Figure 5.13 (a) XPS of AlN surface. **(b)** Depth profile scan up to 200 nm reveals that aluminum and oxygen is present on the surface and nitrogen is absent after thermally oxidizing the surface.

5.3.8 Modeling Thermal Resistance for Surface Treated AlN

We model the total thermal resistance of the AlN with a surface oxide layer, R_{Total} assuming a series addition of the thermal resistance of the AlN layer, $R_{1,}$ and thermal resistance of surface oxide (Al_2O_3) layer, $R_{Al2O3.}$ Assuming a thin (5 μm) solid Al_2O_3 grown on top of AlN (495 μm) the R_{Total} =3.2 x 10^{-6} K/W. The thermal resistance of a bare AlN (thickness, 500 μm) is 2.78 x 10^{-6} K/W. From this simple model, we observe a 14.96% increase in the thermal resistance of the oxidized AlN. The thermal resistance of oxidized AlN is underestimated by this model; experimental research indicated that oxidizing AlN at 1050^0 C could enhance its thermal resistance by up to 15%. Although the oxide layer on the surface of the earth is porous and can trap air, which has a very low thermal conductivity, our first model assumes that the oxide layer is solid. If we model the porous surface layer using Effective Medium Theory (EMT) [12], [13]where the heat is conducted through both the solid alumina and water trapped in the pore, then the effective thermal conductivity K_{eff} according to the effective medium theory:

$$\frac{(K_{alumina}-K_{eff})}{(K_{alumina}+2K_{eff})}(1-\phi_l) + \frac{(K_{water}-K_{eff})}{(K_{water}+2K_{eff})}\phi_l = 0 \qquad (6.2)$$

using the thermal conductivity values from experimental data K_{Al2O3} at 100 ^{0}C = 17.5 W/m.K and K_{water} at 100 ^{0}C = 0.68 W/m.K, and estimate for a case of solid fraction $(1-\phi_l)$ = 0.75 then we find, K_{eff} = 9.64 W/m.K from equation (6.2). Our estimation results to a total thermal resistance R_{Total} = 3.46 x 10^{-6} K/W. The effective medium theory with 75% solid fraction of 5 μm thin surface alumina layer estimates an increase of 23.3% of the thermal resistance **Figure 5.14**. We recognize that 75% solid fraction is a conservative estimate, the surface Al_2O_3 layer is expected to be much denser (solid fraction >90%). Further investigation can be carried out to determine the true porosity of the surface aluminum oxide.

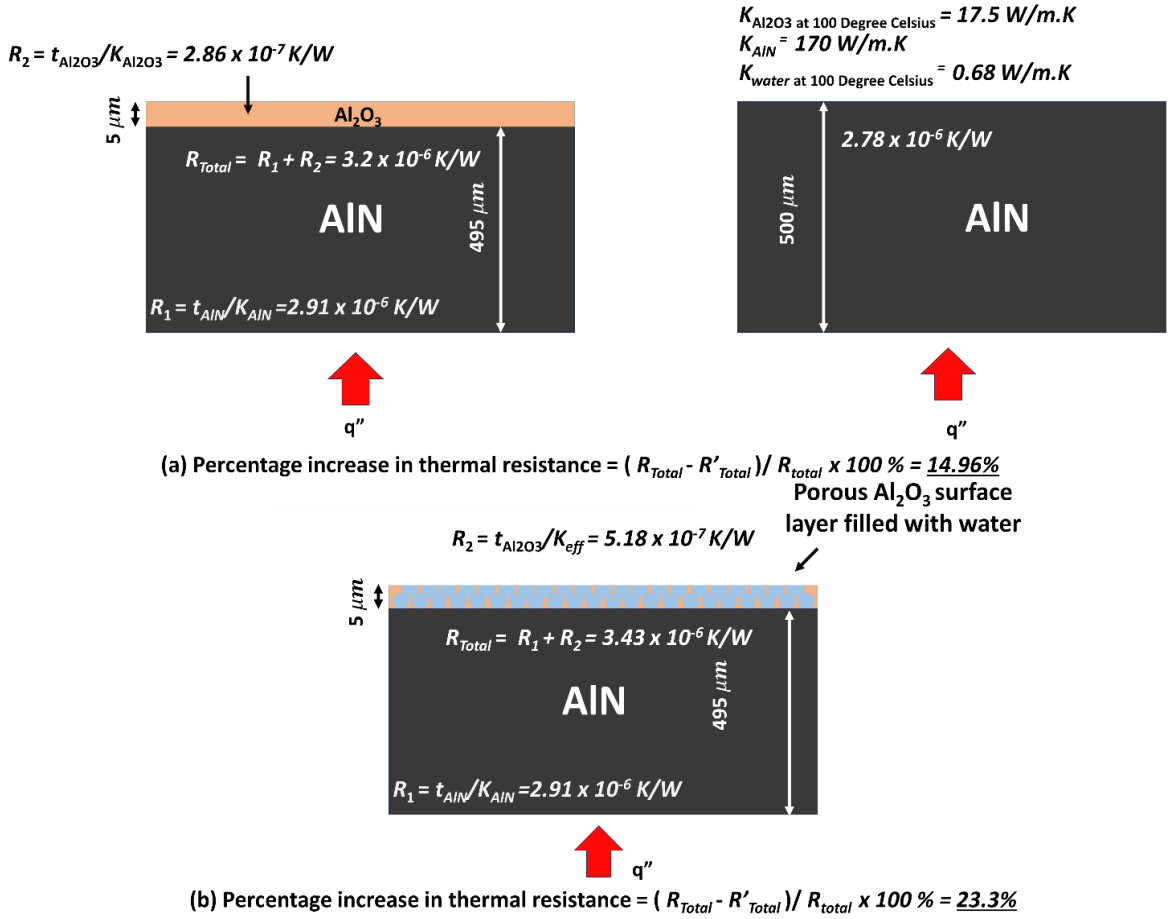

Figure 5.14 A simple model to determine and compare thermal resistances for surface oxidized AlN and bare AlN. The model assumes solid layers of AlN and surface Al_2O_3 at the top, heat is conducted from the bottom to top. Effective media theory can be also used to estimate effective thermal conductivity of a porous Al_2O_3 layer. Our model estimates 15%-24% increase in thermal resistance due to the surface treatment.

5.4 Conclusions

In this study, we characterize the corrosion of AlN in pool boiling conditions using profilometry. We found that the corrosion depth of AlN in pool boiling conditions exhibits a linear relationship with time for up to 150 hours. We

determined the heat flux dependence of the corrosion behavior by changing heat fluxes during the corrosion experiment. We found that the corrosion of AlN does not exhibit heat flux dependence. We explored surface treatment protocols to grow a thin, dense oxide layer on top of the AlN. We found that directly heating AlN in the air at 1050^0C to grow a surface oxide layer can be a one-step process to protect AlN from corrosion in pool boiling conditions. Our findings pave the way for using AlN as a substrate material in two-phase heat transfer processes.

5.5 References

[1] P. Bowen, J. G. Highfield, A. Mocellin, and T. A. Ring, "Degradation of Aluminum Nitride Powder in an Aqueous Environmet," *Journal of the American Ceramic Society*, vol. 73, no. 3, pp. 724–728, 1990, doi: 10.1111/j.1151-2916.1990.tb06579.x.

[2] K. Krnel and T. Kosmač, "Reactivity of aluminum nitride powder in dilute inorganic acids," *Journal of the American Ceramic Society*, vol. 83, no. 6, pp. 1375–1378, 2000, doi: 10.1111/j.1151-2916.2000.tb01396.x.

[3] A. Kocjan, A. Dakskobler, and T. Kosmač, "Evolution of aluminum hydroxides in diluted aqueous aluminum nitride powder suspensions," *Cryst Growth Des*, vol. 12, no. 3, pp. 1299–1307, 2012, doi: 10.1021/cg201349s.

[4] A. Kocjan, K. Krnel, and T. Kosmač, "The influence of temperature and time on the AlN powder hydrolysis reaction products," *J Eur Ceram Soc*, vol. 28, no. 5, pp. 1003–1008, 2008, doi: 10.1016/j.jeurceramsoc.2007.09.012.

[5] C. Y. Zhang *et al.*, "Mechanism for the hydrolysis resistance of aluminum nitride powder modified by boric acid," *Ceram Int*, vol. 48, no. 22, pp. 32696–32702, 2022, doi: 10.1016/j.ceramint.2022.05.308.

[6] S. Fukumoto, T. Hookabe, and H. Tsubakino, "Hydrolysis behavior of aluminum nitride in various solutions," *J Mater Sci*, vol. 35, no. 11, pp. 2743–2748, 2000, doi: 10.1023/A:1004718329003.

[7] A. Abid, R. Bensalem, and B. Sealy, “The Thermal Stability of AlN,” *J Mater Sci*, vol. 21, no. 5491, pp. 1301–1304, 1986, doi: 10.1016/S0140-6736(00)84859-X.

[8] T. Sato, K. Haryu, T. Endo, and M. Shimada, “High temperature oxidation of hot-pressed aluminium nitride by water vapour,” *J Mater Sci*, vol. 22, no. 6, pp. 2277–2280, 1987, doi: 10.1007/BF01132972.

[9] M. Dede, Ercan M.; Zhang, Chi; Wu, Qianying; Seyedhassantehrani, Neda; Shattique, K. Roy, Souvik; Palko, James W.; Narumanchi, Sreekant; Kekelia, Bidzina; Sougata, Hazra; E. Goodson, M. Giglio, Roman; Asheghi, and *, “Heat Flux Micro Coolers Having Multi-Stepped Features And Fluid Wicking,” 2022

[10] E. M. Dede *et al.*, “Techno-economic feasibility analysis of an extreme heat flux micro-cooler,” *iScience*, vol. 26, no. 1, p. 105812, Jan. 2023, doi: 10.1016/j.isci.2022.105812.

[11] C. T. Yeh and W. H. Tuan, “Oxidation mechanism of aluminum nitride revisited,” *Journal of Advanced Ceramics*, vol. 6, no. 1, pp. 27–32, Mar. 2017, doi: 10.1007/s40145-016-0213-1.

[12] H. L. Yang, Z. S. Li, Y. D. Ding, Q. Q. Ge, and L. Jiang, “Hydrolysis Behavior and Kinetics of AlN in Aluminum Dross during the Hydrometallurgical Process,” *Materials*, vol. 15, no. 16, Aug. 2022, doi: 10.3390/ma15165499.

[13] S. Sudhakar, J. A. Weibel, and S. V. Garimella, “Experimental investigation of boiling regimes in a capillary-fed two-layer evaporator wick,” *Int J Heat Mass Transf*, vol. 135, pp. 1335–1345, Jun. 2019, doi: 10.1016/j.ijheatmasstransfer.2019.03.008.

[14] J. A. Weibel, S. V. Garimella, and M. T. North, “Characterization of evaporation and boiling from sintered powder wicks fed by capillary action,” *Int J Heat Mass Transf*, vol. 53, no. 19–20, pp. 4204–4215, Sep. 2010, doi: 10.1016/j.ijheatmasstransfer.2010.05.043.

Chapter 6

Conclusions

The potential of two-phase heat transfer for managing the thermal output of high heat flux dissipating devices has prompted extensive research and paved the way for their widespread use. While significant advancements have been made in increasing the CHF and HTC of two-phase heat transfer, such as integrating hierarchical porous structures and surface functionalization for enhanced wettability; the liquid pressure drop, vapor blanketing of the porous evaporator, long-term reliability and the complexity of processing of porous materials has limited their wide-spread adoption.

Fluid management during two-phase heat transfer can improve the CHF. Liquid can be transported by capillary suction to a porous evaporator to maintain a thin-evaporating film, careful design can allow for separate vapor escape pathways. Furthermore, novel materials with high thermal conductivity, high electrical resistance and higher mechanical strengths like Aluminum Nitride (AlN) are enabling substrate materials for design of functional capillary driven two-phase heat transfer devices.

In this dissertation, we focused on addressing fluid management via a three-dimensional manifold structure placed on top of a laser processed porous evaporator. We demonstrated that capillary wicking can evenly distribute cooling liquid on the porous evaporator. Additionally, we explained and demonstrated why the relative permeability of a porous material in two-phase heat transfer varies during varying heat flux operations. We carefully measured the permeability of single layer thin, porous structures at varying capillary pressure via a novel method. Additionally, we designed and processed a 3D manifold integrating separated paths for liquid delivery and vapor escape via facile techniques. Furthermore, we delved into the reliability of AlN in long term two-phase heat transfer condition.

6.1 The key investigations and research findings

Free-Standing Mesh for Capillary Fluid Delivery

A porous heat spreader can receive liquid through capillary action from thin, free-standing porous materials. In order to drive liquid through capillary action, thin, free-standing mesh-like structures, such as copper mesh, offer sufficient permeability, capillary pressure, and high wettability. In comparison to thin liquid channels with solid walls, the microstructure of free-standing woven copper meshes, and their inherent thinness make it advantageous to incorporate multiple pieces of them for even fluid distribution to the porous heat spreader while maintaining low viscous pressure loss during capillary transport and passages for vapor escape through the pores, and the spaces between the meshes.

Measuring Permeability of Free-Standing Mesh Structure

While free-standing mesh-like porous structures can transport liquid via capillary action, both the liquid permeability and capillary pressures can vary with varying liquid saturation at varying flow rates. We introduced a method for measuring the permeability of free-standing mesh structures. Our method involves experimental techniques to quantify the permeability of these mesh structures. We measure and report permeability of a copper (#100) mesh at varying capillary pressure.

Similitude Analysis for Permeability-Capillary Pressure Relationship

We present a similitude analysis, which is a mathematical technique used to establish similarity between physical phenomena. In this context, we use similitude analysis to develop a relationship between permeability and capillary pressure that can be applied to mesh structures of different sizes having similar

geometry, e.g., weave, and materials. This allows for a more general understanding and application of our findings.

Surface Modification of Free-Standing Meshes and Resultant Permeability-Capillary Pressure Relationship

We discussed a method for surface functionalization, specifically the growth of micro-needles, to modify the wettability of mesh-like structures via electrooxidation. This involves altering the surface properties of the mesh to control how fluids interact with it. After modifying the meshes with micro-needles and adjusting their wettability, we investigate how these modifications affect the permeability-capillary pressure relationship. We investigated how surface modifications impact fluid flow through the mesh.

Integrated Manufacturing of 3D Manifold Structure with Liquid Channels and Separate Vapor Channels

We explore integrated manufacturing approaches for a 3D manifold structure with microchannels for liquid delivery and vapor escape. The processing of liquid microchannels with thin metallic sheets and metallic mesh-type wicks was explored. Furthermore, incorporating the liquid channels in a 3D manifold structure was investigated. The performance of 3D manifold device was tested and was found to significantly enhance the CHF of the porous evaporator.

Reliability of Aluminum Nitride (AlN) Substrate Materials

The direct integration of AlN porous structures on the substrate for two-phase cooling has been recently investigated. However, AlN degrades in boiling water; water has high surface tension and latent heat of evaporation making it a good working fluid for two-phase heat transfer. We investigated the corrosion

rate of AlN substrate materials under pool boiling conditions. We discussed the performance and durability of AlN in such conditions and measured the corrosion rate in pool boiling.

Surface Coating Technique to Prevent Corrosion

To address the corrosion issues identified, we present a surface coating technique designed to protect AlN from corrosion during pool boiling conditions. A novel and facile thermal treatment of the AlN surface was shown to be effective in controlling the corrosion of AlN. Furthermore, the heat-flux dependence of corrosion of AlN was studied in detail.

6.2 Outlook for Future Research

As an outlook for future research, we consider a few investigations that are motivated by the findings from this dissertation:

Firstly, we suggest a detailed experimental and numerical study of the reduced permeability of modified copper meshes under varying capillary pressures, further building on our initial findings. Each of the hypotheses provided in *Chapter 3* can be tested to explain the permeability-capillary pressure relationship of the oxidized mesh. The electrooxidation method in chapter 3 can be optimized for micro-needles shape, dimensions, directions and density and subsequently evaluating the permeability at varying capillary pressures.

Secondly, as described in *Chapter 5*, our findings show that a thickness of 2 μm of a surface aluminum oxide layer was effective in controlling corrosion of AlN at boiling near 100 W/cm^2 heat flux. Although, this surface treatment contributed to < ~15% of thermal resistance, exploring the minimum thickness of a surface oxide layer that can withstand corrosion can be investigated. We

propose further investigation of oxidation on AlN at 1050^0C at shorter oxidation times (5 minutes to 50 minutes, at a 5-minute interval) to minimize the oxidation thickness and study the effectiveness of these thin oxide layers on the corrosion performance. A tube furnace, in lieu of a glazing furnace will enable meticulous and time-effective investigation for this purpose. Furthermore, coating AlN with a nm-scale layer of highly conductive material that is electrically insulating (e.g., ZrO_2) via vapor deposition techniques (for example, atomic layer deposition, AlD) can be investigated. AlD is a versatile tool for uniformly coating complex shapes with a thin layer of secondary advantageous material. Often, AlD is used to coat porous catalysts. A similar experimental approach utilizing AlD can be taken to conformally coat porous heat spreaders made out of advantageous heat transfer substrate materials for high-efficiency pool boiling heat-transfer devices. We identify three key material properties necessary to consider in choosing appropriate material(s) to apply via AlD on a substrate for phase change heat transfer applications: thermal conductivity, thermal expansion coefficient and reactivity with the heat transfer liquid. We recognize that a coating layer as thin as a nanometer (nm) can be expected to have a minimal impact on the overall conduction resistance. Large thermal expansion co-efficient differences can lead to a situation where the coating might crack at high temperature operation. Here, we provide a non-exhaustive list of materials that can be considered for the AlD coating of porous evaporators made of AlN. **Table 6.1**. For the lack of experimental data availability, the reactivity with heat transfer liquid with each material is not listed.

Table 6-1 Materials suitable to coat porous evaporator made of AlN via atomic layer deposition (AlD)

Material	Coefficient of thermal expansion, α (10^{-6}/C)	Thermal expansion of materials in boiling water, (µm) $\Delta L = \alpha * L0 * \Delta T$ [L0 = 15mm], [$\Delta T = 80^{o}$ C]	Thermal conductivity, k (W/m.K) at 100^{0} C
Aluminum (Al)	23.1	28.0	220
Aluminum nitride (AlN)	4.5	5.4	178
Alumina (Al_2O_3)	8.4	10.8	30
Monolithic Zirconia (M-ZrO_2)	22	27	2
Beryllium Oxide (BeO)	6.5	7.8	158
Hexagonal Boron Nitride (hBN)	2.95	3.54	300

Thirdly, in *Chapter 2*, we presented a novel method to characterize permeability of mesh like structures at varying capillary pressures. The method can be used to measure permeability of other thin, porous structures (sintered powders, CIO, foams, to name a few). In the *supplementary section of Chapter 2*, we described how this method can be expanded for other porous materials. A couple of key bottlenecks of the method presented are extended time and the high number of samples required for the measurements. We propose development of a method which can address these bottlenecks. A concept that can be explored is using a small amount of sample inside a pressurized chamber (air pressure can be controlled to control the capillary pressure). The permeability measurements can be made by calculating altering volumetric flow rates at different capillary pressures or conducting the rate-of-rise test, which requires visual monitoring and recording of capillary rise, inside a pressurized chamber. These proposed concepts are expected to minimize time and sample

requirements for the permeability measurements of porous materials and devices, at varying capillary pressures.

Fourthly, in *Chapter 4*, we described processing of a manifold structure which incorporates copper mesh as liquid channels. While single layer copper mesh provides adequate permeability to address heat flux of 1000 W/cm^2, the manifold can incorporate other types of porous materials for enhanced performance. A simple but effective implementation can be to sandwich two finer meshes (e.g., copper #200 mesh) to process liquid channels that would provide higher capillary pressures due to the smaller pore sizes and the space in-between the meshes would provide sufficient permeability for the fluid to flow. Fine copper foams (e.g., 100 μm average pore sizes) can also be used to process the liquid channels directly for capillary driven fluid delivery. Metals foams like copper foams promise both high permeability and high capillary pressures. Thin sectioning tools (e.g., BuehlerMaterials PetroThin) can be used to prepare consistent thin liquid channels (on the order of 50 μm -150 μm) from a thicker foam stock (the stocks are usually on the scale of millimeter thickness). Another class of materials that we propose for liquid channel, or the entire manifold are porous glass/ceramics. Glass/ceramics are strongly wetting materials of fluids like water. They provide an additional advantage of sustaining corrosion and degradation at higher temperatures and during extended operations while at two-phase heat transfer. To this extent, processing of a porous liquid channel with percolating paths made of fine glass/ceramics particles can be explored as research investigations. Another approach is to pursue additive manufacturing by directly 3D printing from glass or ceramics based extruded filaments. The 3D printed liquid channel, or the entire manifold can be subsequently pyrolyzed and cleaned to remove polymeric binders. A subsequent sintering step can be added to sinter the particles to ensure structural integrity of the 3D printed porous structure.

In conclusion, this dissertation delved into investigating strategies towards the realization of a practical two-phase heat transfer device driven by the capillarity of porous materials. Many of the methods developed during this study can be used to measure properties of various porous materials useful for phase change processes. The findings of key material properties, design strategies for enhanced performance, and the facile processing techniques developed, will

narrow focus and stimulate future investigations of capillary driven two-phase heat transfer. The findings of this dissertation are expected to pave the way for a working, cost-effective, and reliable capillary driven two-phase heat transfer device at a commercial scale.

END.